Canadian Exploration Geophysical Society

CANADIAN EXPLORATION GEOPHYSICAL SOCIETY

GEOPHYSICAL SYMPOSIUM 2023

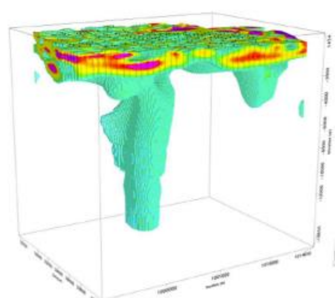

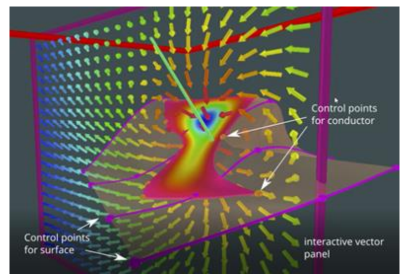

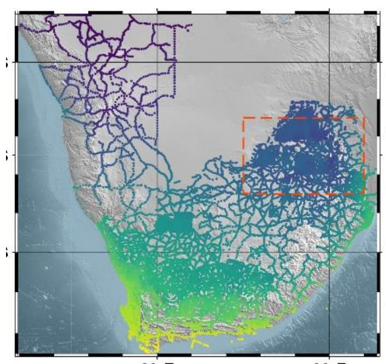

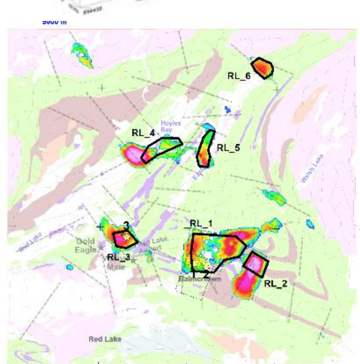

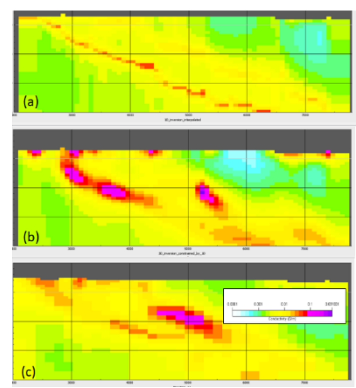

Saturday, March 4th, 2023
Intercontinental Hotel, Toronto

Delegate Program generously sponsored by

ABITIBI GEOPHYSICS

KEGS thanks the Symposium sponsors

Breakfast

TERRAQUEST AIRBORNE GEOPHYSICS

CRONE GEOPHYSICS

Lunch

Geotexera Geophysical Modelling & Inversion

Coffee Breaks

SCINTREX A DIVISION OF LRS

QUANTEC Geoscience

Reception

SEEQUENT

PHOENIX GEOPHYSICS

DMEC Decennial Mineral Exploration CONFERENCES

TABLE OF CONTENTS

12:20	**Lunch**		
13:25	***Session 3:*** AI/ML and Critical Minerals Exploration Chairs: **Alzbeta Ondercova**, Expert Geophysics Limited, **Darren Burrows**, KEGS Secretary-Treasurer		
13:30	**Karl Kwan, Jean M. Legault*** Geotech Ltd	Targeting concealed orogenic gold mineralization using aeromagnetic data: A case study from the Red Lake camp, Superior Province, Ontario, Canada	39
13:50	**Stephen Hallinan*, Wolfgang Soyer, Carsten Scholl, Randall Mackie, Tom Kimura, Friedemann Samrock** CGG Multiphysics	Recent developments in integrated electromagnetics 3D inversion	--
14:10	**Blake Cross*, Hannah Peterson** Condor Consulting Inc.	A comparison of airborne geophysical data over two magmatic nickel deposits	50
14:30	**[1]Tim Munday*, [2]Mike McMillan, [3]Rod Paterson, [4]Camilla Soerensen, [5]Noelene Dorn** [1]Deep Earth Imaging FSP, CSIRO, [2]Computational Geosciences Inc., [3]Intrepid Geophysics, [4]Aarhus Geosoftware, [5]ElectroMagnetic Imaging Technology Pty Ltd	AEM modelling and system options in the search for critical mineral systems in a regolith dominated environment – the Musgrave Province, Central Australia	55
14:50	**Coffee Break**		
15:15	***Session 4:*** Case Histories Chairs: **Jenna McKenzie**, Ronacher McKenzie Geoscience, **Peter Tschirhart**, KEGS Vice-President		
15:20	**José Antonio Rodríguez*, Mehran Gharibi** Quantec Geoscience Limited	Geophysical signatures in high enthalpy geothermal explorations using 3D MT survey	64
15:40	**Alexander Prikhodko** Expert Geophysics Limited	Recovering exploration models patterns with airborne total field passive electromagnetics	68
16:00	**William J. Scott** GeoScott Exploration Consultants Inc	Airborne GPR Survey for Bathymetry, Muskrat Falls, Labrador	73
16:20	**[1]Alireza Malehmir*, [1]Magdalena Markovic, [1]Myrto Papadopoulou, [2]Paul Marsden** [1]Uppsala University [2]Nordic Iron Ore	Establishment of a hardrock seismic test site in central Sweden	76
16:40	**Peter Tschirhart** Vice President of KEGS	Closing remarks	
16:50	**Reception**		

*Presenter

Autonomous Ground Gravity Trial Survey

Lee Zayonce (1), Richard Chow (1), Richard Lachapelle (2)*
(1) De Beers Group Exploration, (2) Scintrex Limited

Summary

An autonomous gravity trial survey was conducted by using the self leveling Scintrex Limited RG-1 remote operating gravimeter paired with unmanned ground vehicles (UGV) provided by Clearpath Robotics. The trial survey was conducted on the premises of Clearpath Robotics' Waterloo, Ontario office. The RG-1 gravimeter was deployed on a Husky UGV to conduct a remotely operated gravity survey grid in an empty parking lot. The UGV did not contribute any significant noise to the readings acquired by the RG-1. The survey consisted of 24 stations spaced at ~10 m, covering an area of ~1575 m. The Husky platform was able to collect accurate and quality data with the RG-1 station standard deviation of 7 microgals over the three survey days. This proved to be slightly more accurate than the CG6 control survey that used the same grid locations and rendered a CG-6 station standard deviation of 11 microgals. The proof of concept of using a gravimeter on a UGV was successful and can be further expanded upon.

Introduction

In order to reduce the amount of personnel working in hazardous areas, De Beers Exploration has explored the potential use of autonomous ground gravity data acquisition to conduct future surveys. Remote operation was a key component to removing the operator from potential harm from landmines, animals, poor weather, and trip hazards. In addition to safety, productivity could also benefit from such a system.

A proof-of-concept trial ground gravity survey was conducted over a parking lot to determine the feasibility of using a UGV together with a gravimeter. The objectives of this trial were to:

1. Demonstrate proof of concept of using gravity meter on a remote platform
2. Conceptually demonstrate the ability to remove operator from risks
3. Test accuracy and quality of gravity data
4. Improve productivity over long periods
5. Evaluate platform suitability of using gravity meter on robot
6. Address any shortfalls observed and relay to relevant parties for improvement
7. Determine the suitability of the UGV for gravity surveys

This project was formed in collaboration between De Beers Group Exploration, Clearpath Robotics and Scintrex Limited.

Testing commenced on October 17 and concluded on October 20, 2022.

Methodology

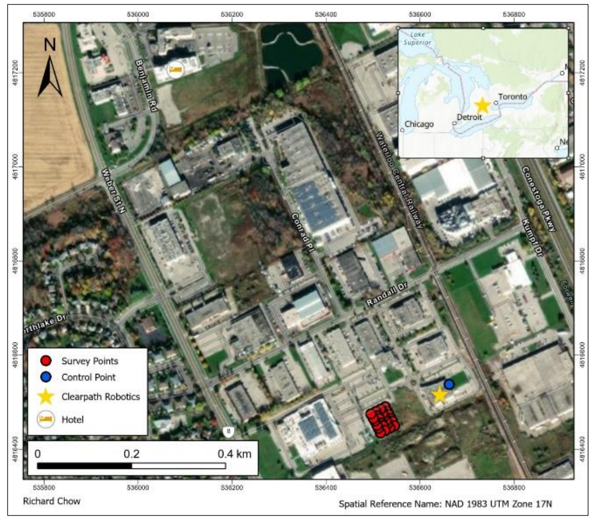

Location of the autonomous gravity survey trial in relation to the town of Waterloo, ON.

The test was carried out in a parking lot located close to the offices of Clearpath Robotics in Kitchener, Ontario.

The RG-1, a remote operating gravimeter, was selected to be used in this test due to its remote operation features. This particular RG-1 was outfitted with an external wireless adapter to allow for remote connection. A laptop with the accompanying software, Remote Gravity Software (RGS), was required to operate the RG-1

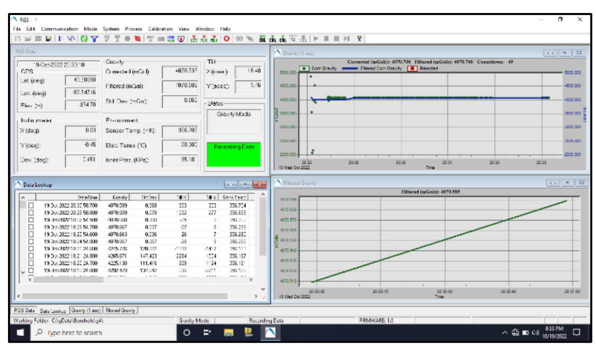

RGS software user interface used to remotely control the RG-1

Two CG-6's owned by DeBeers were brought to conduct a conventional survey to compare and evaluate the performance of the remote platform. Drift calibration was completed on all gravimeters prior to the start of the trial survey.

Clearpath Robotics provided two UGV models for testing, the Husky and the Warthog. The Husky was used to complete the survey and majority of the testing as we did not have full access to the Warthog. The Husky UGV was a small compact four wheeled vehicle whereas the Warthog was a large vehicle with tracked or wheeled variants. An array of sensors was available for both UGVs including DGPS navigation system, inertial measurement unit, wheel odometer, 3D/2D LIDAR, and cameras. For testing purposes, the RG-1 was mounted on a frictionless plate bolted on top of the Husky. The extent of the Warthog trial was a brief demo of maneuverability and stationary readings the RG-1 on placed on top of the UGV.

Husky UGV with RG-1 attached (left) shown side by side with a Warthog UGV (right)

Another component of the UGV system was a base station that houses a GPS and router which is responsible for relaying communication between the remote operator and the UGV. It can be powered from an external battery or be fully powered using solar panels.

The software to remotely control the UGV was called OutdoorNAV and was run from web GUI via an internet browser. A series of waypoints called "missions" can be set to determine the path that the UGV follows. "Goals" are waypoints where the UGV performs a programmed task at a specified location upon arrival. The interface provides the status of the UGV in real-time and allows for manual control to drive the UGV.

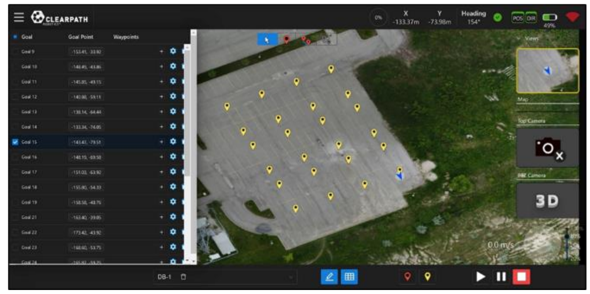

The OutdoorNAV user interface developed by Clearpath Robotics

Survey Results

To evaluate the potential noise introduced by the UGVs, a baseline gravity reading was first measured indoors on the floor. The readings were very comparable concluding that the UGV's had little to no influence on the gravity measurements. The main source of noise for the RG-1 was determined to be wind. The variation of wind speed and direction changed over the duration of the trial. Therefore, it was not possible to constrain what wind conditions (speed or direction) are within tolerable limits for accurate gravity measurements to be collected. The RG-1 was more exposed to the wind when mounted on the Husky compared to the Warthog. This resulted in higher SD's but the readings were still repeatable.

A survey grid was mapped out in an empty parking lot consisting of 24 stations at ~10 m spacing. A control point reading located on a concrete pad was taken before and after the collection of each set of stations for all surveys.
Three surveys were conducted on three different days using the RG-1 and Husky UGV. All RG-1 surveys were completed remotely with the operators at a distance of up to 70 m away. On the last survey day, October 19th, mud tires were used instead of standard radial road tires. A variety of weather conditions were encountered ranging from rain to hail with variable wind.
Each spot where a reading was taken was marked by spray paint to repeat subsequent readings using the CG-6. Two surveys were completed using the CG-6's operated by two different operators.

The UGV obstacle avoidance system was tested by placing cones and other impediments in the travel path. The Husky was able to determine a new path and navigate through the obstacles.
The rugged off-road terrain performance was not evaluated given the urban nature of the nearby area. This was however not a main objective of this trial, and therefore should be included in future evaluations.

Survey grid mapped out in an empty parking lot

For each of the five surveys the total survey length was recorded excluding the control point and the average minute per station was calculated, **Error! Reference source not found.**1. A minimum of two 60 second readings within 5 microgal was the internally set criteria for data quality on this survey. Due to windy conditions more than two readings were required on multiple stations. On October 17th, production began with the RG-1. As expected, there was a learning curve associated with understanding both the RG-1 and OutdoorNAV process and methodology. The survey became more efficient each day as the team became familiar with the platform. Once the RG-1 survey was underway on October 17th, the two CG-6's began to survey the same stations. Lee Zayonce surveyed with unit 290 and trained Richard Chow on how to operate unit 302. Lee completed all 24 stations on October 17th, however Richard stopped at station 16 due to a later start. Richard completed the remaining stations on October 18th with an overlap repeating four stations. Both operators could have surveyed quicker as they were out of practice/learning for the first time and distracted by the priority RG-1 survey. In comparison, the RG-1 October 19th survey had similar production to that of CG-6 290 operated by Lee.

	CG-6 290	CG-6 302	RG-1 Oct 17	RG-1 Oct 18	RG-1 Oct 19
On Grid Survey Time (hours)	**1:45**	**2:22 ***	**3:41**	**2:42**	**1:47**
Minutes/ Station	**4:22**	**5:04**	**9:12**	**6:45**	**4:28**

Production Summary

*Completed over 2 days (repeated 4 stations)

The test grid was composed of 24 stations and was surveyed five different times, twice by the CG-6's and three times with the RG-1. The various forms of acquisition provided an opportunity to compare the different gravity collection methods. The data are summarized below. A minimum of two 60 second readings within 5 microgals was the internally set criteria for data quality on this survey. Due to windy conditions more than two readings were required on multiple stations. The average standard deviation of all the readings for the CG-6 290 and 302 were 33 and 34 microgals respectively. In comparison, the average SD of all the readings for the RG-1 on Oct.17, Oct. 18, and Oct. 19 were 111, 158 and 120 microgals respectively. The CG-6's had less surface area and were lower to the ground reducing the effects of wind shake which resulted in lower reading SD's compared to the RG-1 mounted on the Husky. The Tide and Drift Corrected data, and the Corrected Bouguer data, was evaluated for each of the five surveys. The average standard deviation for all stations across all five surveys was 10 microgals. This was a good result and shows all five techniques can produce similar results. It was interesting to note that the CG-6 average station SD of 11 microgals versus the RG-1 average station SD of 7 microgals.

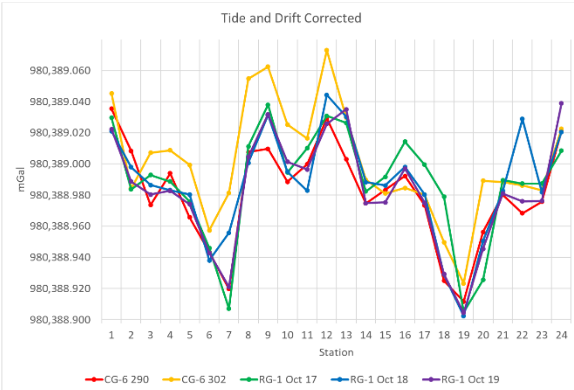

Tide and Drift Corrected data for all five surveys

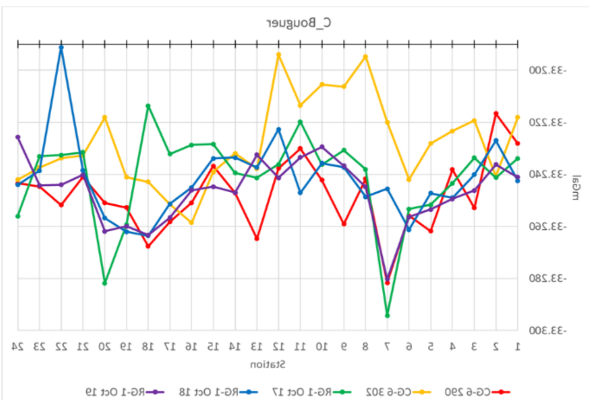

Corrected Bouguer data for all five surveys

Conclusion

The proof of concept of using a gravimeter on a UGV was a success. The team was able to integrate the RG-1 and Husky into single platform. Through wireless operation of RG-1 and Husky via Wi-Fi, the operator was removed from any potential risks. DGPS control of UGV location and coordinate capture eliminated the need for DGPS operator. Neither the Husky nor the Warthog UGV contributed to any noise observed on the RG-1. The test survey of 24 stations showed the platforms ability to acquire accurate and quality data which were repeatable in windy conditions. Through continued collaboration we hope to promote further interest and advancements in this technology.

Acknowledgments

I would like to acknowledge the support of De Beers Exploration, as well as Clearpath Robotics for use of their Husky UGV, technical support and dedicated service time from their engineers, and Scintrex Limited who generously allowed access to the RG-1 and provided the support of geophysicist Richard Lachapelle.

References

Clearpath Robotics, 2022, Husky Unmanned Ground Vehicle, https://clearpathrobotics.com/husky-unmanned-ground-vehicle-robot/, Manual, accessed 23 January 2023.

Clearpath Robotics, 2022, Husky User Manual, https://docs.clearpathrobotics.com/docs/robots/outdoor_robots/husky/user_manual_husky/, accessed 23 January 2023.

Clearpath Robotics, 2022, Warthog Unmanned Ground Vehicle, https://clearpathrobotics.com/warthog-unmanned-ground-vehicle-robot/, accessed 23 January 2023.

Clearpath Robotics, 2022, Warthog User Manual, https://docs.clearpathrobotics.com/docs/robots/outdoor_robots/warthog/user_manual_warthog/, accessed 23 January 2023.

Scintrex Limited, 2019, CG-6 Autograv™ Gravity Meter Brochure, https://6c3ae8.a2cdn1.secureserver.net/wp-content/uploads/2019/01/CG-6-Brochure_R5.pdf, accessed 23 January 2023.

Scintrex Limited, 2019, CG-6 Autograv™ Gravity Meter Operation Manual, https://6c3ae8.a2cdn1.secureserver.net/wp-content/uploads/2019/03/CG-6-Operations-Manual-RevC.pdf, accessed 23 January 2023.

Scintrex Limited, 2021, RG-1 Remote Operating Gravity Meter Brochure, https://6c3ae8.a2cdn1.secureserver.net/wp-content/uploads/2019/12/RG-1-Brochure-R2.pdf, accessed 23 January 2023.

Scintrex Limited, 2021, RG-1 Remote Operating Gravity Meter Operation Manual, https://6c3ae8.a2cdn1.secureserver.net/wp-content/uploads/2021/06/RG-1-Manual-1.pdf, accessed 23 January 2023.

Joint inversion of the gravity gradiometry and magnetic data in the Ring of Fire, Ontario, using the probabilistic Gramian

Michael S Zhdanov and Michael Jorgensen, University of Utah and TechnoImaging, Salt Lake City, UT, USA.*

Summary

We have harnessed the power of statistical and probability theory to jointly invert airborne gravity gradiometry (AGG) and total field magnetic intensity (TMI) data towards unified density and magnetization vector models of the Thunderbird V-Ti-Fe deposit in the McFaulds area of Ontario, Canada. We developed a probabilistic form of Gramian constraint in the regularized inversion to enforce similarity across the multimodal geophysical models. In the framework of this novel approach, the Gramian is defined as a determinant of the covariance matrix between different physical models representing the subsurface geology The incorporation of total field magnetic data can significantly improve the results of inversion of other more costly types of geophysical data, i.e., gravity gradiometry, AEM, etc.

Introduction

In mineral exploration, the joint inversion of multimodal geophysical data can significantly improve our understanding of the local structure and economic deposit targeting. Many deterministic joint inversion approaches have been championed over the last few decades, i.e., cross gradients, clustering, and the Gramian constraint (Gallardo and Mejo, 2003; Sun and Li, 2016; Zhdanov et al., 2012). We demonstrate that the Gramian can be constructed as a determinant of the covariance matrix between different physical models (e.g., density and magnetization) in the framework of the probabilistic approach to inversion theory. This approach allows us to harness the power of statistics and probability towards the joint inversion of multimodal geophysical data based on the probabilistic Gramian constraint.

Moreover, the inversion of total field magnetic data towards not only the scalar susceptibility but towards the full magnetization vector can significantly improve the subsurface models and increase drilling success. This is accomplished by accounting for magnetic remanence, which can heavily distort magnetic susceptibility models if present.

As an illustration of these methods, we jointly invert gravity gradiometry tensor and total field magnetic data acquired in the McFaulds area of Ontario, Canada, towards density and magnetization models, highlighting a 10-50% magnetite formation which was difficult to image using the traditional approach of inverting for only scalar susceptibility (Jorgensen and Zhdanov, 2021). The geomorphology of the jointly inverted models closely matches the drilling results.

Probabilistic Gramian joint inversion

The joint inverse problem is formulated by the following operator equations: $m^{(i)} = \left(A^{(i)}\right)^{-1} d^{(i)}$, $(i = 1,2)$, where $m^{(1)} = \rho$ is the density model, $m^{(2)} = \{M_x, M_y, M_z\}$ is the model corresponding to the scalar components of the magnetization vector, $A^{(i)}$ are the forward modeling operators, $d^{(i)}$ are the data, and the superscript $i = 1,2$ indicates the gravity and magnetic problems, respectively. The inverse problem is ill-posed, so we apply regularization and optimize a probabilistic parametric functional by the conjugate gradient method (Zhdanov 2009; 2015).

Using probability and statistical theory, we can consider the observed data and the model parameters as realizations of some random variables. The joint inversion requires the correlation between different model parameters, which can be done by adding the term containing the covariance matrix, representing a probabilistic analog of the Gramian constraint in the deterministic approach.

The regularized joint inversion algorithm minimizes the probabilistic parametric functional, P_σ^α, which is a linear combination of the sum of multiphysics data misfit functionals, $\sum_{i=1}^{n} \varphi\left(m^{(i)}\right)$, and probabilistic Gramian, S_{G_σ}(Zhdanov et al., 2021):

$$
\begin{aligned}
P_\sigma^\alpha\left(m^{(1)}, m^{(2)}, \dots, m^{(n)}\right) \\
&= \sum_{i=1}^{n} \varphi(m^{(i)}) \\
&+ \alpha \sum_{i=1}^{n} s(m^{(i)}) \\
&+ \beta S_{G_\sigma}\left(m^{(1)}, m^{(2)}, \dots, m^{(n)}\right) \\
&= min,
\end{aligned}
$$

where the misfit functionals are given by:

$$\varphi\left(m^{(i)}\right) = \left\| W_d^{(i)} (A^{(i)}\left(m^{(i)}\right) - d^{(i)}) \right\|_2^2,$$

the stabilizing (smoothing) functional is given by:

$$s\left(m^{(i)}\right) = \left\|W_m^{(i)}\left(m^{(i)} - m_{apr}^{(i)}\right)\right\|_2^2,$$

and the probabilistic Gramian term, S_{G_σ}, can be introduced as the determinant of the covariance matrix between different model parameters:

$$S_{G_\sigma}\left(m^{(1)}, m^{(2)}, \ldots, m^{(n)}\right) = \begin{vmatrix} cov\left(m^{(1)}, m^{(1)}\right) & \ldots & cov\left(m^{(1)}, m^{(n)}\right) \\ \ldots & \ldots & \ldots \\ cov\left(m^{(n)}, m^{(1)}\right) & \ldots & cov\left(m^{(n)}, m^{(n)}\right) \end{vmatrix}.$$

Both AGG and TMI data are weighted by a function of the errors:

$$W_d^{(i)} = 1/\left(err_f^{(i)} d^{(i)} + err_{abs}^{(i)}\right),$$

where $err_f^{(i)}$ are the fractional errors (0.05 for the AGG and TMI data), and $err_{abs}^{(i)}$ are the absolute error floors (2-4 Eotvos for the AGG data and 50 nT for the TMI data). Data weights are then further scaled in the joint inversion such that the first misfit for each term $\varphi\left(m^{(i)}\right)$ is equal to 1.

Model weights are determined by the following function of integrated sensitivity:

$$W_m^{(i)} = diag\sqrt[4]{F^{(i)*}F^{(i)}},$$

where $F^{(i)}$ is the Fréchet derivative matrix of $A^{(i)}\left(m^{(i)}\right)$, and $F^{(i)*}$ is its' complex conjugate matrix. Model weights are then further scaled in the joint inversion by normalizing with the maximum value of the model parameters obtained from standalone inversions.

The regularization terms α, β are adaptively reduced to ensure stable convergence (Zhdanov, 2009; 2015). Inversions were terminated when the fractional error floors corresponding to a 5% difference in observed and predicted data were reached.

McFaulds area example

We applied the developed methodology to joint inversion of gravity gradient tensor and total field magnetic data collected over the Thunderbird V-Ti-Fe deposit in the Ring of Fire area of Ontario, Canada. The deposit is heavily magnetite enriched and has a corresponding high response in both gravity and magnetics.

The Ontario Geological Survey (OGS) and the Geological Survey of Canada (GSC) collaboratively acquired the airborne data with the Fugro Airborne Surveys gravity gradiometer and magnetic system between 2010 and 2011. The observed data versus the data predicted from the probabilistic Gramian inversion is shown in Figures 1 and 2. As an illustration, we show the vertical gradient of the gravity field in Figure 1 only; however, several tensor components were used in the inversion.

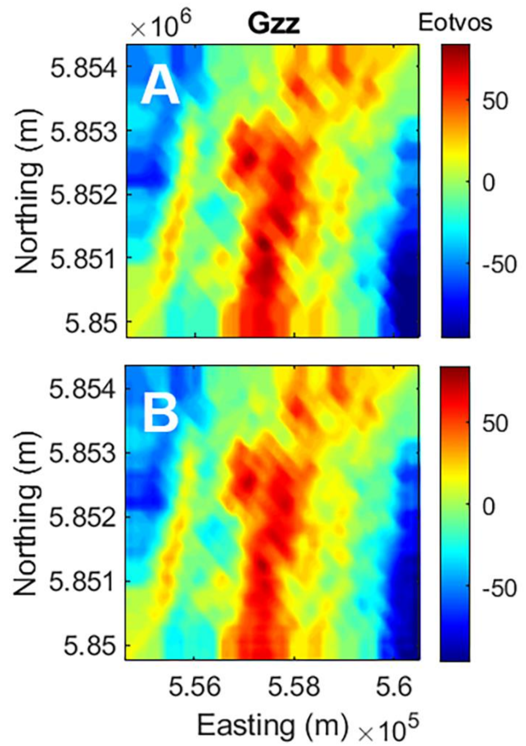

Figure 1. Panel A shows the observed Gzz gravity tensor component. Panel B shows the Gzz gravity tensor response predicted from the probabilistic Gramian inversion.

We conducted separate inversions of gravity gradient tensor and TMI data, generating standalone models. Figure 3 shows a comparison of these models to the results of the joint inversion of the gravity gradient tensor and TMI data using the probabilistic Gramian approach.

Note that the TMI data are inverted into the magnetization vector, which allows us to consider the remanent magnetization. This is achieved by applying the probabilistic Gramian constraints to different scalar components of the magnetization vector (Jorgensen and Zhdanov, 2021). The dominant vertical component, M_z, is shown in panels B and D in Figure 3. By jointly inverting the AGG and TMI data for density and full magnetization vector, we were able to recover the density and magnetic models of the Thunderbird V-Ti-Fe deposit, which correlate well with the known drilling results.

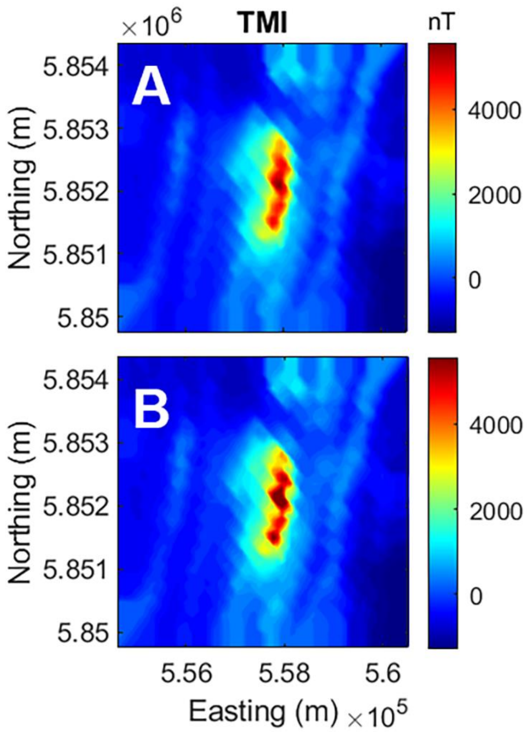

Figure 2. Panel A shows the observed TMI data. Panel B shows the TMI response predicted from the probabilistic Gramian inversion.

We have also generated model parameter cross plots shown in Figure 4 and calculated the correlation coefficient for the area near the Thunderbird deposit with respect to the standalone inversion results (0.8) and the models produced by the probabilistic Gramian inversion (0.89). Analysis of these trends can yield insight into the petrophysical relationships present near the deposit.

Conclusions

We have developed a novel approach to the joint inversion of multiphysics data based on probabilistic Gramian constraints. This approach was illustrated by inverting gravity gradient tensor and total field magnetic data towards structurally similar density and magnetization models of a V-Ti-Fe deposit in the McFaulds region of Ontario, Canada.

The developed probabilistic Gramian constraint yielded models with geomorphology consistent with drilling results. In particular, the magnetization model produced by joint inversion significantly improved over both the standard inversion results for scalar susceptibility and the standalone inversion for the magnetization vector.

Acknowledgments

The authors acknowledge the Consortium for Electromagnetic Modeling and Inversion (CEMI) at the University of Utah and TechnoImaging for the support of this research. The AGG and TMI data were collected by Fugro and made available by the Ontario Geological Survey, Canada.

References

Gallardo, L. A., and Meju, M. A. [2003] Characterization of heterogeneous near-surface materials by joint 2D inversion of dc resistivity and seismic data, Geophysical Research Letters, **30**(13), 1658.

Jorgensen, M. and Zhdanov, M. S. [2021] Recovering magnetization of rock formations by jointly inverting airborne gravity gradiometry and total magnetic intensity data. Minerals, **11**(4), 366.

Sun, J. and Li., Y. [2016] Joint inversion of multiple geophysical data using guided fuzzy c-means clustering. Geophysics, **81**(3), 1MJ-Z27.

Zhdanov, M.S. [2009]. Geophysical Electromagnetic Theory and Methods. Elsevier.

Zhdanov, M.S. [2015]. Inverse Theory and Applications in Geophysics. Elsevier.

Zhdanov, M.S. [2018]. Foundations of Geophysical Electromagnetic Theory and Methods. Elsevier.

Zhdanov, M. S., Gribenko, A. V. and Wilson, G. [2012] Generalized joint inversion of multimodal geophysical data using Gramian constraints. Geophysical Research Letters, **39**, L09301.

Zhdanov, M.S., M. Jorgensen, and L. Cox [2021], Advanced methods of joint inversion of multiphysics data for mineral exploration: Geosciences, 11, 262

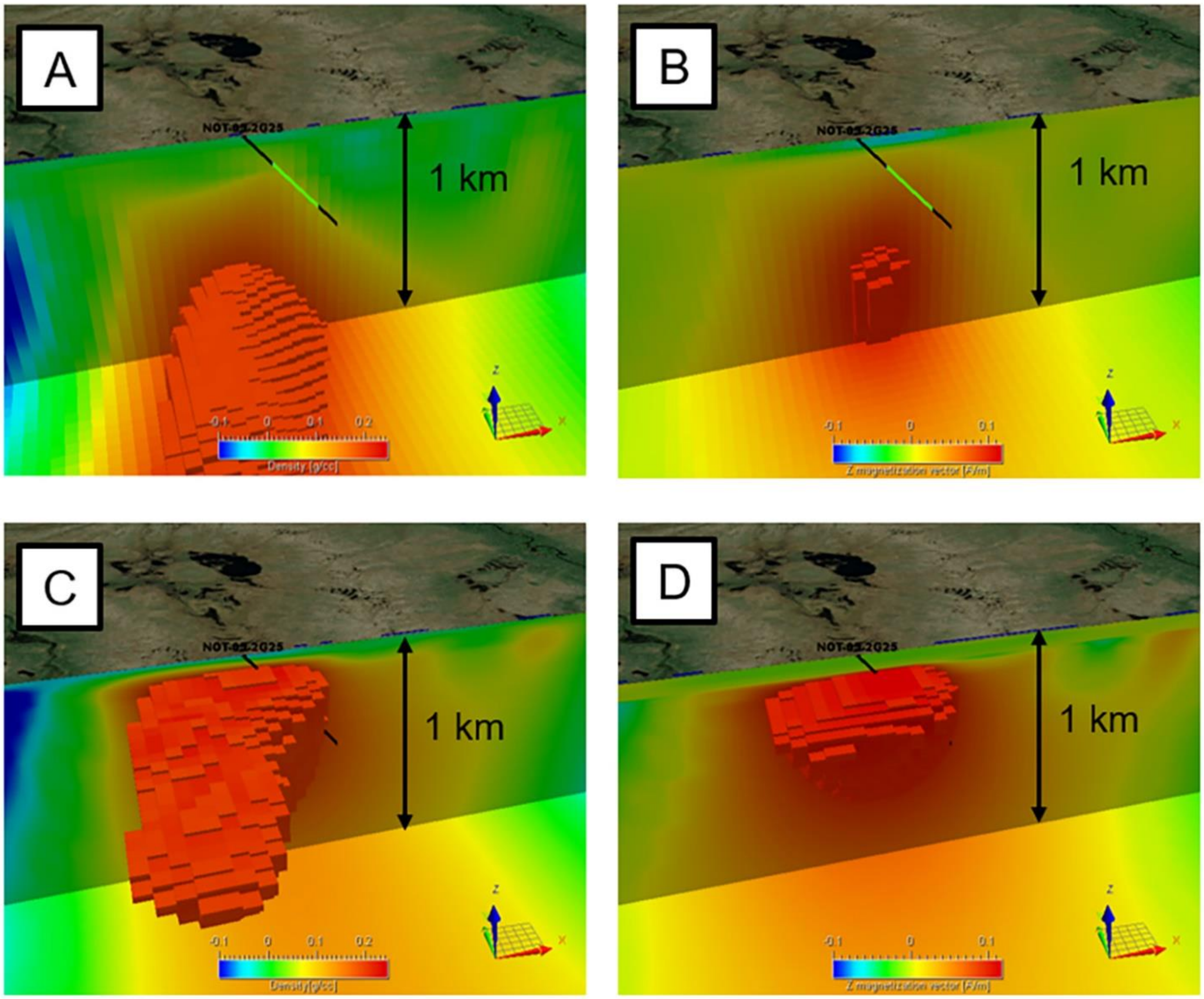

Figure 3. Panels A and B show the standalone inverted density model and vertical component of the magnetization vector model, respectively. Panels C and D show the jointly inverted density model and vertical component of the magnetization vector model, respectively. The bold black line indicates the drilling extent, and the green segment indicates the zone of high mineralization (10-50% magnetite).

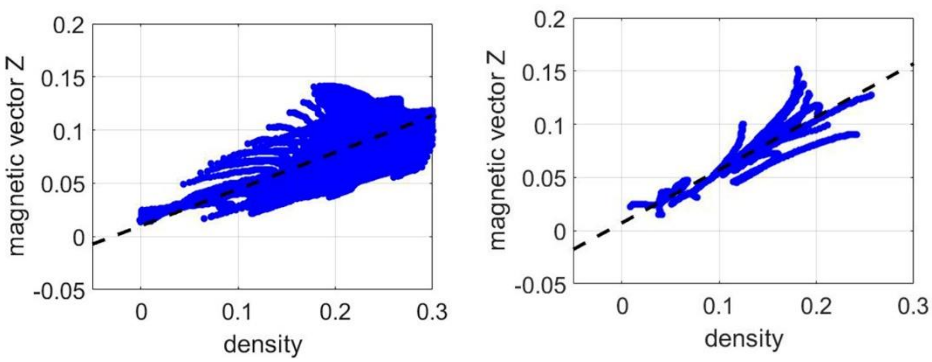

Figure 4. Cross plot of the density and vertical component of magnetization vector models shown in blue. The polynomial trend line is shown by the black dashed line. Panel A shows the standalone inversion results, and Panel B shows the probabilistic Gramian inversion.

Electromagnetic Modelling of Thin Conductors of Complex Shape

Ben Polzer, Nova Mining Exploration Solutions, Sudbury Ontario, Canada (Novaminex)

Summary

EM modelling is an essential step in the use of electromagnetic methods for the location and characterization of sulphide mineral deposits. For tabular deposits in relatively resistive host rocks, the thin rectangular plate model in free-space has proven to be very effective in establishing the location, attitude and approximate size of a conductor. For early-stage exploration this is usually enough to target drilling however as the definition of a mineral system proceeds the plate model is limiting because it cant represent the true shape of the deposit and is therefore limited in guiding subsequent drilling.

Novaminex has developed a software program (Provus) that can simulate the EM response of conductors that are mappings of a plate onto complex forms in 3D. The algorithm uses a modal decomposition of the eddy currents into non-interacting eigencurrents each with an exponential decay. This form of solution provides for very compact representation of the transient EM field and results in a semi-analytic solution which allows for analytic integration over source waveforms. The algorithm is fast enough to be used for interactive modelling with computation times of seconds for moderately complex multiple-conductor models.

Introduction

Computer modelling became the primary means of interpretation of EM data in the late 1980's with the introduction of rectangular plate modelling on a desktop PC. Early programs included PLATE and OZPLATE were single conductor plate simulations based on work by AP Annan (1973). The approach solved the integral equation for the electric field on the plate surface in an indirect manner. The eddy currents are shown to be the result of a countably-infinite set of eigencurrents, each a current pattern with its own intrinsic exponential decay. These eigencurrents are not a mathematical fiction but a fact arising from the induction process in a bounded region of uniform conductivity. Each eigencurrent, or "mode", has a progressively more complex geometric form and a more rapid decay rate. Unlike finite element or finite difference methods which require the conductor to be broken into elements or a finite difference grid, the integral equation method uses global continuous basis functions to describe the eddy currents. While the mathematical approach is elegant a large number of modes are required to describe the eddy current if the receiver is close to the edge of the conductor and the mutual inductance of all modal pairs have to be evaluated numerically. To make the problem more tractable for early desktop PCs the ribbon model was created in 1986 by Yves Lamontagne. This used the same basic mathematical formulation, but it limited the modes to be only varying in a "radial" manner, with current constrained to flow within concentric ribbons. This drastically reduced the number of modes required to get a solution but the approximation is valid only when the primary field is uniform over the surface of the plate. The ribbon model was commercialized by Lamontagne Geophysics as MultiLoop I in 1989 running on DOS and as MultiLoop II in 1993 on the Macintosh. Andrew Duncan (EMIT) brought this model to Windows in 1997 with the introduction of Maxwell.

Rectangular plate modelling has become the mainstay of EM survey data interpretation since that time. While there is much to recommend this simple model which is easy to manipulate parametrically and provides information useful to guiding exploration, it usually cant come close to approximating the true shape of a mineral deposit and so only a portion of the response details can be modelled from any line of borehole. Because the eddy currents can't flow from one plate to the next it is impossible to create an accurate representation of a single complex shaped conductor by modeling a collection of plates approximating its shape. Even if we accept the limitations afforded by its shape, the use of concentric ribbon basis functions does not produce correct results when the primary field coupling varies significantly over the plate surface.

In 2014 Novaminex began work on a new modelling algorithm based on the modal approach of Annan but updated to handle more complex shapes and using more general basis functions. The progress was slow for a number of years while we explored rapid transformations or mappings from a regular 2D figure (eg circle or square) into a closed region on a surface in 3D. While some candidate techniques were found they were too slow to form the basis of a practical modelling program.

In 2021 a more practical approach was pursued guided in part by the notion of geological constraints. Most tabular mineral deposits are constrained locally to an orientation conformal with a geological horizon. A two-staged mapping process was used. First a surface is defined in 3D as the "Canvas" containing the conductor and then the conductor is defined as a closed region within that surface. The technique provided a fast and effective way of defining and modifying the conductor geometry by manipulating control points to define the Canvas followed by modification of the conductor shape within the Canvas. Since mid-2021 Novaminex has developed a software program "Provus" to apply this modelling concept to the EM response simulation of multiple interacting conductors of complex shape.

Theory

A Provus simulation is based on the solution to the quasi-static integral equation for the electric field (Figure 1).

$$\frac{\overrightarrow{K_s}}{\sigma_s} - \frac{j\omega\mu_0}{4\pi}\iint \frac{\overrightarrow{K_s}(\vec{r}-\vec{r}')}{|\vec{r}-\vec{r}'|}\,dr' = \overrightarrow{E_s}$$

$\overrightarrow{K_s}$ Surface current density

σ_s Conductance

$\overrightarrow{E_s}$ Electric field of source

Figure 1. Integral equation in the electric field relating the local voltage drop (first term) the electric field created by all the time varying currents (second term) and the primary electric field right hand side).

This equation which relates the surface current density on a thin sheet to the source electric field can be solved directly for each instance of source excitation and angular frequency however the approach described by Annan solves for the physics of the left-hand side in a general way. The solutions are a set of "eigencurrents" derived as linear combinations of a set of divergence-free basis functions. Each eigencurrent has a simple exponential time decay. To determine the weight of each eigencurrent in any specific solution we need only integrate the dot product of primary electric field with the eigencurrent across the surface. Surface currents are described as the curl of a vector potential having only a normal component so that the contours of the potential function are streamlines of current. Figure 2 shows the first four basis functions and the eigencurrents. The time decay (step response) for a specific transmitter loop coupling is shown in the lower row.

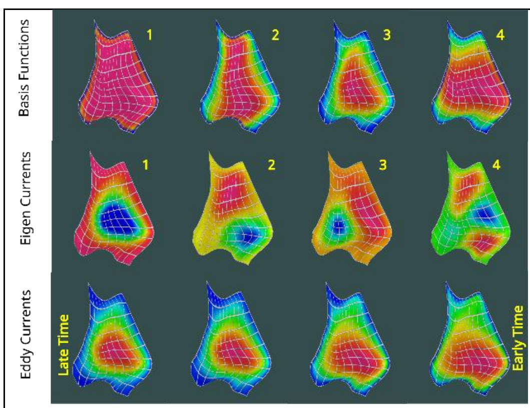

Figure 2. Comparison on a complex shaped conductor of surface current potential for: Basis functions, Eigen Currents derived from the Basis Functions and Eddy currents derived from the Eigen Currents.

Since Provus uses a 2D harmonic series (sin and cosine) for its basis functions it can accurately simulate eddy current systems as they migrate from early to late time (Figure 3).

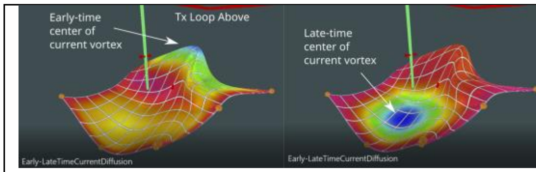

Figure 3. Surface current potential on conductor of complex shape showing early to late time eddy current diffusion.

The Provus "Ribbon" Model

The Canvas is a mapping of a unit square into 3D space and we can think of it as a piece of graph paper that has been morphed to a 3D form to form the domain for creating and interacting with the conductor (Figure 4). The Canvas may correspond to a particular geological horizon favorable to mineralization. The Canvas is defined by a set of control lines. The Ribbon conductor itself is described in the coordinate system of the Canvas as a collection of bounding control points.

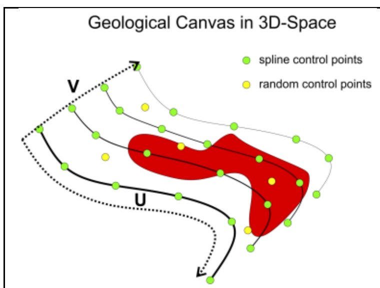

Figure 4. The Provus Ribbon model is based on a 2-stage transformation from a unit square to a 3D shape.

Provus User Interface

Data are currently imported from industry-standard ".TEM" files however custom importers can be written to accommodate any data format. Modelling sessions are managed from a project directory which contains the data as well as waveforms, sampling schemes and loop trajectory files. The project directory also provides caches for keeping time-stamped versions of the conductor models and simulation results as the session proceeds. Existing plate models are imported from industry standard ".PTE" files. Provus embraces the rectangular plate model as a useful starting point for modelling more complex conductor shapes. Provus Plate models can co-exist with the deformable Ribbon models in a mutually-interacting manner.

In a typical modelling session the user can start with a rectangular plate model which can be manipulated parametrically from a dialog or interactively (Figure 5). Once a reasonable fit has been found the plate can be promoted to a Provus Ribbon which can be manipulated interactively with its control points (Figure 6). The misfit between the observed and model response is observed in separate plot forms that may be customized to best suit the modelling session.

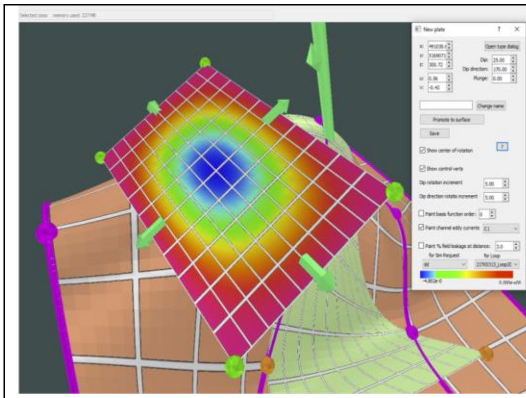

Figure 5. Provus Plate model with eddy current potential painted on its surface. The plate can be manipulated in 3D using dialog or 3D controls.

Visualization tools help to give the interpreter insight. Any number of vector panels may be created, positioned and oriented to visualize the secondary, primary or total fields (Figure 6). For borehole surveys, the direction of the data components can be viewed down the hole. "Induction Vectors" can be created where discontinuities in the response indicate a conductor has been intersected. These vectors lying in the plane of the conductor and pointing at the nearest edge provide a guide for modelling the conductor shape.

At each computation the conductor geometries and the session state are time-stamped and stored. This enables features such as conductor model "undo" and the "Results Timeline" interface which allows the user to scroll through a time sequence of modelling results while viewing the fit to a particular profile or borehole. The current state of the session can be reset to any point along the timeline allowing the interpreter to proceed from the previous "best fit".

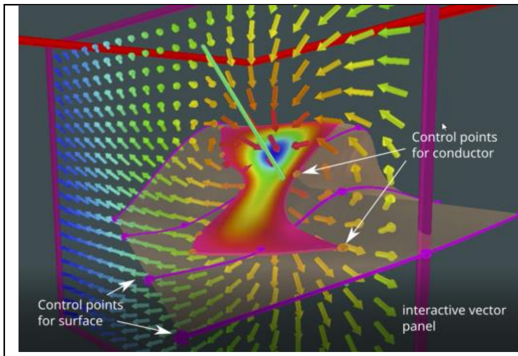

Figure 6. Response of Provus model showing the computed secondary field on a freely movable vector panel.

The Provus user directs the simulations with "Simulation Requests". Each named SR specifies a group of data and model conductors for simulation. These allow the interpreter to minimize computation times by focusing the simulations on a subset of the larger project. Further optimization is provided by automatic pruning of transmitter loop vertices.

Effective modelling requires knowledge of the geological context both for inspiration and for applying hard constraints. Provus provides an automated link to Geoscience Analyst, a full featured application for viewing and interacting with geoscientific data. As model conductors are created and modified they are transmitted to an identified GA session running concurrently via a Python interface. This allows for the assessment of the model conductor geometry and conductance relative to mapping, geochemistry, borehole lithology and structure.

Inversion

A facility for semi-automatic optimization of model parameters and control points is critical for Provus to be efficiently applied to complex modelling projects involving lots of historic data. Electromagnetic inversion can be highly non-linear, and even in the case of Provus, computationally expensive enough that a systematic and comprehensive search through the parameter space is infeasible. We are implementing what we are calling a *user-guided inversion*, which aims to seamlessly integrate inversion tools into the plate modelling workflow. Through GUI controls the interpreter can quickly isolate specific model parameters for inversion, such as selecting an individual plate, or particular node or edge of that plate for inversion. Specific regions of the EM profile data can be highlighted using GUI controls, to focus the inversion onto specific anomalies, or particular data components. We are using techniques such as truncated singular value decomposition to stabilize convergence.

Case History

In early 2022 Novaminex was asked to apply our new modelling application to the definition of a quartz-diorite (QD) hosted Ni-Cu deposit in Sudbury. The target (Zone A) is a small deposit hosted within the QD dyke environment below a much larger deposit. The zone is characterized by borehole UTEM data collected in six holes. The deposit is localized in a local flexure in the dyke, a situation favoured for sulphide accumulations. These deviations from an ideal tabular form added to the challenges posed by estimating the deposit outline using planar, rectangular plate models. The dyke geometry was fairly well established by a large number of additional exploration holes that are not shown here.

To provide a Provus Canvas on which to define the model conductor a geological wireframe of the hanging wall dyke contact was loaded into Geoscience Analyst (GA) and a region of the dyke defined by digitizing a series of sub-vertical trajectories. These were used to create a Provus Ribbon Conductor file containing a token rectangular ribbon defined by four control points at its corners. Once in Provus, the ribbon editing facility was used to adjust the location and shape of the conductor on the Canvas. The Provus link to Geoscience Analyst allowed the model conductor to be viewed in GA in almost real time allowing the Canvas to be adjusted so that the intercept of the model with each hole was co-located with the mineral intercepts in the boreholes.

The outline of the deposit was modified by adding and moving control points defining its outline until the relative locations of the edges were consistent with previous plate interpretations. From this point the modelling began.

As is common for nickel sulphide mineralization in Sudbury, the UTEM responses of these 4Hz base frequency surveys do not significantly decay by the latest channel therefore it is only the latest channel that has been modelled. The conductance has been set to the minimum required to result in the absence of discernable decay (20,000S). The final model of the target Zone A seemed to well define the deposit limits along strike and at depth (Figure 7). Holes M-5 and M-6 have anomalies explained by steeply plunging edges on the east and west limits of the deposit and Holes M-9 and M-K having off-hole responses indicating the lower edge of the conductor above the hole.

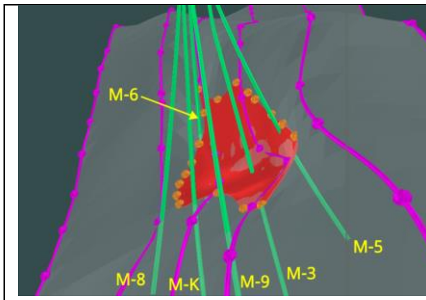

Figure 7. Zone-A modelled by a Provus Ribbon Conductor (red) within a Provus Canvas conformal with a QD offset dyke (translucent). The conductor shape is controlled by the orange control points while the Canvas shape is controlled by the fuchsia control points. View quasi longitudinal, angled upward with East to the right.

The modelling required modification of the Provus Canvas and the Ribbon Conductor using their respective control points. Figure 7 shows the final model for Zone-A with its control points in orange and the control points of its Canvas in fuchsia. While control points can be moved in a fluid and intuitive way with the mouse, keyboard shortcuts (W/A/S/D/I/O) are useful in orchestrating finer adjustments to the Canvas and Conductor control points in the Cardinal directions of the local coordinate system of the Canvas.

The process of data fitting requires the comparison of observed data and synthetic data on the same plot. Provus provides an interface for specifying groups of profiles for comparison on a panelled plot. Any computed results from completing Simulation Requests are pushed to the relevant active plot groups. Figure 8 shows the plot group created for modelling the data from hole M-5 near the eastern edge of the deposit. The late time eddy current is visualized by the current potential painted on the surface. The contours of this function are the streamlines of the eddy current. The centre of vorticity is biased to the bottom of the deposit owing to poorer coupling of the top of the deposit along with "inductive limit" state of current decay. The secondary vector field of the eddy currents is visualized on a separate movable panel.

Initial attempts to model the response of hole M-5 failed to establish an edge geometry fitting the character of the transverse “U” and “V” components along with the neutral response of the axial “A” component. An induction vector (“IV”) was created using a built-in facility which uses the discontinuity in the magnetic vector field across the conductor intercept for a specified time gate to generate a vector lying in the plane of the conductor and points towards its nearest edge. The IV (shown as the red arrow in the figure) was significantly discordant with the Canvas established from the geological model. Guided by the IV the local shape of the Canvas was modified resulting in a much improved data fit.

The modelling exercise was expanded to include holes peripheral to the original group of six. Hole P-0 intersected the QD dyke between the main deposit and Zone A (Figure 9) The main deposit was brought into Provus in a similar fashion using GA to digitize the dyke geometry from the geology wireframe. The outline of the deposit was also digitized as a closed 3D polyline loaded into Provus. A Provus Ribbon conductor was created interactively to match the Main Deposit outline. Figure 9 shows the UTEM data and computed response of channel 1 for Hole P-0. The broad anomaly due to the main deposit departs significantly from the observed response, especially in the “V” component however resolving the geometry of the main deposit was not addressed at the time. Nature of the punctual response near station 1200 has

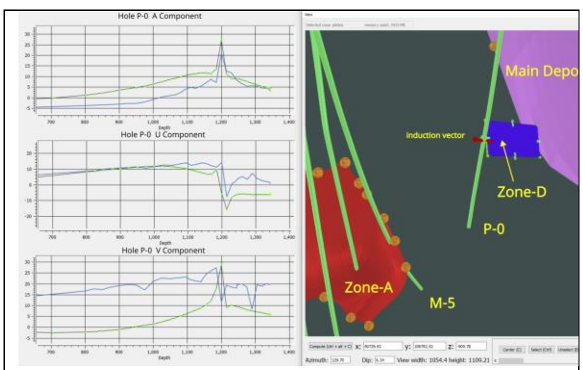

Figure 9. Plate model of “Zone D” (blue), an apophysis of mineralization extending below and to the west of the main deposit.

investigated using a rectangular plate model (blue) together with the Provus Ribbon model of the main deposit. Modelling the orientation of the nearest edge was guided by the use of an induction vector created using the data from stations 1180 and 1220, just above and below the mineralized horizon. The resulting plate model suggests an apophysis of mineralization extending below and to the west of the main deposit and terminating very close to the hole.

Project State and Future Developments

As of March 2023 Provus is limited to fixed-loop EM systems. While it has proved itself useful in its present state development continues with emphasis on inversion, moving transmitter systems and user interface elements to make modelling more efficient. We are also implementing several inversion algorithms and approaches to recover single, or multiple conductors.

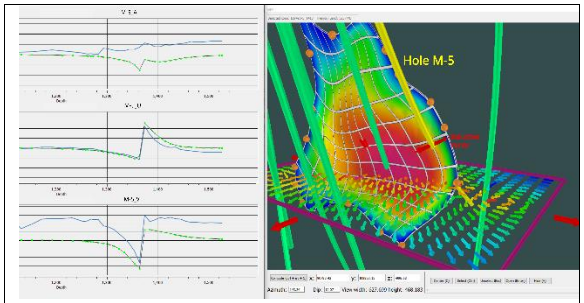

Figure 8. Modelling results from hole M-5 shown in custom plot group after adjusting near edge with aid of an induction vector.

Conclusions

The algorithm and approach described here is a practical next step to extract more information from EM data. By simulating the response of more realistic conductors it will be possible to strive for models that simultaneously explain all available data and by doing so provide models to the exploration team that more accurately reflect targetable mineralization.

Acknowledgements

I would like to thank Talon Metals for providing the financial support in 2021 to get Provus off the ground.

I thank Vale Exploration Canada Ltd for engaging Novaminex to tackle a challenging modelling problem with unproven code. The early application of a new technology to “real world” problems is incredibly useful for finding bugs and focusing refinements.

References

A.P. Annan - The Equivalent Source Method for Electromagnetic Scattering Analysis and Its Geophysical Application, Ph. D. Thesis, Memorial University of Newfoundland, January 21, 1974.

Petrophysical signatures and mineral endowment: The Piché group, Rouyn-Noranda, Quebec

[1]Yasaman Nemati, [1]J. Christian Dupuis, [2]Bernard Giroux, [3]Richard Smith, [1]Rita Rodrigues, and [1]Bertrand Rottier*
[1]Université Laval, Department of Geology and Geological Engineering, [2]Institut national de la recherche scientifique, E.T.E. [3]Laurentian University, Harquail School of Earth Sciences.

Summary

As mineral exploration activities seek deeper targets, understanding the petrophysical signature of geological processes at depth is fundamental to leverage critical information from geophysical datasets. Hydrothermal processes are responsible for mineral enrichment. So, we investigated the signatures of carbonate, chlorite, and sericite alteration in the Rouyn property, which is an orogenic gold deposit within the Superior Province of the Abitibi Greenstone Belt.

Orogenic gold deposits account for more than 75% of global historic gold production. The study area of this project spans 12 km along the longitudinal section of the Cadillac-Larder Lake Deformation Zone (CLLDZ) near Rouyn-Noranda, Québec, Canada. The Piché Group (Piché) is the principal host of gold mineralization in this area. This group is mainly composed of komatiites altered to carbonate schists through hydrothermal alteration.

Petrophysical data were acquired in four endowed and three non-endowed boreholes. Boreholes in the endowed portions of the property show an increase in the variance of resistivity values that are five times larger than their non-endowed counterparts. These same boreholes show a reduction in the variance of the induced polarization. In the non-endowed sections of the boreholes, the resistivity values measured at 8 and 64 inches are quite similar which provides evidence of a homogeneous rockmass. In the endowed sections, the resistivity measurements at 64 inches can be up to five times higher than the resistivity measured at 8 inches. Optical Televiewer results and core images show that the endowed sections have more quartz and carbonate veins which correspond to their higher resistivity seen on these logs. Micro-XRF results on core samples from the Piché revealed that the non-endowed sections have unevenly sorted and distributed pyrites while the endowed sections have a more uniform distribution of pyrite with smaller mineral grains. Thus, we see that the variations in the resistivity and IP data stem from changes in texture, which are linked to alteration processes that have led to the formation of veins and to mineral deposition. These results are an important step in understanding how the scale effects affect electrical measurement downhole and how these can be used to understand alteration in-situ. They will also contribute in understanding how these measurements can be upscaled for surface campaigns.

Introduction

The Abitibi sub-province is located in the southeastern part of the Superior Province and hosts some of the richest mineral deposits in the world. The Rouyn property, in the Abitibi sub-province, spans 12 kilometers along the E-W trending and N-dipping (60–80º) Cadillac-Larder Lake Deformation Zone (CLLDZ) near Rouyn-Noranda, Québec, Canada. This area is host to ultramafic and mafic rocks of the Piché Group (Piché), volcanic rocks of the Blake River Group, and sedimentary rocks of the Timiskaming Group. This property comprises six contiguous blocks, named from west to east: Augmitto, Cinderella, Lac Gamble, Astoria, East-Bay, and Bouzan. The CLLDZ strikes along the entire property and ranges in width from 55 to 120 meters. The Piché is known as the physical manifestation of the CLLDZ (Bedeaux et al., 2018) and constitutes the main target for gold exploration in the area. The lithologies comprising the Piché show evidence of alteration and deformation (Salmon and McDonough, 2011; Bedeaux et al., 2017). Alteration is expressed as carbonization, chloritization, and sericitization, portraying the classical assemblages associated with orogenic gold systems. Mineralization occurs as free gold in quartz-carbonate veins or as inclusions and/or filling of fractures within sulfide minerals (Salmon and McDonough, 2011). The Rouyn property was previously run by Yorbeau Inc. and very recently IAM Gold company has taken over the area. According to Yorbeau Inc. definitions, sections of the property are characterized as non-endowed or endowed when gold grade thickness associated with Piché units are lower or higher that 5g/t/m, accordingly. For the purpose of this project, we have retained this nomenclature.

Gold mineralization is unevenly distributed throughout the Rouyn property. In the study area, both the thickness and the endowment of the Piché decrease towards the East, with the Western sector representing the most prospective areas. Once we reach the East-

Bay and the Bouzan blocks there is no gold endowement.

The borehole geophysical data were collected from four endowed and three non-endowed boreholes. Since the boreholes from the East Bay and Bouzan blocks were in poor shape because they were drilled several decades ago, we chose the less endowed boreholes from the Gamble and Astoria blocks to represent the less endowed end-member in our analysis. The data acquired in every borehole included spectral Gamma Ray (SGR), caliper, resistivity, full-waveform sonic, Induced Polarization (IP), Optical TeleViewer (OTV), and magnetic susceptibility.

In the studied boreholes, the Piché is comprised of the following lithologies: Carbonate-Schist (M1Cb), Talc-Chlorite-Schist (M1TC), and Fuchsite-Carbonate-Schist (M1CbFu). Gold endowment is generally associated with the M1CbFu lithology.

Methodology

It is well known that mineral alteration processes, can significantly affect the nature of rock. Hydrothermal alteration processes in the ultramafic rocks of the Rouyn property, have produced chlorite, talc, micas, carbonates, and many other minerals. They may also change the shape, size, and disposition of minerals within the matrix. The petrophysical effects of alterations remain poorly understood compared to the lithological effects of alterations. Dentith et al. (2017, 2020) developed a conceptual framework for petrophysical data by placing the physical properties of rocks in a ternary diagram (Figure 1) with the end members of “bulk (overall composition)”, “grain (amount, size, and shape of minority mineral phases)”, and “texture (geometric relationships between grains)”. The bulk, grain, and texture (BGT) petrophysical model is a concept that helps scientists predict how geologic processes like alteration, may affect the physical properties of rocks.

Hydrothermal alteration associated with orogenic gold deposits results in the modification of the composition of the rocks. This alteration is usually manifested both as background (affecting the matrix of the rock) and vein formation (classic quartz-carbonate veins). In both scenarios, sulfidation is usually present, i.e., formation of sulfide minerals (e.g., pyrite, arsenopyrite, pyrrhotite).

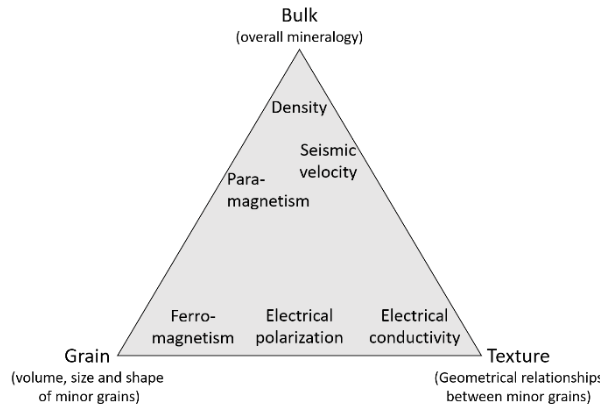

Figure 1—BGT ternary diagram of rocks’ physical properties (Dentith et al., 2017, 2019).

The veins and sulfides formed during this process change the textural characteristics of the rocks. For example, at the borehole scale, the presence of veins may block the passage of electrical current and cause accumulation of charges. Additionally, the presence of sulfide can also intensify the accumulation of charges. We anticipate that the textural modifications resulting from hydrothermal alteration affect the associated IP and resistivity responses.

Results and Discussions

To evaluate the effects of hydrothermal alteration, we cross-plotted the IP data against the resistivity data for the electrodes spaced 64-inch apart. The measurements presented here (Figure 2) are for sections of Piché with M1Cb, M1TC, and M1CbFu lithologies in endowed and non-endowed boreholes. The endowed sections show a higher variance in resistivity values compared to the non-endowed sections up to 5 times more as seen in M1TC parts. Conversely, the IP data show a small variance in the endowed sections and greater variance in the non-endowed sections. This behaviour is seen in all three distinct lithologies within Piché.

Since gold endowment is the result of hydrothermal alteration, we consider that the non-endowed sections have undergone less alterations. The fact that the endowed sections have a higher variance for the resistivity values, is because of the presence of quartz and carbonate veins that significantly affect the measurement. To test the idea that veins may be responsible for the increased resistivity values, we used the OTV and core images to count the number of veins and fractures within the Piché for each well. The OTV and caliper results showed that very few fractures are found within these boreholes and cannot be the cause of the resistivity variations that are observed. The number of veins identified on the OTV images, however, correlate very well with the resistivity changes as seen in Figure 3. The data in Figure 3 are for a portion of the Piché that is found in a non-endowed borehole. They show the results of averaging the resistivity values over 64-in sections and counting the number of veins within the same section. As the veins had various apertures, we multiplied the number of veins by the average aperture within that section. This figure expresses that areas with a greater number and thicker veins exhibit higher resistivities. According to this figure, we consider that the Piché in this well is more altered between 103m to 132m compared to the start and end parts.

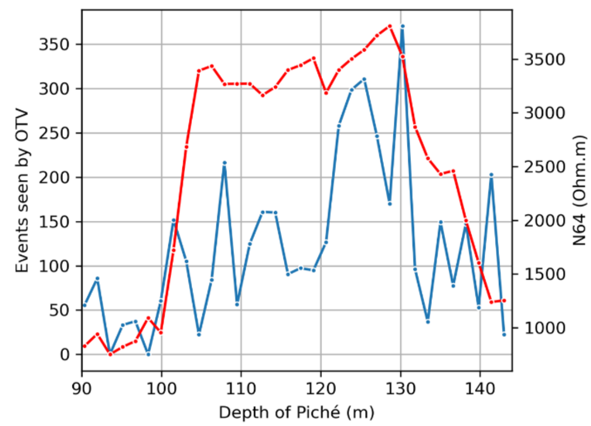

Figure 3—N64 and the number of veins multiplied by their average apertures for the Piché in Ga-20 well. The red color shows the averaged N64 resistivity, and the blue color shows the number of veins multiplied by the average aperture of the veins within that section. The middle parts show a higher number of veins and higher resistivity values compared to the start and end parts.

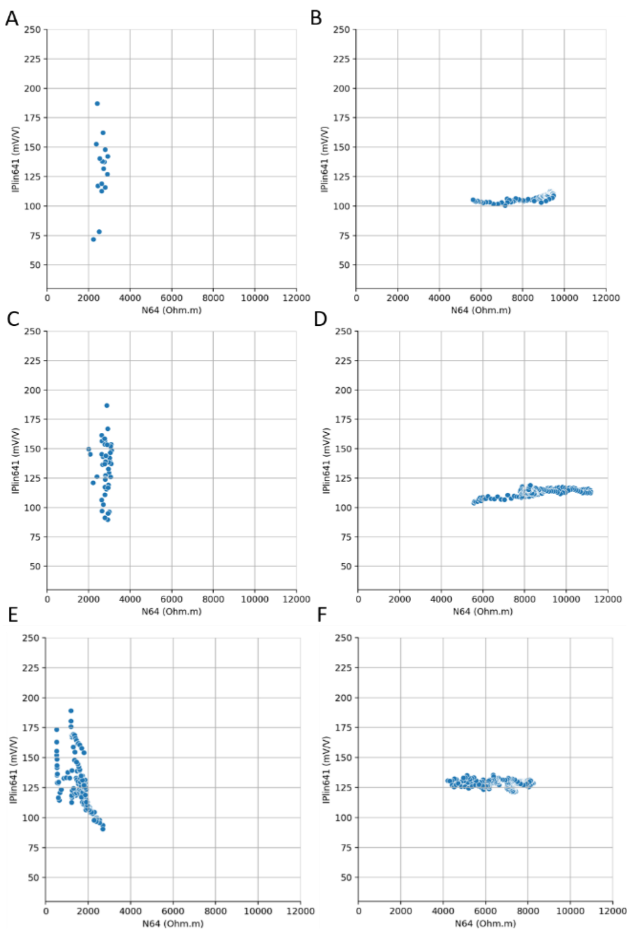

Figure 2—IP64-N64 plots for sections of Piché. A) non-endowed M1Cb, B) endowed M1Cb, C) non-endowed M1TC, D) endowed M1TC, E) non-endowed M1CbFu, F) endowed M1CbFu.

To understand the scale effects on the resistivity measurements, we plotted the resistivities measured over 8 and 64 inches in endowed and non-endowed parts of Piché. The results are shown in Figure 4. Our results reveal that in the non-endowed sections, the resistivities measured over different electrode spacing show what appears to be a one to one correspodance. In endowed sections, however, the N64 values are up to 4 times greater than the N8 measurements. We consider that these greater N64 values are caused by the presence of more resistive veins (quartz and carbonate) in the rock column in the endowed sections. These observations correspond well with the previous plots and the idea that these sections have undergone more alteration and deformations compared to the non-endowed parts.

The lower variance seen for the IP responses from endowed sections in Figure 2, can be explained by higher consistency in the shape, size, and distribution of chargeable materials such as pyrite. To investigate this matter, we performed micro-XRF analyses on core samples. For each lithology, one core sample was selected from an endowed section and another from a non-endowed section. Micro-XRF results for M1TC portions of the Piché are shown in Figure 5. Multi-elemental maps from the non-endowed section show high concentration of pyrite. The shape and size of pyrite grains vary considerably across the sample. Conversely, multi-elemental maps from the endowed section show a significantly lower concentration of pyrite. When present, pyrite grains tend to be more homogeneous in size and shape.

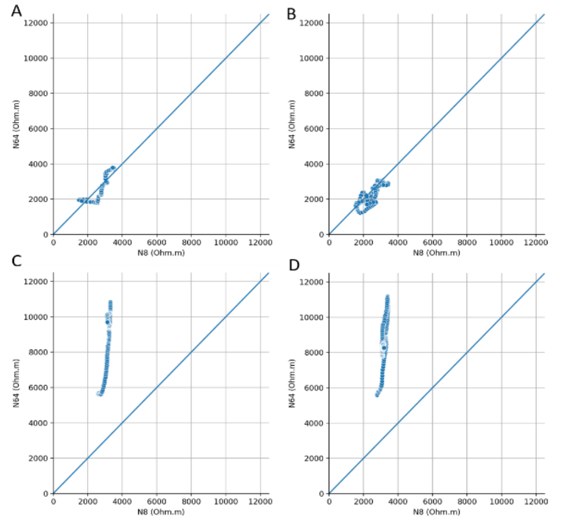

Figure 4—N8-N64 plots in Piché. A) non-endowed sections of M1Cb, B) non-endowed sections of M1TC, C) is for the endowed sections of M1Cb and D) is for the endowed sections of M1TC.

We consider that in the non-endowed parts, pyrite grains present a greater surface area which can lead to electrode polarization at the grain boundaries. The variance of IP observed in these zone is likely dominated by the variable abundance of pyrite. For the endowed sections, pyrite has mostly been destabilized and what remains has significanlty less surface area. This leads to lower IP values in general and a much more uniform distribution of values.

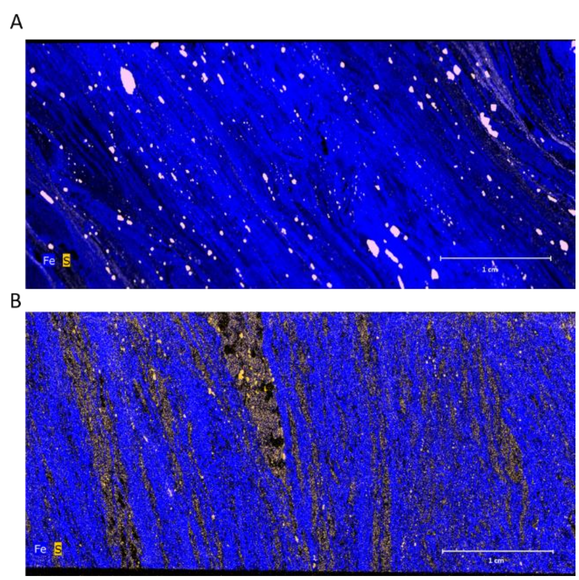

Figure 5—Micro-XRF multi-elemental maps of core samples from M1TC portions of Piché from A) non-endowed B) endowed sections. Blue and yellow colouring show Fe and S contents. Pink-coloured phases illustrate the presence of pyrite (FeS_2).

Conclusions

Petrophysical data can provide valuable information in mineral exploration, but they have not been utilized to their full potential. In this work, we have shown that even a relatively simple set of electrical measurements can yield insights into hydrothermal alteration processes. We showed that non-endowed rocks in this area, have undergone less intense alterations compared to the endowed rocks. This hypothesis was supported by comparing the relationship between IP and resistivity data along with the number and aperture of the veins. We showed that the resistivity at longer offsets are strongly influenced by resistive veining. The micro-XRF results from endowed and non-endowed sections of Piché confirmed that the grain size and texture changes have an effect on the IP measurement that are made. The next step is to acquire more micro-XRF data and quantify the mineral textures further to understand how they affect the measurements that are made downhole. We are also investigating how these findings can be upscaled and included into inversion models for surface data.

Acknowledgments

We would like to thank the Metal Earth team for their financial support for this work. This study was funded by them, and the Metal Earth publication number is MERC-ME-2022-43. We would also like to offer thanks to the Yorbeau Inc. team, especially Mr. Baptiste Chapon, for providing the necessary data and help. We sincerely appreciate ALT for supplying us with the software to perform the data analysis. We thank the Micro-XRF lab team at Laval University for their help in acquiring the micro-XRF images. Finally, we would like to thank Brandon Hume for all his help during the data collection campaign in the summer of 2022.

References

Bedeaux, P., Pilote, P., Daigneault, R. and Rafini, S. (2017). Synthesis of the structural evolution and associated gold mineralization of the Cadillac Fault, Abitibi, Canada; Ore Geology Reviews, v. 82, pp. 49–69.

Bedeaux, P., Mathieu, L., Pilote, P., Rafini, S. and Daigneault, R. (2018). Origin of the Piché Structural Complex and implications for the early evolution of the Archean crustal-scale Cadillac—Larder Lake Fault Zone, Canada; Canadian Journal of Earth Sciences, v. 55, no. 8, pp. 905–922.

Dentith, M., Adams, C. & Bourne, B. T. (2017). Petrophysics and exploration targeting best practice and applications. In: Wyche, S. & Witt, W. K eds. TARGET 2017. Perth, Australia: abstracts: Geological

Survey of Western Australia, Record 2017/6, Accessed online from Geoconferences WA, 37-39.

Dentith, M., Enkin, R. J., Morris, W. A., Adams, C. & Bourne, B. (2020). Petrophysics and mineral exploration: A workflow for data analysis and a new interpretation framework. Geophysical Prospecting.

Salmon, B., McDonough, B. (2011). Report on the Rouyn property—Augmitto block, Rouyn-Noranda, Quebec, Canada, Yorbeau resources, NI 43-101 Report.

Fatiando a Terra: Open-source tools for geophysics

Santiago R. Soler and Lindsey J. Heagy*
Department of Earth, Ocean and Atmospheric Sciences, University of British Columbia

Summary

In this talk, we will present the Fatiando a Terra project, a collection of open-source Python libraries designed for geophysical applications. We will describe how the project has grown from its start as a simple library part of a PhD Thesis in South America to a production-quality codebase, and how it created a community around it that actively collaborates to its development and its current state. We will introduce the tools available in the project and show examples with field data of how they can be used to solve geophysical problems. Finally, we will discuss some of the current challenges and mention the upcoming features and development plans for the future.

Introduction

Advancements in computing, from the origins of silicon-based chips, the development of numerical solvers and the advent of multiprocessing have each enabled new opportunities to solve larger and more complex problems in geophysics. Software developed by researchers and industry professionals enable us to process large amount of data, generate visualizations for interpretation, and ultimately to perform inversions to build models of the subsurface. All of which are key to improve decision-making processes. Although much of this software was built as in-house tools, the appearance of open-source software for geosciences happened as early as the 70s and 80s. Projects like Seismic Unix (Stockwell, 1999) and GMT (Wessel et al., 2019) are pioneer examples.

In recent decades, the popularity of the Python language amongst every scientific field planted the seeds for an ever-growing open-source geoscientific ecosystem. Python tools aimed at solving geoscientific problems have proliferated, and there are now open-source tools that span geologic modelling, data processing, inversion, visualization, and much more.

In this setting, Leonardo Uieda created the Fatiando a Terra project (Uieda et al., 2013; https://www.fatiando.org) aimed at developing open-source Python tools for geophysics. It started in 2010 as a single Python library as part of his PhD Thesis in South America. Being available under an open-source license and its clear and comprehensive documentation have facilitated its use by researchers and industry professionals from different regions of the world. Some of these users have since become contributors by writing new features, fixing bugs, adding more tests, improving the documentation or having an active participation in its community. Now, the Fatiando project has over 30 contributors, and it continues to grow using a community-driven model.

The main goal of the project is to provide open-source software tools that are easy to use and also well designed, tested, and documented. Nowadays, it consists in a set of Python libraries, each one of them with a very specific scope of application. These libraries offer software solutions for downloading and caching data from the web, handling and interpolating spatial data, computing normal gravity of reference ellipsoids using analytic solutions, processing potential fields data with frequency-domain filters, forward modelling gravity and magnetic fields of different geometrical bodies, and gridding harmonic data with equivalent sources.

During this talk we will provide an overview of the tools available in the project and demonstrate their functionalities using examples from research and industry applications.

The Project

In its origins, Fatiando a Terra consisted of a single Python library named fatiando (https://legacy.fatiando.org) that used to host all the features that the project offered. After years of development, this design approach proved to be flawed. The large size of the code base made it difficult to maintain and to extend its functionality. Further, the code contained in this library varied greatly in scope and maturity, ranging from toy problems meant to be used for educational purposes to production ready tools.

In 2018 the community decided to redesign the code base by splitting the old fatiando library into several smaller libraries, each one with a very specific scope. This simplifies both the adoption of the libraries and also their development. Most users look for only a subset of the tools offered by the project, and having them divided in libraries reduces the size of the libraries they depend on. As a side effect, anyone interested in changing the code of one of our libraries now needs to familiarize themselves with a smaller code base, making it easier for new contributors to collaborate to the project.

In parallel, the broader geoscientific Python ecosystem has seen a major growth. Libraries like SimPEG (Cockett et al., 2015), GemPy (de la Varga et al., 2019), pyGIMLi (Rücker et al., 2017) and ObsPy (Obspy, 2019) were established. These projects provide scientists and industry with a wide range of tools for research and exploration. As a project, we decided to invest in the strengths of the Fatiando libraries in light of the broader ecosystem. The introduction of smaller, and narrowly scoped libraries has again been advantageous as it allows other projects to use them without introducing a large set of unnecessary dependencies. The project is currently formed by five libraries: Verde, Boule, Harmonica, Pooch and Ensaio.

Verde

Verde hosts tools for spatial data processing, interpolation, and gridding. Its core interpolation methods are inspired by machine learning, hence its interface reassembles one of the popular machine learning Python packages, Scikit-learn (Pedregosa et al., 2011). Additionally, it offers analysis tools that accompany the interpolators, such as trend removal, windowing operations, cross-validation, k-folding, grid projection, and more coordinate manipulation utilities.

Boule

Boule is a very lightweight library that hosts classes for representing geodetic reference ellipsoids for the Earth and for celestial bodies of the solar system like the Moon, Mars, Venus, and Mercury. These classes also offer methods to perform coordinate conversions between geodetic and geocentric spherical systems, and to compute the normal gravity generated by these ellipsoids on any external point through a closed-form analytic solution (Li and Götze, 2001).

Harmonica

Harmonica offers functions and classes for processing and modelling gravity and magnetic data. It hosts functions for forward modelling the gravity fields of point sources, rectangular prisms and also tesseroids (a.k.a. spherical prisms). It can perform gravity corrections, from a simple Bouguer correction to a full terrain correction, by forward modelling digital elevation models with prisms. Regular grids can be transformed using FFT-based filters including upward derivative, upward continuation, and reduction to the pole, amongst others. It also offers ways to perform interpolation, gridding, and upward continuation through the equivalent sources technique. Finally, it can also read data stored in popular formats like .gdf files provided by the ICGEM Calculation Service and .grd files from Oasis Montaj©.

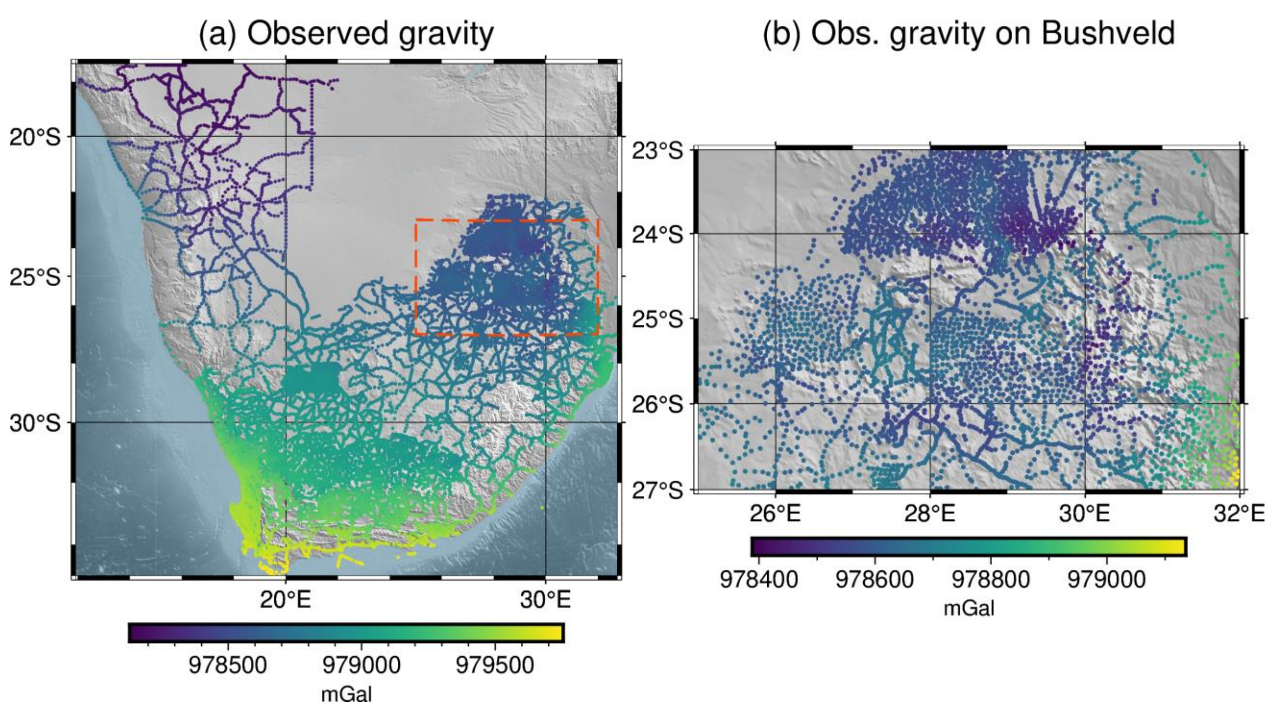

Figure 1. Gravity data over Southern Africa: (a) observed gravity data and box delimiting the boundaries of a region that contains the Bushveld Igneous Complex, (b) observed data limited to the region around the Bushveld Igneous Complex. Data made available by NOAA NCEI and downloaded using Ensaio.

Pooch
The most general purpose library in the project is Pooch, which offers an easy-to-use interface for downloading and caching data from the web. Originally designed for scientific applications and to be used by other software packages, Pooch can download data from the web through a large range of protocols, cache it locally at a desired location, and also check the integrity of those files. This simple but powerful library is currently being used by other projects in the scientific Python stack, like SciPy (Virtanen et al., 2020), scikit-image (van der Walt et al., 2014), MetPy (May et al., 2016) and icepack (Shapero et al., 2020), amongst others.

Ensaio
Lastly, we introduce Ensaio, a small library that hosts open licensed datasets that are useful for running examples and tutorials, for teaching, and for probing our codes. It uses Pooch under the hood to download and cache those datasets locally, so its codebase ends up being very slim.

Example: Gravity data over South Africa

We can use Ensaio to easily fetch some curated datasets. For example, let's download a gravity dataset over Southern Africa (made available by NOAA NCEI):

```
import ensaio
ensaio.fetch_southern_africa_gravity(
   version=1
)
```

Figure 1 shows plots of the downloaded gravity data over Southern Africa (Fig. 1a), and a cropped region focusing on the Bushveld Igneous Complex (Fig. 1b).

Using Boule we can define an object that represents the WGS84 reference ellipsoid and use it to compute the normal gravity, i.e. the gravity acceleration of the reference ellipsoid on every observation point:

```
import boule as bl
ellipsoid = bl.WGS84
ellipsoid.normal_gravity(
   data.latitude, data.height
)
```

By removing the normal gravity from the observed gravity we can obtain the gravity disturbance (see Fig. 2a).

In order to obtain the Bouguer gravity disturbance we need to remove the terrain effect from the gravity disturbance we already computed. Harmonica allows us to compute the gravity effect of the topographic masses on every observation point by approximating them with rectangular prisms with a specified density and forward modelling them (see Fig. 2b)

```
import harmonica as hm
density = np.where(
   topography > 0, 2670, 1040 - 2670
)
model = hm.prism_layer(
   coordinates=(
      topography.easting,
      topography.northing
   ),
```

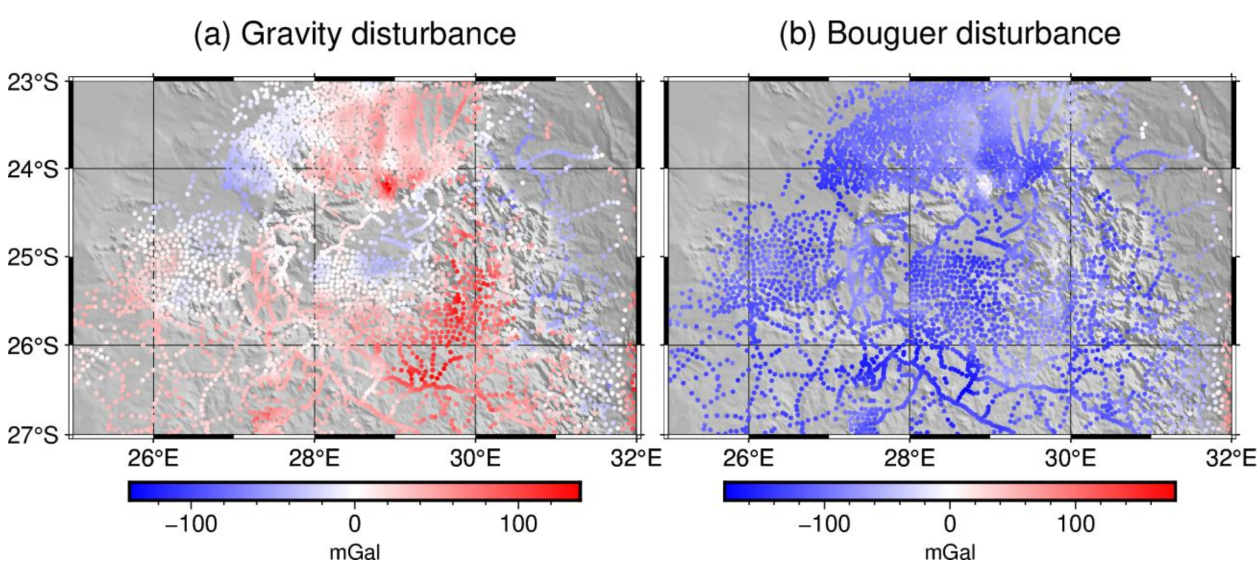

Figure 2. (a) Gravity disturbance over the Bushveld Igneous Complex. (b) Bouguer gravity disturbance obtained after removing the terrain effect from the gravity disturbance.

```
    surface=topography,
    reference=0,
    properties={"density": density},
)
terr_eff = model.prism_layer.gravity(
    coordinates, field="g_z"
)
```

To achieve the goal of obtaining the gravity effect of the shallower masses we need to split the residual field from the regional field. We can use Harmonica to generate the regional field using deep equivalent sources (see Fig. 3a).

```
deep_sources = hm.EquivalentSources(
    damping=1000, depth=500e3
)
deep_sources.fit(
    coordinates, gravity_bouguer
)
regional = deep_sources.predict(
    coordinates
)
residual = gravity_bouguer - regional
```

Similarly, we can use Harmonica's equivalent sources to grid the residual field at a constant height (see Fig. 3b):

```
eq_sources = hm.EquivalentSources(
    damping=10, depth=10e3
)
eq_sources.fit(
    coordinates, gravity_residual
)
grid = eq_sources.grid(
    upward=2200,
    spacing=grid_spacing,
)
```

This example showcases how the tools available in the aforementioned libraries can be used together to process gravity data. The full code for running this example, along with a detailed explanation of the steps, can be found in https://www.fatiando.org/tutorials. Figures were produced using pyGMT (Uieda, 2022).

Conclusions

After more than a decade since the Fatiando a Terra project was started, the project continues to grow thanks to a network of collaborators and users that actively participate in its development. The success of the project has been enabled by having the code be openly-licensed and by promoting a community-driven model of software development. In addition to serving direct users, the benefits of the project extend more broadly as Fatiando libraries are relied upon by other projects in the scientific Python ecosystem. Furthermore, we have contributed to the advancement and adoption of best-practices in open-source software development within this broader community.

Fatiando has been used by students and researchers as core parts of their Thesis and scientific articles, and also by industry. The growing reliance on open-source tools by researchers and professionals highlights the importance of continued maintenance and development of these tools.

Plans for future development include the implementation of more efficient forward modelling

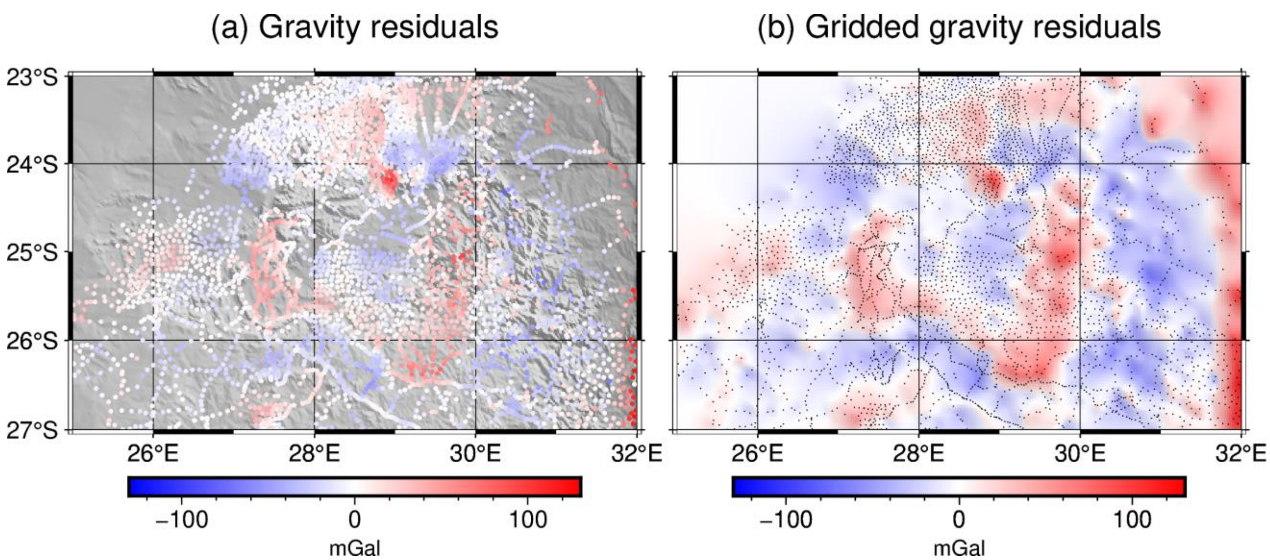

Figure 3. (a) Residual gravity field split using deep equivalent sources. (b) Gridded product of the residual gravity field at a constant height of 2200m above the ellipsoid.

functions for Harmonica as well as the expansion of functionality for equivalent source calculations and FFT-based transformations. Moreover, we plan to bring back the inversion framework that the old fatiando library had, with the opportunity of improving it with modern tools and focusing on types of inversions that are missing in other packages of the geophysical Python ecosystem.

We invite everyone to try out our tools, suggest new features, bring new use cases and especially make contributions to the code and documentation. The Fatiando website (https://www.fatiando.org/contact) has resources for getting involved.

Acknowledgments

We are indebted to the developers and maintainers of all the open-source software and particularly to the users and contributors of Fatiando a Terra.

References

Cockett, R., Kang, S., Heagy, L. J., Pidlisecky, A., & Oldenburg, D. W. (2015). SimPEG: An open source framework for simulation and gradient based parameter estimation in geophysical applications. Computers & Geosciences, 85, 142–154. https://doi.org/10.1016/j.cageo.2015.09.015

Harris, C. R., Millman, K. J., van der Walt, S. J., Gommers, R., Virtanen, P., Cournapeau, D., Wieser, E., Taylor, J., Berg, S., Smith, N. J., Kern, R., Picus, M., Hoyer, S., van Kerkwijk, M. H., Brett, M., Haldane, A., del Río, J. F., Wiebe, M., Peterson, P., … Oliphant, T. E. (2020). Array programming with NumPy. Nature, 585(7825), 357–362. https://doi.org/10.1038/s41586-020-2649-2

Hoyer, S., & Hamman, J. (2017). xarray: N-D labeled Arrays and Datasets in Python. Journal of Open Research Software, 5(1), 10. https://doi.org/10.5334/jors.148

Li, X., & Götze, H. (2001). Ellipsoid, geoid, gravity, geodesy, and geophysics. GEOPHYSICS, 66(6), Article 6. https://doi.org/10.1190/1.1487109

May, R., Arms, S., Marsh, P., Bruning, E., Leeman, J., Bruick, Z., & Camron, M. D. (2016). MetPy: A Python Package for Meteorological Data. UCAR/NCAR-Unidata. https://doi.org/10.5065/D6WW7G29

McKinney, W. (2010). Data Structures for Statistical Computing in Python. 56–61. https://doi.org/10.25080/Majora-92bf1922-00a

The ObsPy Development Team (2019). ObsPy 1.1.1 (1.1.1). Zenodo. https://doi.org/10.5281/ZENODO.1040770

The Pandas Development Team (2023). pandas-dev/pandas: Pandas (v1.5.3). Zenodo. https://doi.org/10.5281/ZENODO.3509134

Pedregosa, F., Varoquaux, G., Gramfort, A., Michel, V., Thirion, B., Grisel, O., Blondel, M., Prettenhofer, P., Weiss, R., Dubourg, V., Vanderplas, J., Passos, A., Cournapeau, D., Brucher, M., Perrot, M., y Duchesnay, E. (2011). Scikit-learn: Machine learning in Python. Journal of Machine Learning Research, 12:2825–2830.

Rücker, C., Günther, T., & Wagner, F. M. (2017). pyGIMLi: An open-source library for modelling and inversion in geophysics. Computers & Geosciences, 109, 106–123. https://doi.org/10.1016/j.cageo.2017.07.011

Shapero, D., Badgeley, J., & Hoffman, A. (2020). icepack: Glacier flow modeling with the finite element method in Python (v1.0.0). Zenodo. https://doi.org/10.5281/ZENODO.1205640

Stockwell, J. W. (1999). The CWP/SU: Seismic Un∗x package. Computers & Geosciences, 25(4), 415–419. https://doi.org/10.1016/S0098-3004(98)00145-9

Uieda, L., V. C. Oliveira Jr, and V. C. F. Barbosa (2013), Modeling the Earth with Fatiando a Terra, Proceedings of the 12th Python in Science Conference, pp. 91 - 98.

de la Varga, M., Schaaf, A., & Wellmann, F. (2019). GemPy 1.0: Open-source stochastic geological modeling and inversion. Geoscientific Model Development, 12(1), 1–32. https://doi.org/10.5194/gmd-12-1-2019

Virtanen, P., Gommers, R., Oliphant, T. E., Haberland, M., Reddy, T., Cournapeau, D., Burovski, E., Peterson, P., Weckesser, W., Bright, J., van der Walt, S. J., Brett, M., Wilson, J., Millman, K. J., Mayorov, N., Nelson, A. R. J., Jones, E., Kern, R., Larson, E., … Vázquez-Baeza, Y. (2020). SciPy 1.0: Fundamental algorithms for scientific computing in Python. Nature Methods, 17(3), 261–272. https://doi.org/10.1038/s41592-019-0686-2

van der Walt, S., Schönberger, J. L., Nunez-Iglesias, J., Boulogne, F., Warner, J. D., Yager, N., Gouillart, E., & Yu, T. (2014). scikit-image: Image processing in Python. PeerJ, 2, e453. https://doi.org/10.7717/peerj.453

Wessel, P., Luis, J. F., Uieda, L., Scharroo, R., Wobbe, F., Smith, W. H. F., & Tian, D. (2019). The Generic Mapping Tools Version 6. Geochemistry, Geophysics, Geosystems, 20(11), 5556–5564. https://doi.org/10.1029/2019GC008515

10 years of SimPEG - Recent developments and the next steps forward

[1]*Joseph Capriotti**, [1]*Lindsey J. Heagy*, [1]*Devin Cowan*, [1]*Johnathan Kuttai*, [2]*Seogi Kang*, [3]*Dominique Fournier*, [4]*Thibaut Astic*, [5]*Rowan Cockett*, [1]*Douglas W. Oldenburg, and the SimPEG Team.*
[1]*University of British Columbia, Geophysical Inversion Facility,* [2]*Stanford University, Stanford Environmental Geophysics Group,* [3]*Mira Geoscience Ltd.* [4]*KoBold Metals,* [5]*Curvenote Inc.*

Summary

SimPEG has been actively developed for over a decade, and in that time, it has grown from a white-board sketch into a platform used by researchers and industry professionals to solve geophysical problems. The framework allows for collaborative experimentation with new inversion methods and has shortened the time required for new researchers to start their own projects. The addition of sparse norms, and more recently joint inversions, has been driven by research in mineral exploration, hydrology, carbon mineralization, and a host of other applications. Current areas of development include large-scale electromagnetic inversions and the implementation of tetrahedral meshes.

Introduction

SimPEG (Cockett et.al. 2015) is an open-source simulation and inversion framework developed in python to support researchers and industry professionals in geophysics. It currently supports simulating and inverting gravity, magnetics, resistivity, induced polarization, frequency and time-domain electromagnetics, fluid flow monitoring, and seismic tomography data. The framework itself is general to the inverse problem of interest. Its goal is to promote collaboration between researchers in many different geoscience and numeric fields to enable new research by providing a verified, tested, and robust code base.

The SimPEG project was started 10 years ago at UBC and over that time it has grown to include an international community of academics and industry professionals. These community members drive SimPEG development, and this development is facilitated by open-source software practices including versioning code, tracking issues, testing code, suggesting and reviewing changes, holding weekly meetings, and providing a forum for discussion. Over these years the framework has evolved based on the feedback and needs of the community. This code is made freely available under a permissive open-source license for commercial and academic use at https://simpeg.xyz/.

SimPEG has evolved over the past decade and has been split into several Python packages that all work together to solve the geophysical inverse problem. There is the main SimPEG package which defines the geophysical simulation and inversion operations. Discretize, now a separately maintained and distributed package, was created from SimPEG's initial finite volume meshing package. It creates finite volume operators for common mesh types including rectilinear, quadtree, octree, triangular, tetrahedral, curvilinear, and cylindrical meshes. Discretize also provides operations for taking derivatives of those finite volume operators with respect to model parameters. The main SimPEG package then uses these operators to solve the numerical PDEs behind its simulations. The geoana package, which is also maintained as part of the SimPEG ecosystem, houses fast analytic functions for simple geometries and models. The main SimPEG package uses geoana, for example, to create primary fields for electromagnetic simulations in a primary-secondary simulation approach, or to model the gravitational response of a rectangular prism. We also maintain packages that interface to efficient linear solvers (pymatsolver) and are supporting the development of a library for processing of magnetotelluric data (aurora).

SimPEG development is driven by a combination of research needs and industry use. For example, current research in the use of gravity and magnetics for characterizing the alteration of ultramafic rocks for carbon mineralization leverages Petrophysically and Geologically Guided Inversion and has motivated the implementation of Cross Gradient and Joint Total Variation inversions (Astic and Oldenburg, 2019; Heagy et al., 2022). Active projects in hydrogeophysics are driving lateral and time constrained inversion approaches to stitched 1D EM inversions (Kang and Knight, 2022). We have also added support for unstructured mesh types in SimPEG to better account for models with rugged geometries (Capriotti et al. 2022).

Industry use and contributions have also been critical to success. Notably, the need to invert large 3D DCIP and potential fields data sets has driven developments to allow SimPEG to scale to large cluster computing environments using the dask library (Dask, 2016). Work is ongoing to improve efficiency of the modules for natural source, frequency, and time-domain electromagnetics. In addition to expanding functionality, we have significantly expanded the documentation and provided end users with many tutorials demonstrating SimPEG's use. This continues to be important for expanding the community and supporting new users and contributors.

In this work, we will introduce SimPEG and its general framework, and discuss how the project and community has evolved over the past decade. We will highlight recent developments with examples from research and industry applications. We conclude with an overview of the road ahead and avenues for getting involved in the project.

SimPEG Framework

SimPEG provides a common framework where the inversion problem is split into multiple different pieces (Cockett et al. 2015). These pieces are developed independently and then assembled to solve the inverse problem. The simulation is the largest chunk of the inversion problem. A simulation is defined as an object that supports the ability to predict data given a model and compute Jacobian and Jacobian transpose products with arbitrary vectors. This allows us to use these objects to perform the minimization operations required for inversion. SimPEG comes ready with multiple types of common simulations used in geophysics including gravity, magnetics, magnetotellurics, frequency and time-domain electromagnetics, travel time tomography, resistivity, induced polarization, and others. These simulations are tested for accuracy to both verify the implementation and provide a reliable base for researchers to build from. The inversion machinery is extensible, and if a user wants to invert data using a different simulation engine, they can instead create their own custom-built method that provides the predicted data and computation of sensitivities. The inversion machinery is extensible, and if a user wants to invert data using a different simulation engine, they can instead create their own custom-built method that provides the predicted data and computation of sensitivities.

The regularization portion of the inversion problem, used for underdetermined or ill-posed problems, is the next piece of the inversion. SimPEG contains several different regularization pieces capable of computing regularization measures on the norm of the model and the model's spatial gradients. Regularizations can be created with a variable l-p norm measure to produce models with sharper contrasts (Fournier and Oldenburg, 2019). By developing these operations independently of the simulation, a user can use the same regularization approach for a magnetotelluric inversion that they would for a gravity inversion.

The simulation and regularization objects are combined using composable objective functions that know how to evaluate themselves, calculate gradients, and perform (approximate) Hessian vector operations. The inversion is then constructed as a problem of minimizing an objective function. The user can choose from different minimization strategies appropriate to their particular problem including gradient descent, Gauss-Newton, projected Gauss-Newton, BFGS, and others. We then define directives that tell the inversion how to proceed. These directives are fairly general and widely scoped but generally modify the objective function in some way after an iteration. There are directives that update a model weighting matrix based on the sensitivity matrix (or Jacobian matrix at each iteration for non-linear problems), define a strategy to update the regularization parameter if a target data misfit is not reached, force the inversion to switch between an l-2 norm and l-0 norm at some specified iteration, and many others.

Together all the pieces of the framework (Figure 1) combine to form a concrete implementation of a SimPEG inversion. With these modular pieces it becomes straightforward to test multiple assumptions about your model space. SimPEG's modularity also allows one to create a sparse norm inversion of gravity data, then switch only the simulation object to instead perform a sparse norm inversion of resistivity data.

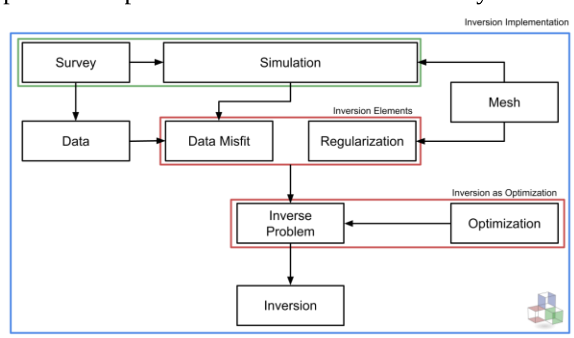

Figure 1: The SimPEG framework shows the general setup of an inversion. The process is broken into composable pieces that can be interchanged.

Community

Hello SimPEG initially started as an effort at UBC with the goal of helping accelerate research in geophysics by developing a common framework and set of tools for solving inverse problems, and importantly, also by fostering the growth of a community of geoscientists interested in solving problems with geophysical data. Since its start in 2013, the project has grown to include contributors from multiple academic institutions and companies worldwide. The diversity in skill-sets and interests of this community have been essential for driving development and improvements to the project. Research is a prime driver of new functionality, large-scale industry use cases have motivated improvements in efficiency, and educational and humanitarian projects have led to the development of tutorials and additional resources that facilitate the use of the code. We welcome contributions that span from developing code or documentation, to bringing new use-cases, to participating in discussions in meetings and on forums such as GitHub or Slack.

Examples

SimPEG development is primarily driven by an individual project's needs, but by building in a common framework and coordinating these efforts, each project can build from and extend off of the work of others. We highlight projects that have contributed recent developments to SimPEG and showcase ongoing projects that are directing the current path.

Fournier and Oldenburg (2019) developed the sparse norm inversions strategy used in SimPEG. In the implementation, different norms can be applied to each component of the regularization (e. g. the smallness and smoothness terms) with automated and balanced weightings. The same regularization functions and minimization strategies were applied to both a seismic travel time tomography inversion (Figure 2) and magnetic inversion using a common framework.

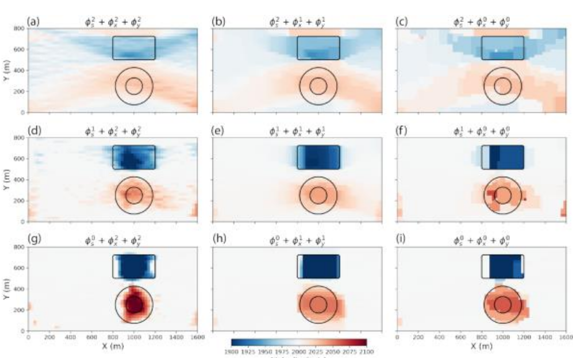

Figure 2: Suite of inverted traveltime tomography models with various norms applied to the smallness and smoothness terms of the model objective function from Fournier and Oldenburg, 2019.

Petrophysically and Geologically guided inversion (PGI) from Astic and Oldenburg, 2019, is a method of jointly inverting geophysical data and petrophysical data by iteratively updating weights in the regularization and reference models. A Gausisan mixture model describing the petrophysical data is used to update a quasi-geology model, which is in turn used to update the inversion's properties. While originally applied to inversions for a single physical property, it is also capable of linking multiple physical properties together for a joint inversion, Astic et al. 2021, Figure 3. This work formed the first additions of joint inversion capabilities to SimPEG.

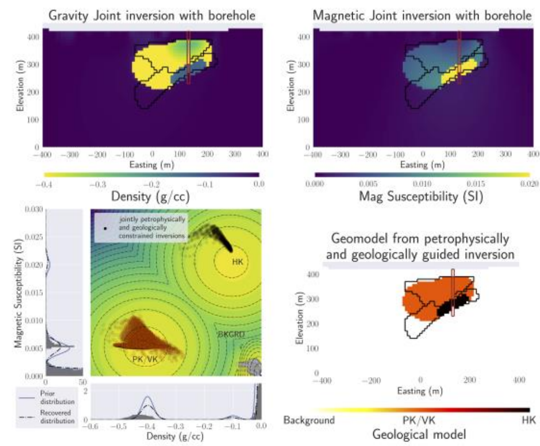

Figure 3: Joint inversion of gravity and magnetic data using the Petrophysically guided inversion framework from Astic et. al., 2021.

A recent project developing strategies for identifying and assessing carbon mineralization potential of serpentinites makes use of multiple aspects of SimPEG. Heagy at al., 2022, investigate how choosing different cutoff values for inversion models affects the estimated volume of serpentinized rock, and develop a general strategy based on inverting characteristic models. They applied the approach to gravity and magnetic inversion using traditional smooth inversions, sparse norm inversions, and PGI, showing how incorporating petrophysical information improved the estimate of volume with depth.

Another aspect of the carbon mineralization project, which is ongoing in partnership with industry, involves extending the overall joint inversion framework that was initially established for PGI to support structural based approaches. Cross-gradient (in collaboration with Wei and Sun, 2022) and joint-total variation methods have both been included in SimPEG and applied to the same representative example from Heagy et al. 2022, with results shown in Figure 4. The two different methods both fit into the framework of SimPEG and can be quickly exchanged.

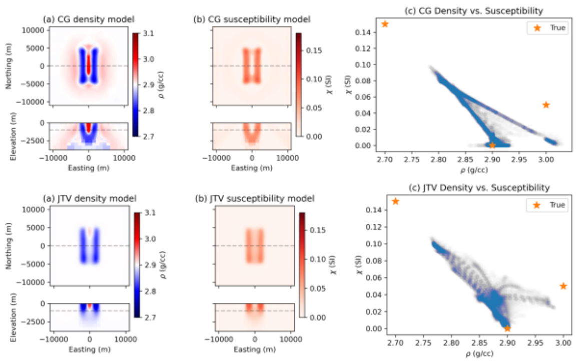

Figure 4: Cross-gradient (top) and Joint total variation (bottom) inversion of gravity and magnetic datasets over a synthetic example representative of serpentinite with zones in different stages of mineralization.

Kang and Knight, 2022, used repeated airborne time-domain electromagnetic surveys to monitor saltwater encroachment. While full 3D inversion is still an active area of improvement for SimPEG, 1D inversions at each sounding location are useful for interpretation and appropriate in many settings. The authors stitched multiple inversions together to perform a time-lapse laterally constrained inversion. They found that using the same sparse norm inversion measures developed for potential fields allowed for a more interpretable conductivity change in time (Figure 5). In collaboration with the SimPEG development team, they worked to add fast 1D time and frequency domain electromagnetic inversion capability to SimPEG, and continue to iterate on the addition of their laterally constrained and time-lapse inversion implementations to SimPEG.

Multiple projects have motivated the addition of triangular and tetrahedral mesh support to SimPEG. The laterally constrained inversion approach used for the hydrogeophysics problem regularizes a model defined at irregularly spaced locations. Triangular meshes also allow for accurate representation of rugged topographies and irregularly shaped bodies. Capriotti et al., 2022, extended the resistivity simulations to support triangular meshes and then performed inversion of a synthetic volcanic example (Figure 6). Using a spatial gradient regularization defined using inner product operators from discretize, they were able to obtain consistent results with previous axis aligned meshes.

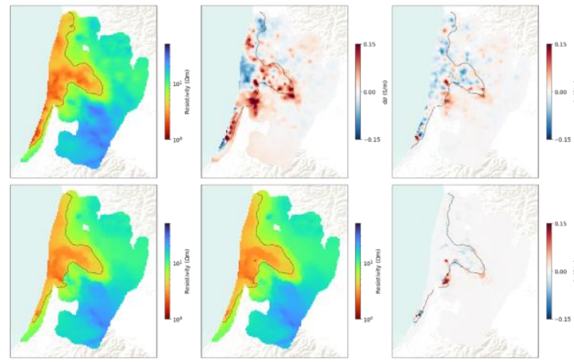

Figure 5: Time-lapse inversions of two airborne EM surveys from 2017 (left) and 2019 (center), with smooth gradient norms (top) and sparse gradient norms (bottom) applied in time. The sparse norm improved the image and highlights locations of saltwater encroachment (right). From Kang and Knight (2022).

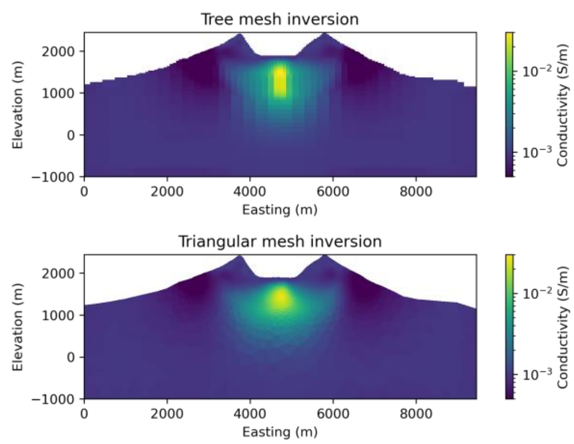

Figure 6: A comparison resistivity inversion results of an axis aligned tree mesh, and a triangular mesh using equivalent gradient regularizations. The rugged topography of this synthetic volcanic example requires fine cells for the tree mesh near the surface to accurately model the partial differential equations. From Capriotti et al., 2022.

A common need across all SimPEG projects is to improve its scalability by allowing inversions to benefit from cluster computing. There are several different methodologies for parallelizing the inversion that have been used with SimPEG (Capriotti et al. 2021), which were developed in cooperation with industry members to support large scale inversion problems. Not all approaches suit every problem, and the strategy depends on the setup. Numerical solutions to partial differential equations are naturally split over each individual source, assuming that a single worker can store the required matrix factorizations. Alternatively, another approach splits the mesh using the decoupling approach of Haber and Schwarbach, 2014, to reduce the size of the model space by creating local meshes that can be solved in parallel. We chose to implement the parallelism strategis in SimPEG using the dask framework (Dask 2016). Currently the gravity, magnetics, resistivity, and induced polarization simulations have optional dask parallelism. Meanwhile, other methods are currently being extended to support parallelization.

Conclusions

Over the years, SimPEG has provided a solid foundational framework of tested codes for geophysical practitioners to use for their own projects. It has also provided educational resources that facilitate an understanding of the interaction of geophysical fields with the subsurface, as well as the role that inversion plays in interpreting data. Generally, new users follow tutorials provided in the online documentation as a starting point and adapt them to their own problems. SimPEG has also fostered a global community of interested geophysicists through weekly meetings and providing online discussion boards where community members can engage in conversation about ongoing projects and solicit feedback and advice.

For researchers and industry professionals, SimPEG provides an environment that allows for active feedback and cooperation. It has also shortened the time to incorporate new research developments into production workflows. The collaboration amongst researchers, professionals, and students actively improves the codebase because multiple parties have a vested interest in seeing it succeed.

SimPEG currently provides production-level codes for simulating and inverting gravity, magnetics, resistivity, induced polarization, and electromagnetic data. Active areas of research continue to spur additions and improvements to SimPEG. Our current focus includes improving the efficiency of the electromagnetic simulations, implementing laterally constrained and time lapse inversions, allowing for flexible unstructured meshes, and development of joint inversion resources.

Acknowledgements

H The authors are grateful to the SimPEG community and to everyone who has contributed to its growth by adding to the codebase and participating in discussions. We are also grateful to the companies who have sponsored research at UBC-GIF which has helped enable continued maintenance and development of SimPEG.

References

B Astic, T., D. W. Oldenburg, 2019, A framework for petrophysically and geologically guided geophysical inversion using a dynamic Gaussian mixture model prior, Geophysical Journal International, 219, 1989–2012.

Astic, T., L. J. Heagy, D. W. Oldenburg, 2021, Petrophysically and geologically guided multi-physics inversion using a dynamic Gaussian mixture model, Geophysical Journal International, 224, 40–68.

Capriotti J., L.J. Heagy, and D. Fournier, 2021, Dask parallelized geophysical inversions using SimPEG. In ParCFD21.

Capriotti, J., J. Kuttai, D. Fournier, and L.J. Heagy, 2022, Linking open-source tools for geophysical simulation and inversion in rugged topographies. In Fall Meeting 2022. AGU.

Cockett, R., S. Kang, L. J. Heagy, A. Pidlisecky, and D. W. Oldenburg, 2015, SimPEG: An open-source framework for simulation and gradient based parameter estimation in geophysical applications: Computers and Geosciences, 85, 142–154.

Dask Development Team (2016). Dask: Library for dynamic task scheduling https://dask.org

Fournier, D., and D. W. Oldenburg, 2019, Inversion using spatially variable mixed lp-norms: Geophysical Journal International, 218, 268–282.

Haber E. and C Schwarzbach, 2014, Parallel inversion of large-scale airborne time-domain electromagnetic data with multiple OcTree meshes, Inverse Problems 30 055011.

Heagy L. J., T. Astic, J. Capriotti, J. Weis, and D. W. Oldenburg, 2022, Geophysical Inversions to Delineate Rocks with CO2 Sequestration Potential Through Carbon Mineralization, FastTIMES, 26,4.

Kang, S., Knight, R., 2022. Time-lapse inversion of airborne electromagnetic data for monitoring saltwater intrusion in the Salinas Valley of California, USA, in: Second International Meeting for Applied Geoscience & Energy, SEG Technical Program Expanded Abstracts. Society of Exploration Geophysicists and American Association of Petroleum Geologists, pp. 3125–3127.

Wei X. and Jiajia Sun, 2022, 3D probabilistic geology differentiation based on airborne geophysics, mixed Lp norm joint inversion, and physical property measurements, GEOPHYSICS 87: K19-K33.

3D Time Domain Inversion of Ground Electromagnetic Data with Open-Source SimPEG; A Case Study for SimPEG Applications to VMS Exploration in the Iberian Pyrite Belt

Scott R. Napier, Mira Geoscience*
Dominique Fournier, Mira Geoscience
Filipa Luz, Almina - Minas do Alentejo, S..A.
Kris Davis, Mira Geoscience

Summary

SimPEG (Simulation and Parameter Estimation in Geophysics) is an open-source python package for geophysical forward modelling and inversion. We demonstrate the utility of SimPEG to improve 3D EM inversion models and advance exploration outcomes using ground electromagnetic (EM) data, collected on the Portuguese side of the Iberian Pyrite Belt. The EM dataset was collected in a mineral concession in close proximity to the giant VMS deposit complexes at Aljustrel and Neves Corvo. The processing and inversion of EM data remains practically difficult due to variable data formats, unit conventions and numerous system parameters required to accurately represent a geophysical survey. A data processing and inversion workflow, implemented in Geoscience ANALYST software, is outlined, that documents the steps required to achieve efficient and effective inversion modelling and interpretation of this large ground EM dataset. Throughout, the inversion results are compared to a variety of approaches used on this data including, decay analysis, 1D inversion, plate models and established 3D EM inversion programs (UBC-GIF's H3Dtdinv). The outcome of the 3D modelling has been interpreted to be a very interesting localized conductivity bright spot, in a favourable structucual position, at the end of an interpreated thrust ramp. This result is a compelling exploratin target made possible becasue of the 3D inversion.

Introduction and background

The VMS metallogenic district of the Iberian Pyrite Belt (IPB) has been subject of renewed exploration campaigns. The list of discoveries highlight that improvements and model refinement along with advances in geophysical methods and 3D modelling were critical for the recent discoveries either in Spain or Portugal (La Magdalena and Sesmarias, respectively).

This study focusses on a greenfield project in the IPB that is located near Aljustrel (Cu-Zn active mine in Portugal) The area has been the focus of some studies by several companies during the last years. Within this exploration license, new methodologies recently developed for IPB have been tested to drive the exploration campaign including 3D EM inversion.

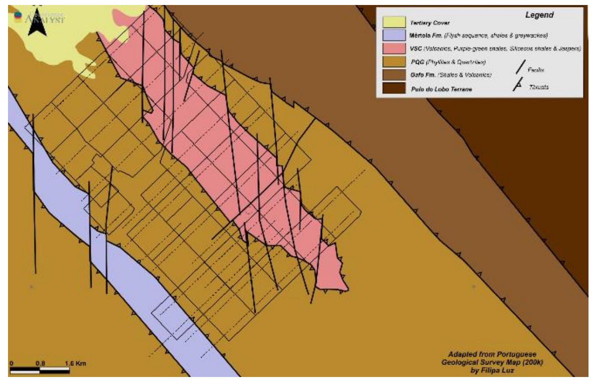

Figure 1: Location map showing deep search ground EM loops and lines. The loop are 1km square. The survey has 100m station spacing.

The studied area is located along the northern sector of the Portuguese IPB where it is possible to observe the two main lithostratigraphic units of this province: Phyllite Quartzite Group (PQG) and Volcano Sedimentary Complex (VSC). The PQG is the lowermost succession and includes black metapelites, metasiltstones and quartzites. Throughout the geological sequence there is frequently the presence of disseminated pyrite, especially in the siliciclastic units. The VSC is composed by felsic volcanic rocks that evolve laterally and vertically to metasedimentary sequence In this area the PQG overthrust the VSC, that were lately affected by deformation and led to a complex anticline structure with SW-verging. Lately, North-South structures cut all the anticline.

A ground EM survey was completed over the entire anticline using 1km square loops arranged contiguously, with 100m station spacing and variable 600m or 300m spaced lines. The survey was designed to detect very large EM conductors associated with the giant VMS deposits of the IPB with a demonstrated depth penetration, in favourable settings, of more than 1 km. The survey was conducted at 5 Hz base frequency and used a SQUID magnetic field sensor. The survey detected a number of very extensive northeast dipping conductors that are present throughout the survey area.

Many IPB deposits are closely associated with extensive black shales (Saez et al 1999). IPB VMS deposits often occur in the same basins which accumulated these shales at the end of Devonian time. Notable examples of black shale associations with IPB deposits include Neves Corvo, Tharsis, Aznalcollar, and Sotiel. As a result of past work in the belt the authors have found that IPB VMS deposits may present in EM data as localized increases in conductivity within a much broader horizon that represents the black shale unit of the same or similar age, within the VSC package of rocks.

Data processing and SIMPEG interface to Geoscience ANALYST

One of the critical problems with practical 3D EM inversion is that the handling of EM data remains difficult and time consuming due to variable data formats, unit conventions and numerous system parameters required to accurately represent an EM geophysical survey. This, along with the computational complexity of the inversion task have hindered widespread adoption of the 3D EM inversion technique and limited the practice to a relatively small number of domain experts.

EM data are more complex to deal with, and are less standardized, when compared to other sorts of geophysical data encountered by the mining geophysics professional. 3D inversion programs invariably require significant reformatting of the data prior to submission to inversion. Geoscience ANALYST Pro Geophysics provides a platform that facilitates the easy handling of electromagnetic data and preparation of data for 3D inversion. The software facilitates the following steps that are essential to 3D EM inversion:

1. Importer for Amira format TEM data
2. Conversion of data units
3. Definition of channel delay times and channel selection
4. Definition of transmitter current waveforms
5. Construction of octree model meshes.
6. Inversion settings dialogue box
7. Submission of inversion to the Azure cloud for fast remote computation
8. Inversion progress monitoring
9. Import and review of results including viewing models and data fit as decays and profiles

SIMPEG and 3D TEM inversion

SimPEG (Simulation and Parameter Estimation in Geophysics) is an open-source Python package for geophysical forward modelling and inversion (Cockett et. al 2015). The library provides the differential operators and methods needed to compute electromagnetic fields for various types of geophysical experiments: direct-current, inductive loops, natural sources (Heagy et al. 2017). The customizable framework also provides modular components for deterministic inversion, following the conventional weighted least-squares approach (Li & Oldenburg, 1996).

As for any numerical simulation, the Earth must be approximated by discrete elements that characterize the subsurface in terms of physical property. SimPEG provides several types of meshes to parameterize the physics: horizontal layers, cuboids, cylinders and tetrahedra. For this project, we employed a semi-structured Octree grid. Octree meshes can be refined locally to provide a good level of numerical accuracy while keeping the overall problem size small. Runtime and memory requirements were further reduced by employing a mesh-decoupling approach such that individual loop sources are simulated on localized mesh (Yang et al. 2014).

We used the Intel-Pardiso direct solver for the forward simulation and computation of derivates with respect to the model, or sensitivities. We opted to explicitly store the sensitivity matrix of each sub-problems rather than implicitly calculating gradients with matrix operations. Having access to the Jacobian allowed us to speed up the inversion process by employing a Jacobi pre-conditioner and by reducing the number calls to the direct solver. We also applied sensitivity-based weighting to the regularization function to better counteract ringing and near surface artefacts generally encountered in EM inversion (Yang et al. 2018).

Analysis of results

The ground EM survey grid over the anticline showed ubiquitous EM responses which were judged to be significant, but interpretation of the data was a challenge because of the widespread nature of the EM responses observed throughout. It was clear that the bulk of the responses were some sort of stratigraphic conductor or, rather set of conductors, but the question remained if there were more prospective areas within these zones.

The EM data were analysed and modelled in various ways with Maxwell plate models and 1D inversion prior to 3D inversion. The decay constant analysis indicated prospective responses with time constants, Tau values, that exceeded some of those recorded over known mineralization. Plate modelling was hampered by the relatively high background response and both plate modelling approaches and 1D inversion produced results that showed, generally, two subparallel, very extensive and shallow NE dipping conductive layers. While the EM responses were interesting these modelling approaches were unable to discriminate any conductive 'bright spots' within these horizons. In this setting these approaches were judged unsatisfactory and 3D inversion was suggested as an appropriate technique to aid the interpretation of these data.

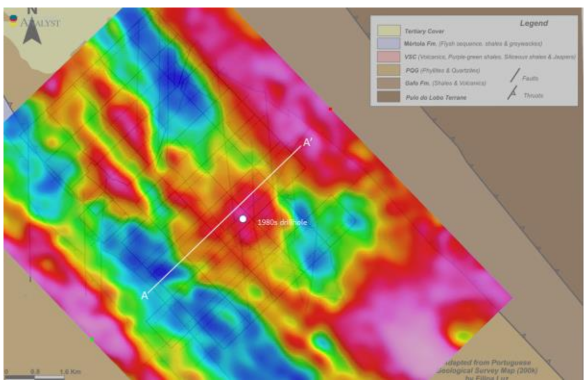

Figure 1: Map showing a colour grid of residual ground gravity data, TEM lines and loops. The location of a drillhole from the 1980s is shown on the map with a white circle. The location of the section and profile A-A' in Figure 3 is shown with the white line. The amplitude of the central anomaly along the profile is approximately 0.75 mgal.

The data were processed for 3D inversion in Geoscience Analyst Pro Geophysics and submitted to 3D inversion for both SimPEG and with the UBC-GIF program h3dtdinv. The existing 3D EM inversion program h3dtdinv was used to compare and contrast the results of the newer SimPEG 3D TEM inversion.

A comparison between 1D inversion and the two methods of 3D inversion is shown along the profile A-A' outlined in the residual gravity map in Figure 2. The gravity data is shown in profile in Figure 3 (top).

In Figure 3a the stitched 1D inversion shows a relatively simple configuration of two shallow dipping horizons. The h3dtdinv and SimPEG inversions, incorporating both Z and X component data, are shown in Figure 3b and 3c respectively. The 3D inversion adds some interesting complexity to the situation. Both 3D inversions use the 1D model as a starting model in orderto improve the modelling results. We find preconditioning the 3D inversion with the 1D model to be very useful in this case.

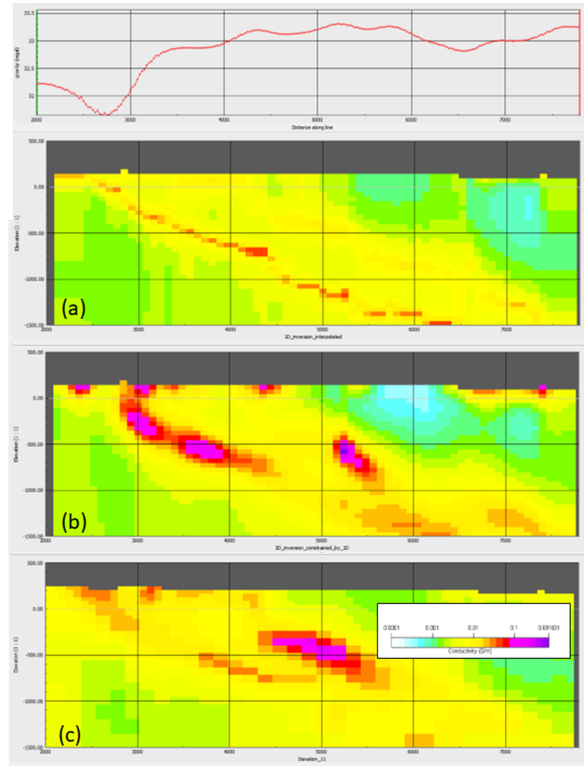

Figure 2. Top showing gravity data profile on A-A'. a) Section from stitched 1D inversion b) H3Dtd inversion model c) SIMPEG 3D TEM inversion model. Both 3D inversion models use the 1D inversion as a starting model.

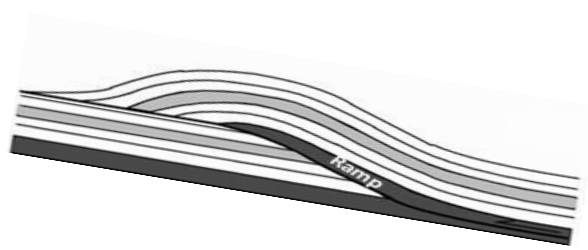

Figure 3: Thrust fault schematic modified from Dubey (2014) and rotated through 30 degrees The configuration of the schematic is noted to have similarities to the recovered 3D models.

The inadvertent targeting of stratigraphic conductors such as black shales have commonly been considered a pitfall in IPB VMS exploration when using EM methods. With new tools, such as 3D inversion, and with careful thought about the significance of these stratigraphic conductors, it may be possible to obtain structural insight to assist with targeting. This can be done by matching the 3D inversion geometries with known elements of the genetic and post-mineral deformational model for these deposits.

We believe that both 3D inversions have allowed for the imaging of a thrust fault ramp and the conductive horizons are interpreted as a thrust repetition of a moderately conductive black shale horizon. The situation is interpreted to be that shown schematically in Figure 4.

Furthermore, the conductivity bright spot, sitting at end of the interpreted thrust ramp is in a particularly interesting location. The initial break in thrust faulting, defining the ramp edge, may be controlled by pre-existing normal faults. These syn-mineral normal faults control mineralizing fluid flow and are bounding faults for the location of the basins in which VMS deposits form (Seaz at al. 1999). These faults may remain as zones of long-lasting crustal weakness and can be reactivated as thrust faults in late compression. In the IPB it is common to find deposits on present day anticlines, likely due to the reactivation of these pre-existing faults. Examples of significant deposits on anticlines include Neves Corvo, Massa Valverde, Rio Tinto and others.

As shown in the image in Figure 2 and in profile at the top of Figure 3, the area is associated with a very broad gravity high that could represent a deep, dense body though detailed gravity modelling has not yet been done here to confirm this.

Finally, a drillhole from the late 1980's is reported just south of the section in Figure 3. The location of the drillhole is indicated in Figure 2. In the summary report for the drillhole a BHEM offhole conductor at 630m depth is noted in the log, in a thick section of prospective VSC rocks. The depth of the offhole response matches the depth of the 3D EM conductor in the section. The historic BHEM EM survey was single component axial data, and the data themselves are lost, unfortunately. As a result no direction to the offhole source is available to confirm the 3D conductor, the location of which is centered northwest of the drillhole.

Conclusions

The use of Geoscience ANALYST allows the EM practitioner to make 3D EM inversion part of the day-to-day toolbox by offering data handling, inversion interface and access to cloud computational resources. We have demonstrated that efficient 3D inversion can be achieved using an open-source 3D inversion package SimPEG and we have benchmarked the 3D inversion with existing 3D EM inversion software to demonstrate consistency across the 3D methods in imaging.

In the case study presented here the 3D inversion has led to a new interpretation of an area of existing EM survey coverage where no particular target could be pinpointed based on traditional plate modelling or 1D EM interpretations alone.

In this case, a high conductivity bright spot was identified in the EM inversion that was interpreted as the front of thrust faut ramp, a position that is particularly prospective for VMS mineralization and presents a compelling exploration target for future follow up.

Acknowledgments (Optional)

We would like to thank the SimPEG community for the ongoing code development and technical support.

References

Dubey, A.K. (2014). Thrust Fault. In: Understanding an Orogenic Belt. Springer Geology. Springer, Cham. https://doi.org/10.1007/978-3-319-05588-6_4

Lindsey J. Heagy, Rowan Cockett, Seogi Kang, Gudni K. Rosenkjaer, Douglas W. Oldenburg. "A framework for simulation and inversion in electromagnetics" Computers & Geosciences, September 2017. doi:10.1016/j.cageo.2017.06.018

Cockett, Rowan, Seogi Kang, Lindsey J. Heagy, Adam Pidlisecky, and Douglas W. Oldenburg. "SimPEG: An Open Source Framework for Simulation and Gradient Based Parameter Estimation in Geophysical Applications" Computers & Geosciences, September 2015. doi:10.1016/j.cageo.2015.09.015.

Dikun Yang, Dominique Fournier, Seogi Kang, and Douglas Oldenburg. Recovery of compact conductors in 3D voxel inversion of time-domain EM data. SEG Technical Program Expanded Abstracts 2018. doi:/10.1190/segam2018-2984314.1

Dikun Yang, Douglas W. Oldenburg, Eldad Haber, 3-D inversion of airborne electromagnetic data parallelized and accelerated by local mesh and adaptive soundings, Geophysical Journal International, Volume 196, Issue 3, March 2014, Pages 1492–1507, https://doi.org/10.1093/gji/ggt465

R. Saez, E. Pascual, M Toscano, G R Almodovar " The Iberian Type of Volcano-Sedimentary Massive sulphide deposit" Minerlaium Deposita (1999) 34 : 549-570

Reference: Díez-Montes, A., Matos, J.X., Dias, R., Clavijo, E.G., Carmona, J.J.H., Albardeiro, L., Oliveira, J.T., Morais, I., Fernandes, P., Inverno, C., Machado, S., Ressurreição, R., Pereira, Z., Mendes, M., Solá, R., Salgueiro, R., Matilla, A.S., Gonçalves, P., Santos, S., López, M.T.L., 2020. Mapa Geológico de la Zona Surportuguesa/Carta Geológica da Zona Sul Portuguesa, Folha Transfronteiriça nº 1, Escala 1/200 000. Proj. Geo-FPI/Interreg POCTEP, Instituto Geológico y Minero de España/LNEG/Junta de Andalucía-SGIEM/CM Aljustrel. Formato A0, bilingue português-castelhano. ISBN: 978-989-675-067-1, NIPO: 836200054.

FTMG from a consultant's perspective

Sean E. Walker, Campbell & Walker Geophysics Ltd. (Scotland), Christopher (Kit) Campbell, Campbell & Walker Consultants Ltd. (Canada)*

Summary

Papers discussing the potential advantages of full tensor magnetic gradiometer (FTMG) data over conventional scalar total field magnetics are not new. However, they have primarily come from researchers, hardware developers, and companies with exclusive access to FTMG technology. While airborne FTMG surveys became commercially available in 2020, there are still very few case histories from an "end user" perspective. This paper will present our experiences working with FTMG data on various exploration projects. This will include a discussion of the practical advantages of measuring the full magnetic tensor, an overview of the available processing, modelling and inversion tools, and a field example from a recent survey. Throughout the presentation, we will highlight how we believe FTMG data can be used to advance an exploration project.

Introduction

Two excellent summaries describing the development and subsequent commercialization of airborne FTMG technology have been published in recent years (Stolz et. al., 2021, Rudd et. al., 2022). Therefore, we will begin our discussion of airborne FTMG data with the understanding that this type of data exists, is being collected regularly and is available to the wider exploration community. We feel that this is worth noting because for many "non-experts" the pre-2020 lack of access to airborne FTMG data relegated the numerous papers published and talks given about its advantages to the category of an interesting development rather than a new tool in the exploration toolbox. The first two sentences of the abstract of Pedersen and Rasmusen (1990) sum this up well; "The full gradient tensor is presently not measured routinely onboard airplanes or on land. This paper describes some improvements that can be made in strategies of data collection and in processing of potential field maps if such tensor measurements were available." Luckily, for the greater community, a group of dedicated "experts" worked to advance data processing (FitzGerald and Holstein, 2006, Fitzgerald, et. al., 2011, Schiffler, et. al. 2017), theory (Schmidt and Clark, 2006, Beiki, et. al., 2012, Clark, 2012), modelling (Foss, 2006, Fitzgerlad, et. al., 2011, Pratt, et. al., 2019), and inversion (Zhdanov, et. al., 2011, Zhdanov, et. al. 2012, Cockett, et. al. 2015, Fournier, 2019). Others with access to field data sets presented case histories (Rompel, 2009, Vorster, et. al. 2013). The diligent work of these individuals has provided a solid foundation for consultants (and others) who are now tasked with interpreting and modelling this "new" type of data.

FTMG advantages in practice

The majority of discussions about airborne FTMG data begin with a list of its advantages over conventional TMI data. One example from Letts et. al. (2019) includes the following points; 1) lower noise, 2) higher spatial resolution, 3) insensitivity to diurnal variations and 4) increased information about the magnetic field. While the first three points in this list are technically impressive in their own right, it is the fourth point that makes FTMG data unique. Other lists elaborate upon this point to include better-constrained geophysical inversions which can improve geological interpretation and directly detect remnance (Jansen, 2020) as well as a better definition of structural features, continuous mapping of the magnetization direction of magnetic source rocks, and more precise mapping of geologic boundaries (Rudd et. al., 2022). A less commonly mentioned but equally important consequence is the system's effectiveness in low magnetic latitude environments (Rudd et. al., 2022). However, in the end, it is the increased information contained in the tensor measurements that make all these things possible. So we will start there.

If the anomalous magnetic field vector $\boldsymbol{b}$ is defined as

$$\boldsymbol{b} = [b_x, b_y, b_z] = b_x\hat{\boldsymbol{x}} + b_y\hat{\boldsymbol{y}} + b_z\hat{\boldsymbol{z}}$$

and the inducing field is defined by another magnetic field vector, $\boldsymbol{f}$, the anomalous total magnetic intensity (TMI) can be approximated as

$$TMI = |\boldsymbol{f} + \boldsymbol{b}| - |\boldsymbol{f}| \approx \boldsymbol{b} \cdot \hat{\boldsymbol{f}} \text{ if } |\boldsymbol{f}| \gg |\boldsymbol{b}|.$$

The magnetic gradient tensor $\boldsymbol{B}$ is defined as

$$\boldsymbol{B} = \begin{bmatrix} B_{xx} & B_{yx} & B_{zx} \\ B_{xy} & B_{yy} & B_{zy} \\ B_{xz} & B_{yz} & B_{zz} \end{bmatrix}, B_{ik} = \frac{\partial b_i}{\partial k} \; (i, k \in x, y, z)$$

and if we assume quasistationary conditions and neglect telluric currents the tensor can be defined by five independent tensor components

$$\boldsymbol{B} = \begin{bmatrix} B_{xx} & B_{xy} & B_{xz} \\ B_{xy} & B_{yy} & B_{zy} \\ B_{xz} & B_{yz} & -(B_{xx} + B_{yy}) \end{bmatrix}.$$

To highlight the increased information about the magnetic field that is captured by measuring the tensor components two sets of synthetic data were generated. For both cases, the magnetic field from a sphere located at depth of 200 m, a radius of 100 m and magnetic susceptibility of 0.1 SI was calculated on a plane 50 m above the surface at 10 m intervals in both x and y directions. Figure 1 shows the response of the sphere at the magnetic pole (inclination: 90˚, declination: 0˚) and Figure 2 shows the response of the sphere near the magnetic equator (inclination: 15˚, declination: -15˚). While in reality, the field at the equator has a smaller amplitude to make a direct comparison of responses both simulations used a value of 60,000 nT. The left column of images in each panel contains the magnetic field components (b_x, b_y, and b_z) and the top right image shows the TMI. The changes that take place in the TMI response of a dipole from the magnetic pole to near the magnetic equator are well understood. Simply looking at the data plots it appears intuitive that having five independent measurements of changes in field components is better than a projection of the field in a single direction.

Processing, modelling and inversion

The analytical signal amplitude (ASA) is a simple method of overcoming the complexities of responses at low magnetic latitudes (Rajagopalan, 2003) and is defined as

$$ASA = \sqrt{\left(\partial TMI/\partial x\right)^2 + \left(\partial TMI/\partial y\right)^2 + \left(\partial TMI/\partial z\right)^2}.$$

However, the sphere example shown here highlights some limitations. The ASA calculated at the pole has a maximum amplitude that is approximately double that of the ASA at the equator (Figure 2) and the shape of the ASA response near the equator is distorted relative to the shape at the pole. It is possible to calculate a tensor-based version of the analytical signal using Bx, By or Bz (Schmidt and Clark, 2006). The Bz_ASA shown in Figures 1 and 2 is defined as

$$Bz\ ASA = \sqrt{(B_{xz})^2 + \left(B_{yz}\right)^2 + (B_{zz})^2}\ .$$

In Figure 2 we see that even when we use three measured tensor components to calculate the Bz_ASA, it suffers from variations similar to the TMI-derived ASA. This is where the normalized source strength (NSS, Beiki, et. al., 2012, Clark, 2012) shows its usefulness in combining the detail contained in the individual tensor components into a single value. The NSS is a rotational invariant that is calculated from the eigenvalues of $\boldsymbol{B}$ labelled in non-increasing order ($\lambda_1 \geq \lambda_2 \geq \lambda_3$) as

$$\mu = \sqrt{-\lambda_2^2 - \lambda_1\lambda_3}.$$

The NSS is independent of the magnetization direction and for a dipole source, the peak amplitude is proportional to the dipole moment (Clark, 2012). The results in Figures 1 and 2 confirm that the NSS is identical for the measurements at the pole and near the equator. While the exact relationship does not extend to arbitrarily shaped magnetic bodies the NSS is still a very useful quantity for identifying anomalies within FTMG data (Pratt et. al. 2019). After identification via the NSS the individual tensor components within each anomaly can be reviewed to identify the presence remnant magnetization. A first pass of this can be done qualitatively by comparing patterns in the tensor components with those expected for an induced field anomaly within the survey area. Pratt et. al. (2019) present an automated procedure to achieve the same goal. These anomalies can also be modelled using iterative forward calculations or parametric inversion (Pratt et. al., 2020) or inverted to recover a susceptibility or magnetization vector voxel model (Cockett et. al. 2015, Fournier, 2019). Before modelling FTMG data it is important to know the coordinate system convention used to define the data by the contractor and by the modelling software (Holstein et. al., 2015).

Field example

The Eskay Creek deposit is a high-grade, precious metals-rich epithermal volcanogenic massive sulphide (VMS) deposit located 83 km northwest of Stewart, British Columbia, Canada. Murray et. al. (2022) provide an overview of the exploration and development carried out by Skeena Resources Ltd. at Eskay Creek. In 2020, Skeena contracted Dias Airborne to fly an FTMG survey over their claims at Eskay Creek. The goal of the survey was to enhance the lithological and structural information around the deposit.

A 1.5 x 1.5 km subset in the northeast of the survey area, referred to as Eskay Deeps, was identified by Skeena for inversion. The FTMG data in Figure 3 shows three isolated low-amplitude anomalies. The areal extent relative intensity of each anomalous zone is well-defined by the normalized source strength. TMI data from an Aerodat survey flown in 1988 suggests the presence of an anomaly in this area, however, due to the quality of the data, it is just on the edge of detection.

The five independent components of the FTMG tensor were inverted using SimPEG (Cockett et. al., 2105, Fournier, 2019) on an Octree mesh with a core consisting of 25 x 25 x 12.5 m voxels. The data was pre-processed according to the guidelines described in Walker (2018) and were inverted multiple times to determine reasonable error estimates and to ensure that the recovered model was not overfitting the data. The final magnetization amplitude model shown in Figure 4 provides an estimate of the location and depth of the magnetic sources in the Eskay Deeps area. The information from the inversion was combined with the existing litho-structural model in the Eskay Deeps area to assist in planning a deep exploration drill hole in late 2022. The hole intersected a broad zone of Rhyolite-hosted mineralization at a vertical depth of 850 metres below the surface with grades of 3.79 g/t Au, 59.4 g/t Ag (4.46 g/t AuEq) over 32.19 metres (Skeena Resources Ltd., 2022).

Conclusions

More than twenty years of research have shown the many things that can be done with FTMG data. In this paper, we have focused on how to get the most out of the data now that it is more widely available. Our proposed workflow describes steps for processing, interpreting and modelling/inverting selected anomalous zones within a dataset. The results of this methodology were combined with a litho-structural model for drill targeting on an active exploration project.

Acknowledgements

The authors would like to thank Paul Geddes, Senior Vice President, Exploration & Resource Development, Skeena Resources Ltd. for providing the information about the deep drilling at Skeena deeps and for permission to present the FTMG data and inversion results.

References

Beiki, M., Clark, D. A., Austin, J. R., and Foss, C. A., 2012, Estimating source location using normalized magnetic source strength calculated from magnetic gradient tensor data, Geophysics, 77, 6, J23–J37.

Cockett, R., Kang, S., Heagy, L.J., Pidlisecky, A. and Oldenburg, D.W., 2015. SimPEG: An open source framework for simulation and gradient based parameter estimation in geophysical applications, Computers and Geosciences, 85, 142–154.

Clark, D. A., 2012, New methods for interpretation of magnetic vector and gradient tensor data I: Eigenvector analysis and the normalised source strength, Exploration Geophysics, 43, no. 4, 267–282.

Fitzgerald, D., and Holstein, H., 2006. Innovative data processing methods for gradient airborne geophysical data sets, The Leading Edge, 25, 1, 87–94.

Fitzgerald, D., Holstein, H., and Foss, C., 2011. Automatic modelling and inversion for dykes from magnetic tensor gradient profiles - recent progress, SEG Technical Program Expanded Abstracts, 796-800.

Foss, C.A., 2006. Improvements in source resolution that can be expected from inversion of magnetic field tensor data, Leading Edge, 25, 81–84.

Fournier, D., 2019, Advanced potential field data inversion with lp-norm regularization: Ph.D. thesis, The University of British Columbia.

Holstein, H., Fitzgerald, D., Zengerer, M., and Starr, A., 2015. Left or right handed potential data?, First Break, 33, 4.

Jansen, J., 2020. Full-Tensor Magnetic Gradiometry: a better way to collect airborne data, PDAC Annual Convention.

Letts, S., Jansen, J., Polomé, L., and Vorster, A., 2019. Interpretation and Benefits of Full-Tensor Squid-Magnetometer Data, BC Geophysical Society Monthly Meeting.

Murray et al., 2022, Eskay Creek Project NI 43-101 Technical Report and Feasibility Study: Prepared for Skeena Resources Ltd. by Ausenco Engineering Canada Inc., pp. 472. Retrieved from https://skeenaresources.com/site/assets/files/6532/eskay_creek_ni_43-101_technical_report_and_fs_amended_sept_19_2022.pdf

Pedersen, L.B., and Rasmussen, T.M., 1990. The gradient tensor of potential field anomalies: Some implications on data collection and data processing of maps, Geophysics, 55, 12, 1558–1566.

Pratt, D.A., McKenzie, K.B. and White, A.S., 2019. An AI approach to automated magnetic formation mapping beneath cover, 2nd Australasian Exploration Geoscience Conference, ASEG, Extended Abstracts.

Pratt, D. A., White, A. S., Parfrey, K. L. and McKenzie, K. B., 2020. ModelVision User Guide Version 17.0, Tensor Research Pty Ltd.

Rajagopalan, S., 2003. Analytic Signal vs. Reduction to Pole: Solutions for Low Magnetic Latitudes, Exploration Geophysics, 34, 4, 257-262.

Rompel, A.K.K., 2009. Geological Applications for FTMG, 11th SAGA Biennial Technical Meeting and Exhibition.

Rudd, J., Chubak, G., Larnier, H., Stolz, R., Schiffler, M., Zakosarenko, V., Schneider, M., Schulz, M., and Meyer, M., 2022. Commercial operation of a SQUID-based airborne magnetic gradiometer, The Leading Edge, 41, 7, 486–492.

Schiffler, M., Queitsch, M., Stolz, R., Meyer, H.-G. and Kukowski, N., 2017. Application of Hilbert-like transforms for enhanced processing of full tensor magnetic gradient data, Geophysical Prospecting, 65, 68–81

Schmidt, P. W., and Clark, D.A., 2006, The magnetic gradient tensor: Its properties and uses in source characterization, The Leading Edge, 25, 1, 75–78.

Skeena Resources Ltd., 2022, Skeena extends Eskay Creek rift with new discovery intersecting 4.46 g/t AuEq over 32.19 metres [Press Release]. Retrieved from https://skeenaresources.com/news/skeena-extends-eskay-creek-rift-with-new-discovery-intersecting-4.46-g-t-aueq-over-32.19-metres/

Stolz, R., Schiffler, M., Zakosarenko, V., Larnier, H., Rudd, J., Chubak, G., Polomé, L., Pitts, B., Schneider, M., Schulz, M., Meyer, M., and Campbell, K., 2021. Status and future perspectives of airborne magnetic gradiometry, SEG Technical Program Expanded Abstracts, 3554-3561.

Vorster, A., Polomé, L. and Letts, S., 2013. Evaluation and interpretation of full tensor SQUID magnetic gradiometer data, 13th SAGA Biennial Conference & Exhibition.

Walker, S.E., 2018, Sometimes innovative tools require an FAQ: Lessons learned inverting magnetic data, SEG Technical Program Expanded Abstracts, 1868-1872.

Zhdanov, M.S., Cai, H., and Wilson, G.A., 2011. 3D inversion of full tensor magnetic gradiometry (FTMG) data, SEG Technical Program Expanded Abstracts: 791-795.

Zhdanov, M.S., Čuma, M., Wilson, G.A., and Polomé, L., 2012. 3D magnetization vector inversion for SQUID-based full tensor magnetic gradiometry, SEG Technical Program Expanded Abstracts : 1-5.

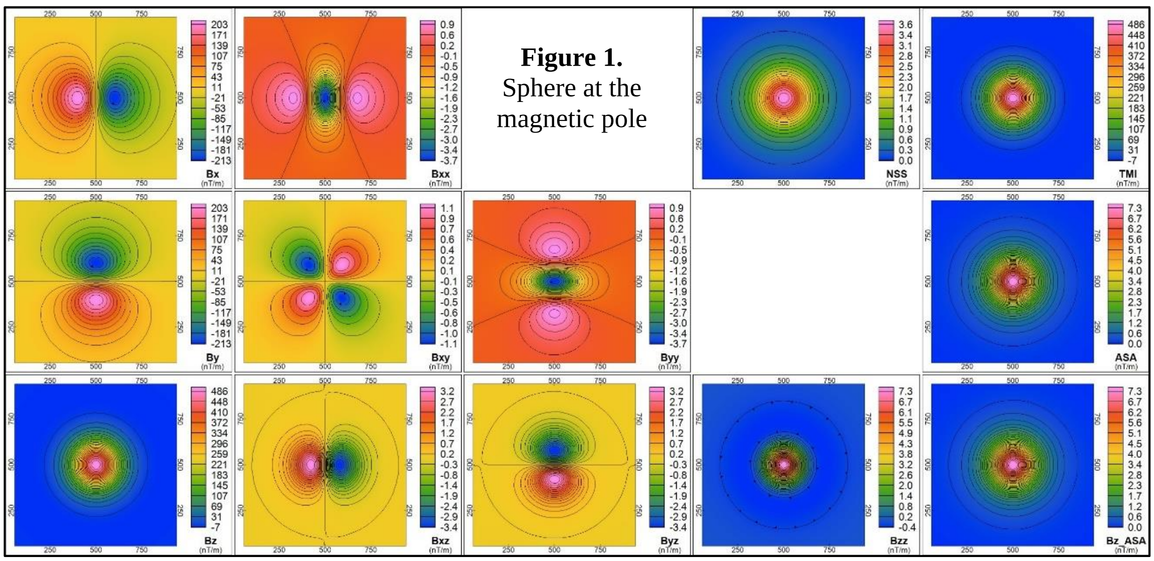

Figure 1. Sphere at the magnetic pole

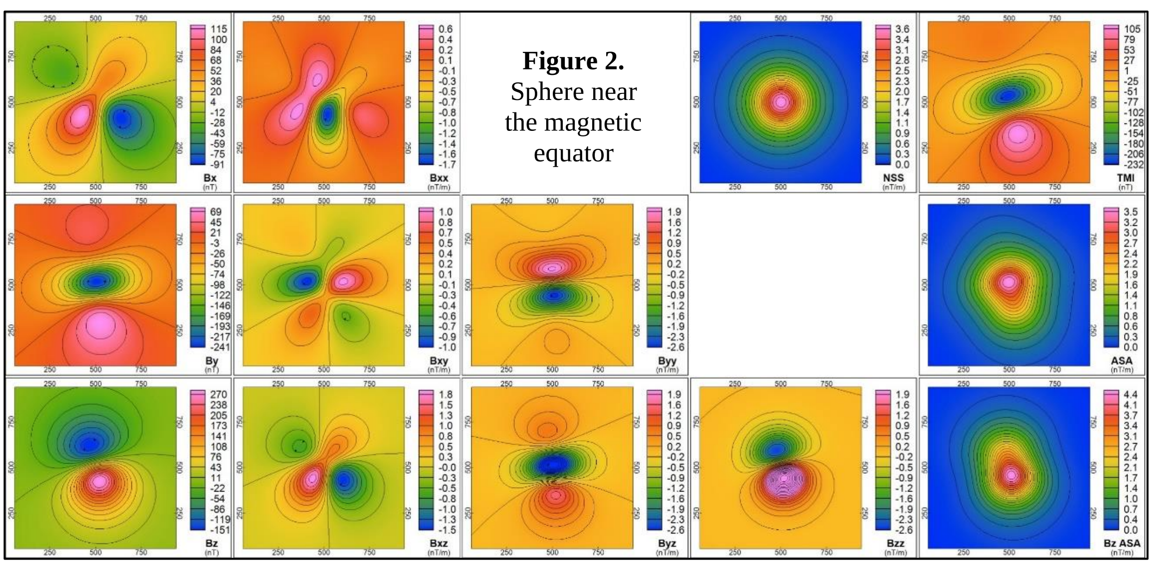

Figure 2. Sphere near the magnetic equator

Figures 1 and 2. Synthetic data from a sphere. Top panel (Fig 1): at the magnetic pole (Ampl: 60,000 nT, Incl:90, Decl:0). Bottom panel (Fig 2): near the magnetic equator (Ampl: 60,000 nT, Incl:15, Decl:-15). The sphere is located at (500, 500, -200) and has a susceptibility of 0.1 SI. Data is calculated at z=50 plane at 10 m intervals in X and Y. The subplots in each panel are: Top row (L-R): bx, Bxx, NSS (normalized source strength), TMI, middle row (L-R): by, Bxy, Byy, ASA (analytical signal amplitude calculated from TMI), bottom row (L-R): bz, Bxz, Byz, Bzz, Bz_ASA (analytical signal amplitude calculated from bz). ENU coordinate system.

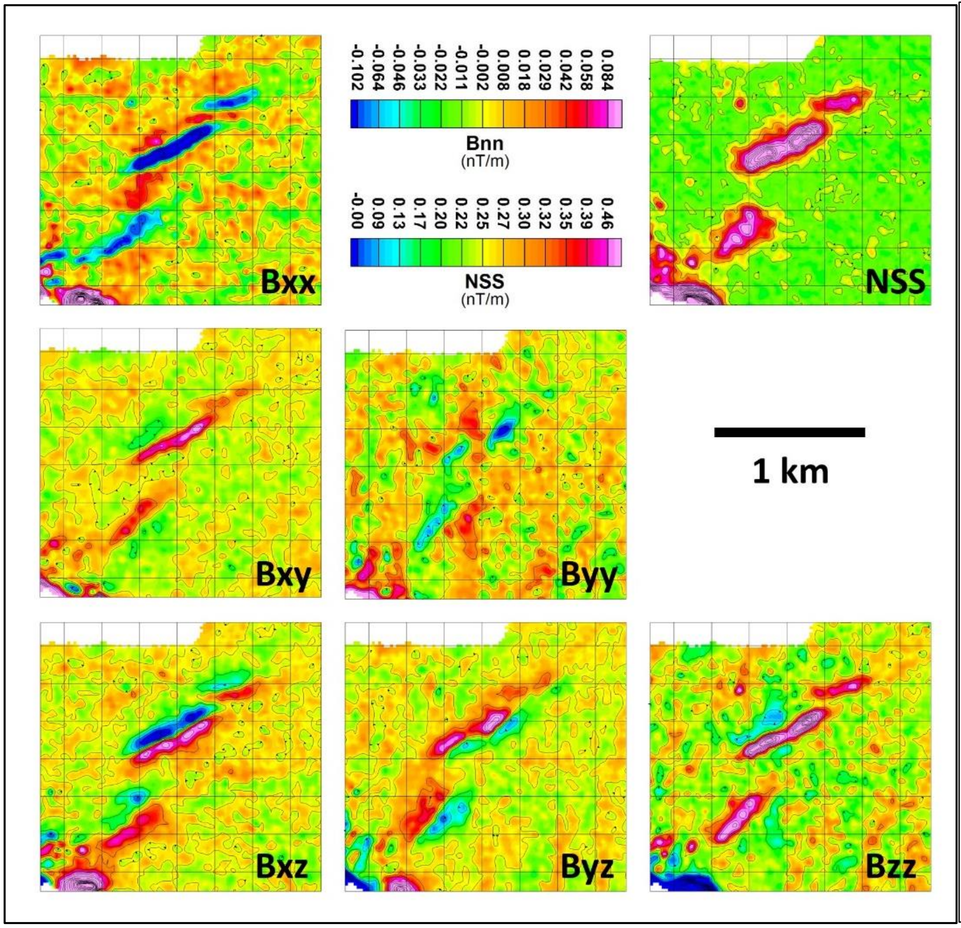

Figure 3. Subset of the FTMG survey data over the Eskay Deeps target area used in the magnetization vector inversion. The panels show the six tensor components (Bxx, Bxy, Byz, Byy, Byz, and Bzz) and the normalized source strength (NSS). NED coordinate system.

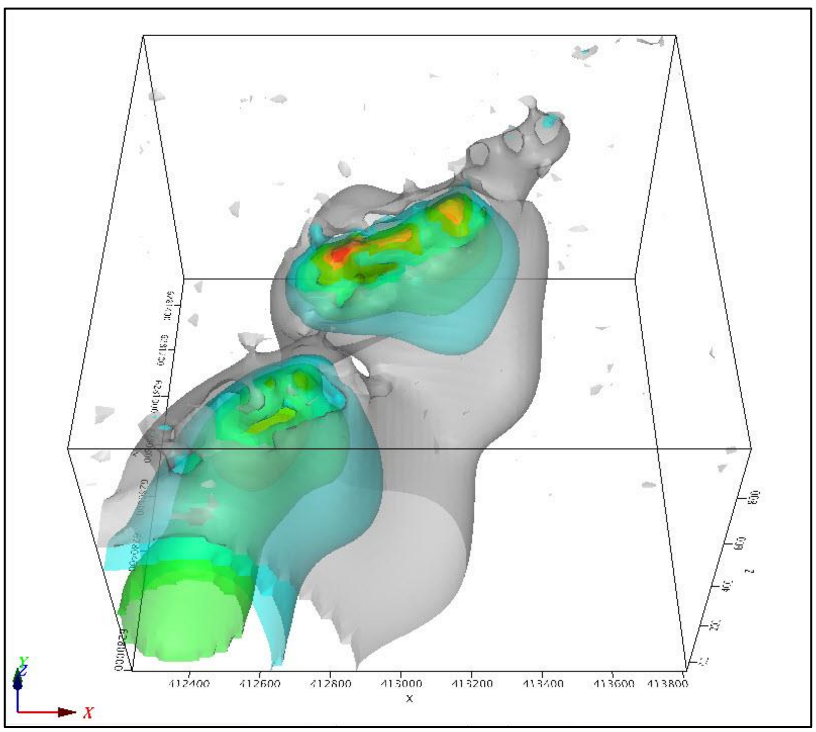

Figure 4. Iso-surfaces derived from the recovered magnetization amplitude model in the Eskay Deeps area. The iso-shells are defined using cool to warm colours for the values 7.5E-5, 1.25E-4, 1.75E-4, 2.25E-4, 2.75E-4 and 3.25E-4 of equivalent SI.

Targeting concealed orogenic gold mineralization using aeromagnetic data: A case study from the Red Lake camp, Superior Province, Ontario, Canada

Karl Kwan* and Jean M. Legault**, Geotech Ltd., Aurora, Ontario, Canada
* Corresponding author, ** Presenter

Abstract

The targeting of orogenic gold deposits under cover is challenging, requiring a holistic and multi-disciplinary mineral systems approach. Orogenic gold deposits are structurally controlled, and it is also considered as a Self-Organized Critical (SOC) ore system. One of the defining attributes of a SOC orogenic system is that the spatial distribution of gold deposits is fractal, and that the deposits are clustered at regional and district/camp scale. The critical state of a SOC orogenic gold system is the geological environment in which the gold was deposited. In this state, the gold deposits share similar structural settings and common physicochemical conditions. The high-resolution aeromagnetic surveys in the exploration for orogenic gold deposits is routinely deployed and the acquired aeromagnetic data are commonly used to map the structures. The Structural Complexity (SC), defined as the intersection density and the orientation diversity of linear structures, can also be derived from the magnetic data. Common features in the SC and in the magnetic data can be grouped together using unsupervised classification in order to construct a Self-Organizing Map (SOM). The predictive targeting of orogenic gold can be achieved with the support of a Supervised Deep Neural Network (SDNN), with the SC, the magnetic data, and the SOM result as inputs. The SDNN is trained using the data from a study area containing known gold deposits. The output target probabilities provide options for the selection of exploration targets. A set of targeting criteria, mainly based on geological considerations, are used to select the final targets. Since the orogenic gold targeting process involves the SC, SOM, and SDNN, it is therefore termed as the S^3 method. We test the S^3 method using the public domain high-resolution magnetic data set from the Red Lake camp, Superior Province, Ontario, Canada. Our results suggest that this method is effective and robust in targeting concealed orogenic gold mineralization in the greenstone belts worldwide.

Keywords/Acronyms: Mineral Exploration Targeting (MET), greenstone-hosted orogenic gold, Orientation Entropy(OE), Structural Complexity (SC), Self Organized Critical System (SOC), Self-Organizing Map (SOM), Supervised Deep Neural Network (SDNN).

1. Introduction

The Archean greenstone-hosted orogenic gold (Groves et al., 1998) deposits in the Superior Province, Canada, are structurally controlled epigenetic deposits characterized by simple to complex networks of gold-bearing laminated quartz-carbonate fault-fill veins (Dubé and Gosselin, 2007). In the greenstone belts, mafic to ultramafic volcanic rocks are the most magnetic, with the mean magnetic susceptibilities exceeding 0.015 SI (Mitchinson, 2009).

World-class orogenic gold deposits are zones of focused mass and energy flux (McCuaig & Hronsky, 2014) and are structurally controlled. In order to find those deposits, first we need to identify the structures that facilitate the efficient channeling the gold-bearing fluids. In orogenic gold exploration, the most important question is not where the gold came from, but instead, where it was concentrated in the upper crust to form economic deposits (Hronsky and Groves, 2008). Fault geometry related parameter, such as intersections of faults and intrusive contacts, is used in targeting of hydrothermal mineral deposits by Yousefi and Hronsky (2023).

Hronsky (2011) argued that most of the ore-forming systems, including orogenic gold systems, are examples of Self-Organized Critical (SOC) systems. For SOC orogenic gold systems, the critical point is the geological state in which the gold was deposited. Furthermore, the generation of extreme fluid-pressure gradients is critical for producing more focused and larger fluxes of gold-mineralizing fluid. Common physical and chemical conditions exist at camp scale for SOC gold deposits, and some of these commonalities could be recorded by aeromagnetic data. Therefore, the unsupervised classification method such as the Self-Organizing Map (SOM) can be used to classify the aeromagnetic data and identify those features or classes associated with the similarities of SOC gold deposits.

In this case study, a targeting method for concealed orogenic gold deposits is proposed and tested using aeromagnetic data from the Red Lake camp, Superior Province, Ontario, Canada.

2. Targeting Method

As briefly explained in the introduction, two of the fundamental geological processes of orogenic gold systems are SC (Structural Complexity) and SOC (Self-Organized Critical) systems. The SOC describes how orogenic gold systems are formed (Hronsky, 2011), whereas SC controls the spatial distribution of orogenic gold deposits (Groves et al., 2000).

The linear structures, such as ridges, in the aeromagnetic data can be mapped using the CET (Centre for Exploration Targeting, the University of Western Australia) grid analysis module, available by subscription from Seequent of the Oasis Montaj geophysical data processing platform. The CET SC sub-module offers the computation of SC directly using the ridge vectors derived from aeromagnetic data. The ridge vectors are stored in a database. The SC workflow, fully described in Holden et al. (2012), consists of these steps, (1) magnetic ridge detection, (2) amplitude thresholding and skeletonizations (3) skeleton to vector conversion, and (4) generating Contact Occurrence Density (COD) based on ridge intersection density, and the Orientation Entropy (OE) based on trendline direction/orientation. Importantly, some linear features cross-cutting the ridges or with magnetite degradation are not represented by the ridges. Therefore, these structures must be manually digitized and placed in the CET ridge vector database. The analysis of SOC orogenic gold systems using aeromagnetic data is carried out by the Geosoft Self-Organizing Map (SOM) tool, created by Ian MacLeod of Geosoft Inc. in 2014. Since 2017 the program is freely available at the following link:

https://github.com/GeosoftInc/gxpy/tree/master/examples/geosoft_research/self_organizing_maps

The release of Google's TensorFlow (TF) for Python (https://www.tensorflow.org/) in 2015 enables the application of the powerful and robust Deep Neural Network (DNN) system to geoscience data to predict exploration targets. A DNN is a simple feed-forward network with many hidden layers. For this study, the DNN class used is the "*Tensorflow.Estimator.DNNClassifier*" in TensorFlow version 2.3.

3. Targeting Application

The chosen area of study is the Red Lake Gold Camp in northwestern Ontario. The Red Lake camp has produced over 19 Moz gold since the 1930s (Harris, et al., 2007).

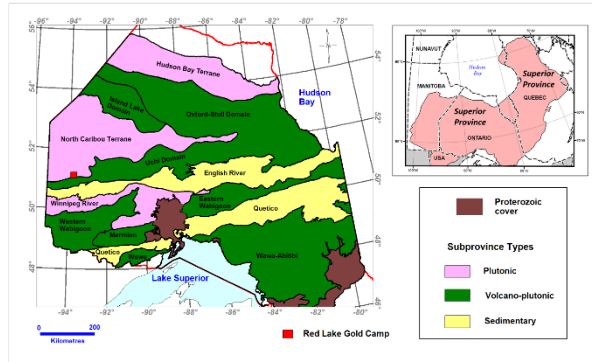

Figure 1: The Superior Province in Ontario with subprovinces classified into plutonic, volcano-plutonic, and sedimentary belts (modified after Stott, 2011 and Rehm et al., 2021). The Red Lake gold camp is indicated by a red rectangle.

Regional Geology

The Canadian Superior Province (Figure) represents the largest Archean craton in the world, forming the core of the North American continent (Percival, 2007). Orogenic gold deposits were formed along major structures developed in greenstone belts during regional deformation between 2710 and 2600 Ma (Robert et al., 2005). The Red Lake camp is located near the southern margin of the North Caribou Subprovince.

Local Geology

The local geology (Sanborn-Barrie et al., 2004) of the Red Lake camp, shown in Figure 2, consists of mainly the felsic to mafic volcanic rocks, metasedimentary rocks, and the mafic to ultramafic rocks, in the greenstone belt trending SW-NE north of the Red Lake airport, and then turned to the NW-SE direction east of the airport. The greenstone belt is surrounded by granitoids.

The Campbell-Red Lake complex in Balmertown had historical productions of 11.2 Moz and 5.6 Moz gold respectively, and the Cochenour-Willans mine produced 1.2 Moz gold between 1939 and 1971 (Goldcorp NI 43-101 technical report, 2016). The gold mineralization is structurally controlled, and most of the gold deposits are hosted in mafic volcanic rocks and occur as vein systems (Sanborn-Barrie et al., 2004). At the Campbell-Red Lake complex, one of the gold mineralization styles is the sulphide mineralization, typically found in broad zones of strongly sheared mafic rocks accompanied by disseminated pyrrhotite (up to 30%), *Goldcorp NI 43-101 technical report, 2015*.

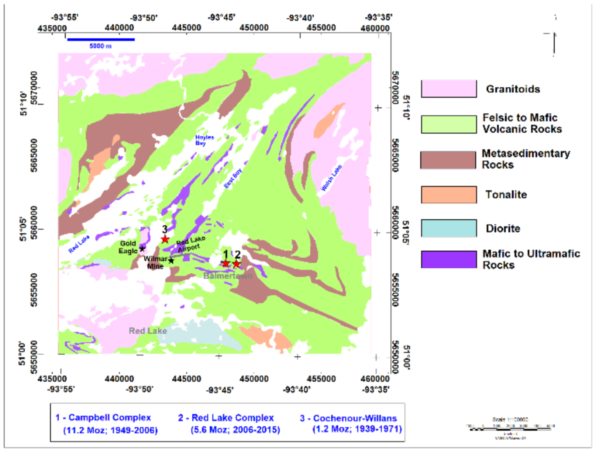

Figure 2 The local geology of the Red Lake camp.

Aeromagnetic Data

High-resolution airborne magnetic surveys covering the Archean greenstone belts in Ontario were initiated in 1975 by the Ontario Geological Survey (OGS, 2017). Seventy-six high-resolution airborne magnetic surveys were merged to create seven super-grids. The Red Lake-Stormy super grid includes the aeromagnetic data from the Red Lake camp, and the magnetic RTP (Reduced to Pole) data are shown in Figure 3. The strong magnetic responses are associated with volcanic rocks, and mafic to ultramafic rocks.

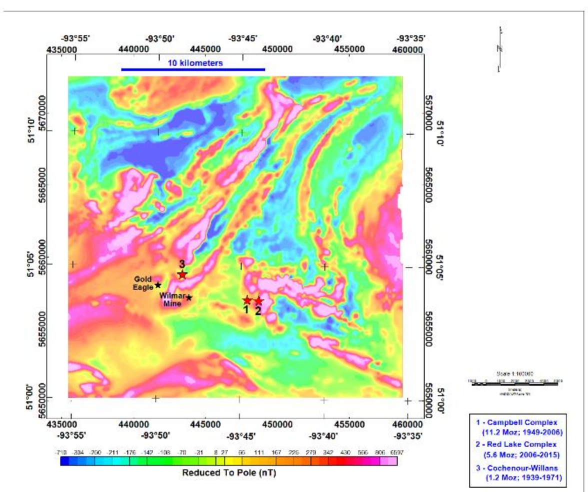

Figure 3: Magnetic RTP data of the Red Lake camp.

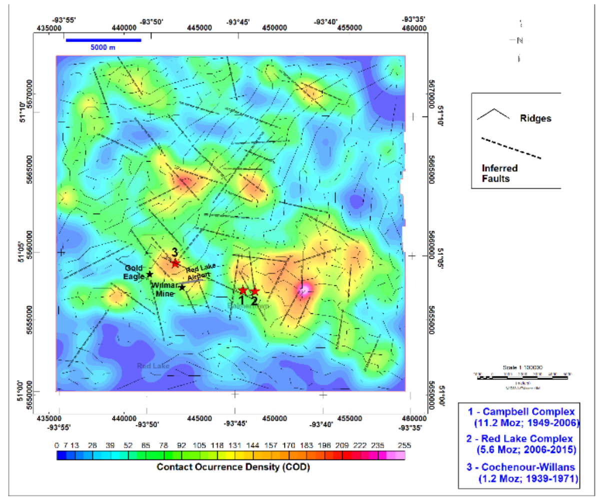

Figure 4: COD (Contact Occurrence Density) data, Red Lake camp.

SC and SOM results

The Contact Occurrence Density (COD) data, or the magnetic ridges intersection density, are presented in Figure 4. The COD is calculated using both the magnetic ridges mapped by the automatic process in the CET module and the inferred faults. High COD values are in the greenstone belt. It is worth noting that the major gold mines are located close to COD highs.

The OE map is shown in Figure 5. The major gold mines are also in the margins of OE high zones.

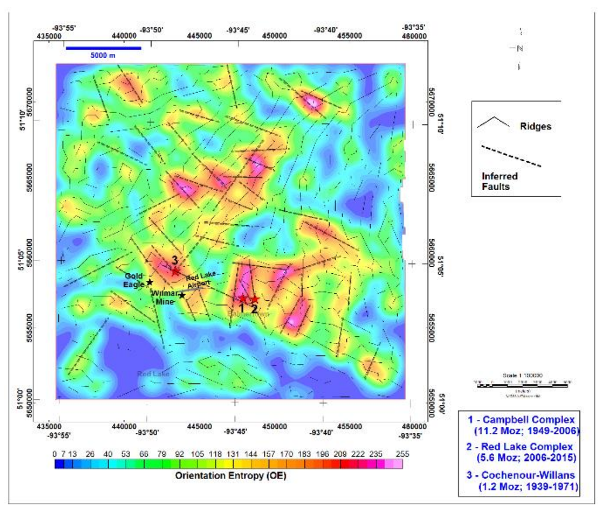

Figure 5: The OE (Orientation Entropy) map, Red Lake camp.

The SOM (self organizing map) results or classes, computed using the COD, OE, the analytic signal data as the inputs, are shown in Figure 6. The major gold mines are in the zones with higher anomalous classes (>13). The other high anomalous class zones, such as the one in the north-central region of the Red Lake greenstone belt, and the one SE of Campbell and Red

Lake mines, could be targeted for potential world class gold deposits.

SDNN Results and Selected Targets

The third module of the S^3 targeting tool for concealed orogenic gold is the predictive targeting analysis using Supervised Deep Neural Network (SDNN). The inputs to the SDNN include the SOM results, COD, OE, and the analytic signal data.

The SDNN is trained using the input data from an area including the Campbell-Red Lake mines as recommended targets (Figure 7a). The outputs from the SDNN are the predictive target probabilities. The top 61.3% (>0.75 region in the histogram) probabilities ((Figure 7b) are chosen for target selection. The purpose of SDNN is to identify potential exploration targets using the geophysical signatures of known gold deposits. In the case of greenfield exploration in less well-endowed regions, exploration targets must be selected with assistance of the project geologist who has mapped the area and is most familiar with the local geology.

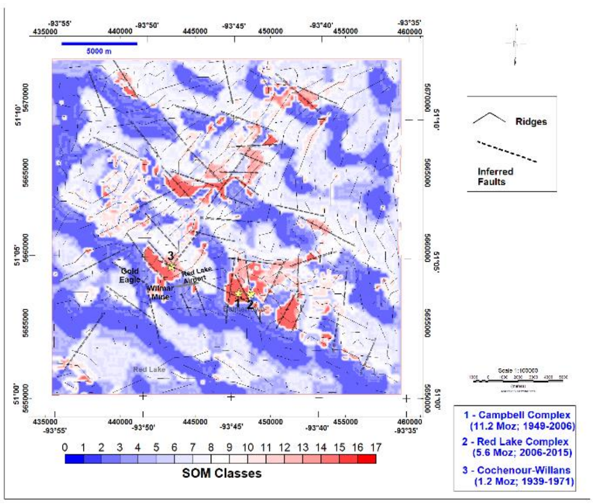

Figure 6: The higher anomalous SOM classes (>13) are represented by hot colours, and the gold mines in the Red Lake camp are in the zones with high anomalous classes.

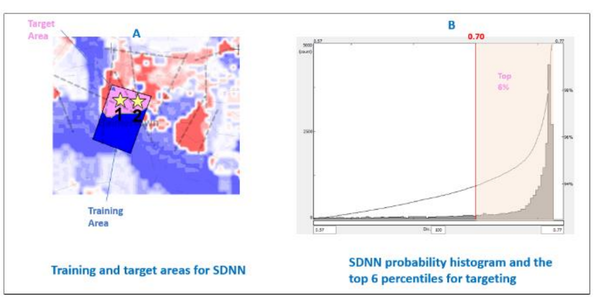

Figure 7: (A) Selected data area for training the SDNN; the red region covering the Campbell-Red Lake complex is the target area with value of 1.0. (B) The top 6% target probability histogram.

The selection criteria for targeting gold in the Red Lake camp consist of (1) targets are in the greenstone belt, and (2) targets are associated with high magnetic responses. Six (6) targets, RL_1 to RL_6, are identified, and they are displayed over the local geology in Figure 8. RL_1 covers the Campbell-Red Lake complex, and RL_3 includes the Cochenour-Willans mine. RL_1 is to the east of RL_1. RL_4 and RL_ 5 are in the northern part of the Red Lake greenstone belt. RL_6 is in the northern tip of the greenstone belt.

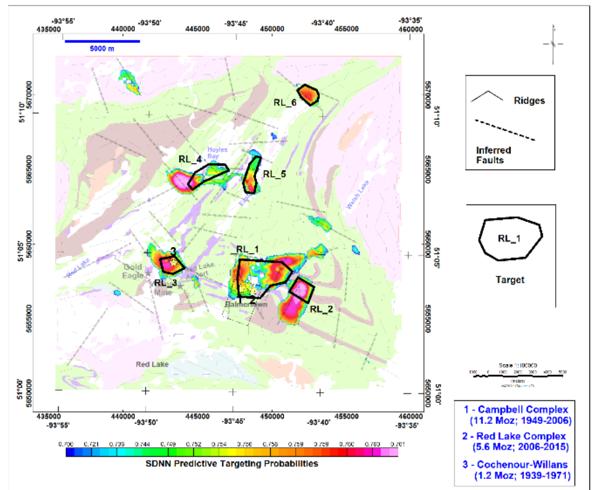

Figure 8: Selected gold targets over local geology of the Red Lake Camp.

The selected targets over the RTP data are shown in Figure 9. All the targets are associated with moderate to strong magnetic responses. The mafic to ultramafic rocks, and pyrrhotite are very magnetic.

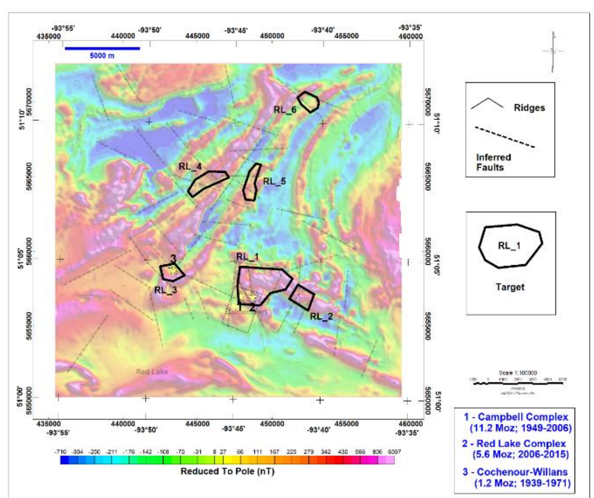

Figure 9: Selected gold targets over the RTP of Red Lake Camp.

4. Conclusions

A proposed S^3 method for targeting concealed orogenic gold mineralization is based on the geological concepts of Structural Complexity (SC) and Self-Organizing Criticality (SOC), and the integration of the SC and Self-Organizing Map (SOM) results together with the original aeromagnetic data by Supervised Deep Neural Networks (SDNN). The input of additional geoscientific information, including geophysical, geochemical, and remote sensing data into the SOM and SDNN modules is highly recommended. The selected predictive targeting probabilities derived from the SDNN provide options for the selection of exploration targets depending on a set of local geology-based criteria. Our study has tested the S^3 method using high-resolution aeromagnetic data from the Red Lake camp. The results are calibrated by known world-class gold deposits in the study area. Importantly, our study reveals four additional gold targets for future brownfields exploration in the camp.

Our study may be used as a template for the interpretation of integrated structural complexity and multiple geophysical datasets to identify potential orogenic gold targets in greenfield exploration. The selected targets greatly reduce the size of areas for further prospect- or deposit-scale investigations. This innovative method may help in the discovery of concealed orogenic gold deposits in Archean greenstone belts such as those elsewhere in the Superior Province, Canada.

Acknowledgements

This study is based on aeromagnetic data acquired and released to the public by the Ontario Geological Survey to whom we express our sincere appreciation and gratitude.

References

Dubé, B., Gosselin, P., 2007. Greenstone-hosted quartz-carbonate vein deposits. *In:* Goodfellow, W.D., (Ed.), Mineral Deposits of Canada: A Synthesis of Major Deposit-Types, District Metallogeny, the Evolution of Geological Provinces, and Exploration Methods: Geological Association of Canada, Mineral Deposits Division, Special Publication 5: 49-73.

Groves, D.I., Goldfarb, R.J., Gebre-Mariam, M., Hagemann, S.G., Robert, F., 1998. Orogenic gold deposits: A proposed classification in the context of their crustal distribution and relationship to other gold deposit types. Ore Geology Reviews 13: 7-27.

Groves, D.I., Goldfarb, R.J., Knox-Robinson, C.M., Ojala, J., Gardoll S., Yun, G., Holyland, P., 2000. Late kinematic timing of orogenic gold deposits and significance for computer-based exploration techniques with emphasis on the Yilgarn Block, Western Australia. Ore Geology Reviews 17: 1-38.

Groves, D.I., Santosh, M., Müller, D., Zhang, L., Deng, J., Yang, L.Q., Wang, Q.F., 2022. Mineral systems: Their advantages in terms of developing holistic genetic models and for target generation in global mineral exploration. Geosystems and Geoenvironment 1: 1-26.

Harris, J.R., Sanborn-Barrie, M., Panagapko, D.A., Skulski, T., and Parker, J.R., 2007.Gold prospectivity maps of the Red Lake greenstone belt: application of GIS technology, Canadian Journal Earth Sciences, 43, 865-893.

Holden, E.-J., Wong, J. C., Kovesi, P., Wedge, D., Dentith, M., Bagas, L., 2012. Identifying structural complexity in aeromagnetic data: An image analysis approach to greenfields gold exploration. Ore Geology Reviews 46: 47–59.

Hronsky, J.M.A., Groves, D.I., 2008. Science of targeting. Definition, strategies, targeting and performance measurement. Australian Journal of Earth Sciences 55: 3-12.

Hronsky, J.M.A., 2011. Self-organized critical systems and ore formation: the key to spatial targeting? SEG Newsletters 84: 14-16.

Kohonen, T., 2013. Essentials of the self-organizing map. Neural Networks 37: 52-65.

McCuaig, T.C., and Hronsky, J.M.A., 2014. The mineral system concept: the key to exploration targeting, SEG Special Publication 18, 153-175.

Ontario Geological Survey (OGS), 2017. Ontario Airborne Geophysical Surveys Magnetic Supergrids.

Percival, J.A., 2007. Geology and Metallogeny of the Superior Province, Canada. In: Goodfellow, W. (Ed.), Mineral Deposits of Canada: A Synthesis of Major Deposit Types, District Metallogeny, the Evolution of Geological Provinces and Exploration Methods, Geological Association of Canada, Mineral Deposits Division, Special Publication 5: 903–928.

Rehm, A.G., Jørgensen, T.R.G., Thurston, P.G., Gibson, H.L., Lafrance, B., 2021. Syn-sedimentary rifting and basaltic-komatiitic volcanism in the

Pontiac subprovince, Superior craton (Canada): Implications for Neoarchean geodynamics. Precambrian Research 362: 106204.

Robert, F., Poulson, H.K., Cassidy, K.F., Hodgson, J.C., 2005. Gold Metallogeny of the Superior and Yilgarn Cratons. Economic Geology 100: 1001-1033.

Sanborn-Barrie, M., Skulski, T., and Parker, J., 2004. Geology, Red Lake greenstone belt, western Superior Province, Ontario; Geological Survey of Canada, Open File 4594, scale 1:50,000.

Stott, G.M. 2011. A revised terrane subdivision of the Superior Province in Ontario; Ontario Geological Survey, Miscellaneous Release - Data 278.

Yousefi, M., and Hronsky, J.M.A., 2023. Translation of the function of hydrothermal mineralization-related focused fluid flux into a mappable exploration criterion for mineral exploration targeting, Applied Geochemistry, 149, 105561.

A Conservative Approach to Inversion with AI

James A. Craven, Geological Survey of Canada, 601 Booth St., Ottawa, ON K1A 0E8*
Xiaojun Liu, Geological Survey of Canada, 3303 33 St NW, Calgary, AB, T2L 2A7
Victoria Tschirhart, Geological Survey of Canada, 601 Booth St., Ottawa, ON K1A 0E8

Summary

Artificial Intelligence (AI) offers many advantages for large dataset analyses and is an attractive solution to many issues currently faced in geophysics. The physics underlying geophysical methods becomes increasingly complicated and time consuming to simulate as we attempt to model the earth in ever more realistic approaches. Working with geophysical data is predicated upon the concept of resolution. An inversion in the traditional sense can compute sensitivities based on the physics and creep or jump towards the best fit model for your data using guides from physics-based sensitivities whilst under some form of constraint such as maintaining model smoothness. This makes a lot of sense as it establishes a conservative framework that generates models that not only fit the data, but simultaneously supresses sporadic unresolved features not required by the data. However, similar physics-based guides and spurious feature constraints on AI models do not appear to be explicitly involved.

At the outset, therefore, it appears as if AI is both non physics based in its approach and its lack of explicit constraints suggests results may be untrustworthy. To investigate the first drawback, we took an approach using the magnetotelluric method (MT) as it has the property of uniqueness meaning the data collected, theoretically, are representative of a singular earth model. Working initially in 1D to more readily meet the uniqueness requirements allows one to attribute deviation from the true model as a failure in the AI methodology. To address the second drawback, we work with a convolutional neural network (CNN). A suitably trained CNN was validated with independent synthetic datasets, and the predicted resistivity distribution displayed an acceptable resolution and reliability, seemingly surpassing traditional smoothed inversion even when artificial noise was introduced. Based on these successes, the CNN was used to analyze MT data collected in Saskatchewan demonstrating the ability of the technique to reliably work with real world data.

Introduction

Artificial neural networks (NN) have demonstrated a considerable number of successful applications in different areas of study. Traditional EM inversion methods that can be quite time consuming as the earth models become increasingly complex. Due to the ability of NN algorithms to leverage a considerable speed up in wall clock time utilizing modern CPUs, it is worth investigating them to evaluate their ability to reliably retrieve unknown subsurface geo-electric structures. Puzyrev (2019), and Puzyrev and Swidinsky (2021) presented 1D inversion of EM induction data, controlled source EM and time domain EM (TEM) data using CNNs. The two studies displayed impressive results, laying the groundwork of CNN inversion for larger widespread use in EM geophysics. Liu et al. (2020) developed a sample-compressed NN algorithm for MT inversion and an adaptive-clustering analysis algorithm for resistivity boundary demarcation, and Guo et al. (2020) employed a supervised descent method for 2D MT data inversion to reduce uncertainty. Conway et al. (2019) applied a non-convolutional NN to approximate the 3D MT forward method instead of resolving the expensive forward functions, speeding up the inversion procedure and producing reasonable resistivity models. In spite of these advances, further study of MT inversion using CNN has yet to be performed.

In this study, we implement a multi-head CNN with residual block, which permits the use of measured MT resistivity and phase data and facilitates working in a multi-scale context. We test the sensitivity of our method to data noise and compare the results with a traditional inversion method, which shows an unexpected advantage of the proposed CNN inversion method.

MT Inversion with a CNN architecture

Geophysical inversion attempts to estimate the distribution of physical properties of the subsurface based on surface observed data. The proposed workflow in this study implements a significant concept of DL algorithm with CNN to predict the resistivity distribution from the measured apparent resistivity and phase data directly.

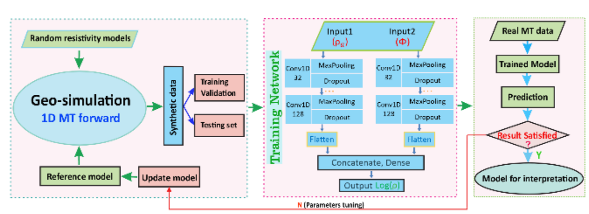

Figure 1. A schematic workflow of MT CNN inversion in this study (modified after Puzyrev and Swidinsky, 2021.

The quantity and quality of the data used for training the network model parameters is important for prediction accuracy. Randomized resistivity models were created for a 50-layer model with a resistivity range of 1 to 10^4 Ω m. The resistivity distribution in the model was randomly generated with a maximum of ten major anomalous resistive or conductive zones. The large amount of variably shaped resistivity models span most of the possible real world subsurface 1D geo-electric models without using any data augmentation methods. Continuous models were examined initially and underpin the results reported here, but preliminary study of discontinuous models is also reported herein. Layer thickness was fixed and responses at 128 frequencies were calculated within a range of 0.001–10,000 Hz. The forward module in the Occam inversion package was used for generating the apparent resistivity and phase (Constable et al., 1987). For this study, we generated 100,000 layered resistivity samples for model training and validation, taking about 40 minutes using a 56-core desktop computer. The base 10 logarithm of resistivity m=log10(ρ) was used as the targeted model parameters, and the input data were standardized similar to the form given by Puzyrev and Swidinsky, (2021).

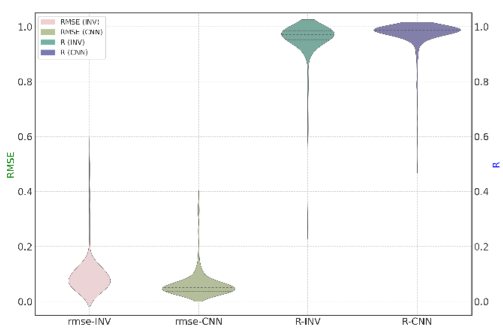

Figure 2. Violin plot of distribution of 300 tests (see text for detail) using CNN and traditional iterative inversion (INV).

Because both the apparent resistivity and phase are required as inputs for training, a popular multi-head CNN model architecture (Figure) was employed for this study (Canizo et al., 2019; Khan and Ahmad, 2021). The framework includes two parallel heads for feature analysis of apparent resistivity and phase. Each head was designed using similar 1-D CNN layers but different weights, to extract features from the corresponding input, then the interpretations of both heads were concatenated into one interpretation as a fully-connected layer (Canizo et al., 2019; Khan and Ahmad, 2021). Details on the network model can be found in Long et al. (2014), Ronneberger et al. (2014), Chen et al. (2017), and Puzyrev (2019). During training and validation, the network parameters were updated by minimizing the objective function, which is specified with the root mean squared error (RMSE) as the loss function metric,

$$rmse = \sqrt{\frac{1}{n}\sum_1^n (y_i^{pre} - y_i^{mod})^2},$$

where y_i^{pre} is predicted value and y_i^{mod} is the input model. The objective function of known resistivity models and their corresponding forward results is used to train the network with the Adam (adaptive moment estimation) optimization algorithm, which is an extension of the stochastic gradient descent for first-order gradient-based optimization that has recently seen broader adoption for DL applications.

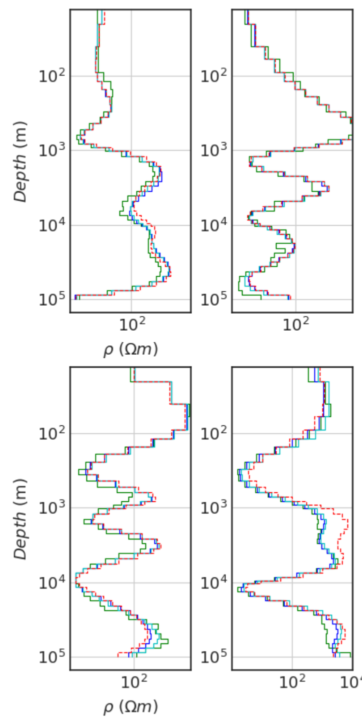

Figure 3. CNN inversion results of 4 models (green is true model) at different noise levels (blue is 0%, turquoise is 3%, red is 5%).

In this study, the model training took about 5 hours of computation time with a batch size of 64 using a single NVIDIA Quadro-P5000 GPU to reach a stable accuracy; the model with the best validation loss was saved during maximum 150 epochs. The network hyper-parameters (e.g. network structure, number of hidden layers, batch size, filter number and kernel sizes, activation function, and optimization function) were all adjusted during model training. In addition, we also checked different learning rates for model updating. We chose four hidden layers with a fixed kernel size of 3 for the final model. After the tests were verified, the same network architecture and weight parameters were saved and used in the rest of the program.

Comparisons with Traditional Inversions

In order to verify the accuracy of the proposed method, we compared the CNN predicted results with a traditional deterministic inversion method, which takes an initial model and updates the resistivity model until a best-fit is achieved with the observed data (Constable et al., 1987). Three hundred synthetic data were randomly generated using 1D forward simulation. During the inversion, the same layer thickness were used and the number of frequencies remained the same. We calculated and plotted the statistic distribution of misfit and R (correlation coefficient) based on testing with the synthetic models (Figure 2). The figure shows that the misfit RMSE distribution peak of the traditional inversion is higher than the CNN inversion, and the correlation coefficient peak is lower as well. We also can see the results of traditional inversion displays a larger variation than the CNN, as the quartiles are wider than CNN inversion. A few selected model comparisons are shown in Figure 3, (CNN model shown in blue, and true model shown in green). In general, the R and RMSE demonstrate that the resistivity models with CNN inversion are better recovered for this specific set of examples in comparison to traditional inversion.

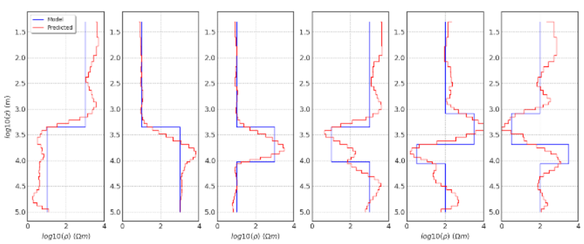

Figure 4. Comparison of predicted resistivity (red) using CNN inversion and true discontinuous layered resistivity models (blue).

Noise Stability of CNN Inversions

To ascertain the stability of this network in the presence of noise, the original resistivity and phase were distorted by adding random noise at different levels (3% and 5%) to the simulated apparent resistivity and phase (Figure 3). The CNN algorithm is stable with respect to noise, although more resistive features become less imageable as noise increases.

During the CNN model training and validation, we used layered models with continuous variable resistivity at the boundary between layers. To further test the reliability of the model prediction, we created a few simplified models with discontinuous layer boundaries and compared with the results of CNN inversion (Figure 4). The predicted resistivity distribution are consistent with the true models and show the trend of spatial variation, verifying the trained CNN model works date well for both continuous and discontinuous structures.

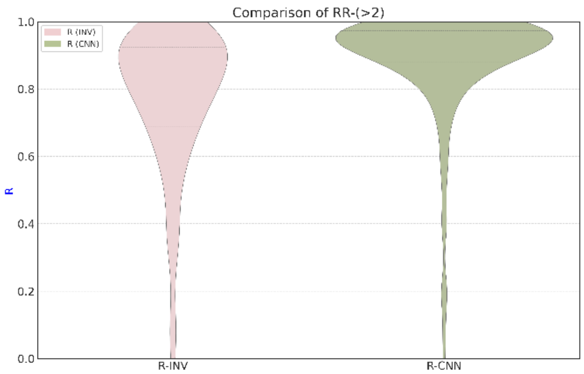

Figure 5. Comparison of correlation coefficient R for models containing layers greater than 100 ohm m.

Imaging Resistive Features

Visual inspection of a larger suite of model comparisons (not shown here, but similar to those shown in Figure 3) suggested that CNN could outperform traditional inversion for resistive features. To further examine this rather bold claim, we looked at R for model parameters associated with only resistivity values higher than certain thresholds. Figure 5 is one such comparison and the threshold in this plot is 100 ohm-m. The higher degree of correlation exhibited by CNN derived models highlights the success of the method to image relatively resistive features.

Real World Data Example

To test the accuracy of the trained 1D CNN model proposed in this study four sites were selected from dataset collected recently in northern Saskatchewan, Canada on the margin of the Athabasca Basin (Tschirhart et al, 2022). At periods corresponding to the uppermost crust, these data demonstrate circular phase tensors suggestive of 1D conductivity structures below the sites. This is reasonable geologically, as upwards of ~750 m of flat-lying resistive Athabasca Supergroup sedimentary rocks unconformably overlies Taltson Domain basement rocks, with no major interpreted intersecting faults. The determinant

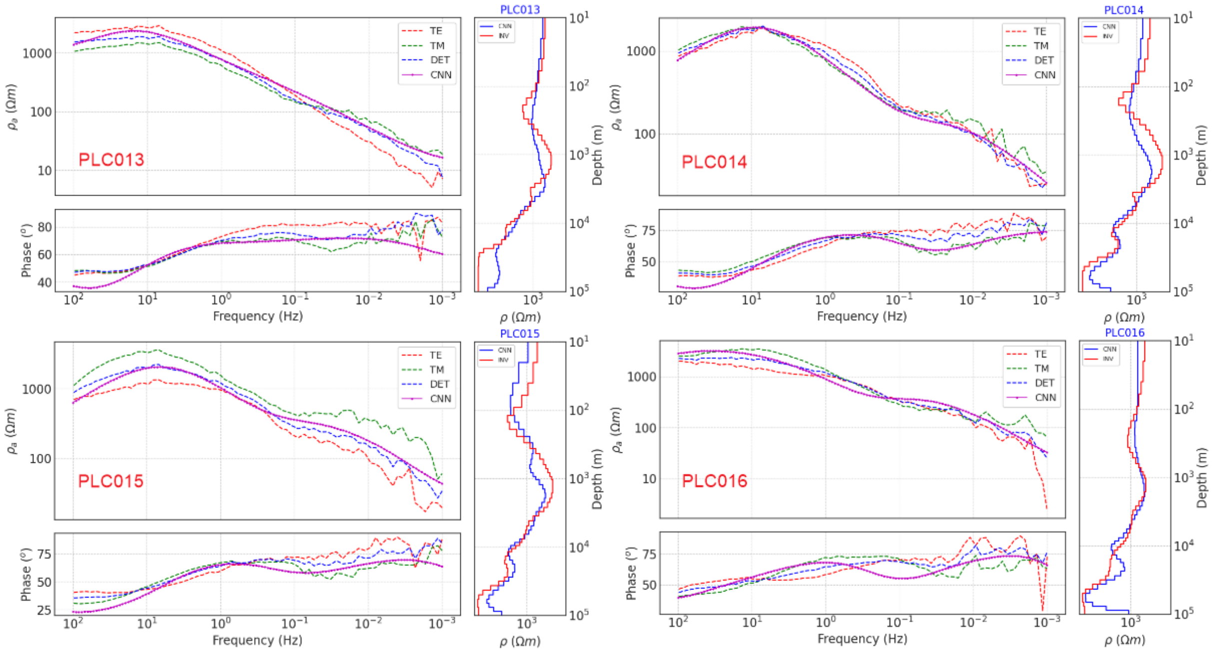

Figure 6. Sites PLC013, PLC014, PLC015, and PLC016. In the subplot of each site with comparisons of apparent resistivity between TE and TM modes, determinant (DET), and 1D CNN modeling responses in purple. The models arising from traditional inversion are shown red, and from CNN in the right panels.

average of the impedance tensor was used for model testing.

Comparison of the models found by CNN with the results of iterative inversion () indicates both methods locate a high resistivity zone around 1 km and display a similar trend in the overall resistivity distribution. There are some differences in the resistivity between the two methods in the near surface (<300 m) and mantle (>40 km) due to higher noise levels in the data. The deeper parts of the models are consistent across all four sites, where the resistivity decreases from 25 km to 40 km coinciding with the boundary between lower crust and mantle, located at ~35 km depth in the study area. A stitched resistivity section is shown in **Error! Reference source not found.**. The section d emonstrates a reasonable correlation in the resistivity variation between individual sites and between the two methods indicating CNNs work reliably with real world data.

Conclusions

DL or AI offer new efficient methods to analyze complicated data. They do not appear to directly incorporate physics, nor do they appear to offer any stability or smoothness constraints exhibited by traditional (i.e. conservative) inversion schemes. Our investigation into these issues supports the notion that indeed AI can be taught the physics needed and it can solve for the models without undue structure due to noise or other effects. In fact, it is shown here that AI can outperform traditional methods of data analysis

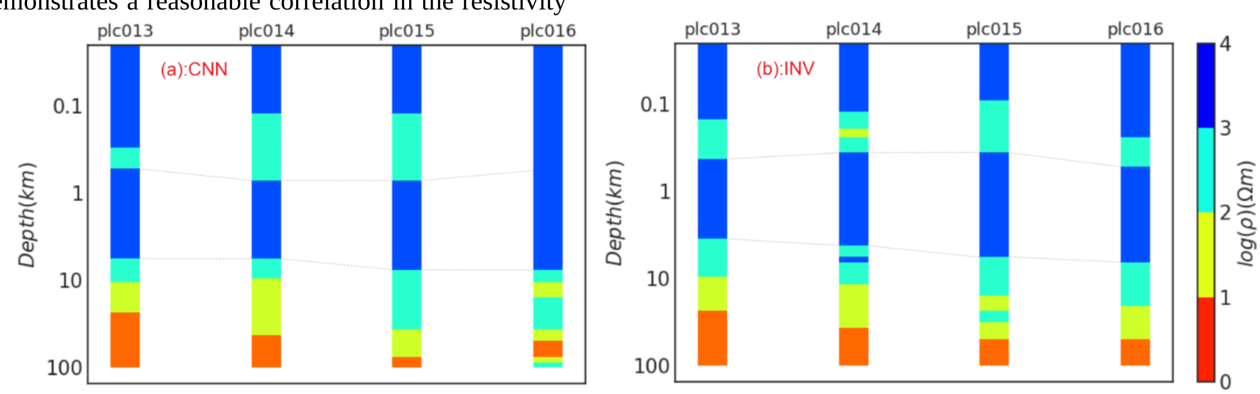

Figure 7. Resistivity sections of four calculated 1D models with CNN inversion (a), and iterative inversion (b).

especially in terms of imaging resistive features. Careful analysis and high quality data are required, but these results corroborate Jones (2019) and suggest MT can be used in non-traditional environments such as direct detection of electrically resistive oil or sequestered CO_2. Further work to verify the results beyond the test models shown here and using a wider range of CNN parameters is required, however. Extension of the CNN approach to 3D is currently underway.

References

Canizo, M., Triguero, I., Conde, A., and Onieva, E. (2019), Multi-head CNN–RNN for multi-time series anomaly detection: An industrial case study. Neurocomputing (Amsterdam), 363, 246-260.

Chen, L.C., Papandreou, G., Schroff, F., and Adam, H., (2017), Rethinking Atrous Convolution for Semantic Image Segmentation. CoRR, abs/1706.05587. 2017. URL: https://arxiv.org/abs/1706.05587v3.

Constable, S.C., Parker, R.L., and Constable, C.G. (1987), Occam's inversion: A practical algorithm for generating smooth models from electromagnetic sounding data, Geophysics, 52(3), 289-300.

Conway, D., Alexander, B., King, M., Heinson, G., and Kee, Y. (2019), Inverting magnetotelluric responses in a three-dimensional earth using fast forward approximations based on artificial neural networks. Computers & Geosciences 127, 44-52.

Fukushima, N. (1980), A self-organizing neural network model for a mechanism of pattern recognition unaffected by shift in position. Biological Cybernetics, 36(4), 193–202. doi:10.1007/bf00344251.

Guo, R., Li, M., Yang, F., Xu, S., and Abubakar, A. (2020), Application of supervised descent method for 2D magnetotelluric data inversion. Geophysics, 85(4), WA53-WA65. https://doi.org/10.1190/geo2019-0409.1.

Jones, A.G. (2019), Beyond chi-squared: Additional measures of the closeness of a model to data, ASEG Extended Abstracts, 2019:1, 1-6, DOI: 10.1080/22020586.2019.12072970

Khan, Z.N. and Ahmad, J. (2021), Attention induced multi-head convolutional neural network for human activity recognition. Applied soft computing, 110, 107671. URL: https://doi.org/10.1016/j.asoc.2021.107671.

Liu, W., Lü, Q., Yang, L., Lin, P., and Wang, Z. (2020) Application of Sample-Compressed Neural Network and Adaptive-Clustering Algorithm for Magnetotelluric Inverse Modeling. IEEE Geoscience and Remote Sensing Letters, 1-5. doi: 10.1109/LGRS.2020.3005796.

Long, J., Shelhamer, E., and Darrell, T. (2014), Fully convolutional networks for semantic segmentation. arXiv:1411.4038., https://people.eecs.berkeley.edu/~jonlong/long_shelhamer_fcn.pdf.

Puzyrev, V. (2019), Deep learning electromagnetic inversion with convolutional neural networks. Geophysical Journal International, 218(2), 817-832.

Puzyrev, V., and Swidinsky, A. (2021), Inversion of 1D frequency- and time-domain electromagnetic data with convolutional neural networks, Computers & Geosciences, 149, pp. 104681.

Ronneberger, O., Fischer, P., and Brox, T. (2015), U-net: convolutional networks for biomedical image segmentation. In: Medical Image Computing and Computer-Assisted Intervention (MICCAI), vol. 9351. Springer, LNCS, p. 234–241.

Tschirhart, V., Potter, E. G., Powell, J. W., Roots, E. A., and Craven, J. A., (2022), Deep geological controls on formation of the highest-grade uranium deposits in the world: Magnetotelluric imaging of unconformity-related systems from the Athabasca Basin, Canada, Geophysical Research Letters, 49, e2022GL098208, https://doi.org/10.1029/2022GL098208.

A comparison of airborne geophysical data over two magmatic nickel deposits

Blake Cross, Condor Consulting, Inc.*
Hannah Peterson, Condor Consulting, Inc.

Summary

Historic exploration for economical nickel (Ni) mineralization has often targeted magmatic sulfide deposits in extensional settings. However, convergent margin hosted Alaskan-type complexes represent a potentially underexplored source of Ni. Case studies of the geophysical responses associated with two magmatic-Ni deposits, one typical and one associated with an Alaskan-type complex, are presented and the results compared. Data was assessed from historic and newly acquired airborne geophysical surveys collected over the Mayville property in southeast Manitoba and the Turnagain property in northern British Colombia, explored by Mustang Minerals Corporation and Giga Metals Corporation, respectively. Airborne electromagnetic (EM) and magnetic data were utilized to make comparisons of the two properties and the mineralized zones specifically. The review showed that the Mayville magmatic sulfide deposit was directly detectible with electromagnetic methods, with passive and active source methods being complimentary to one another. The EM data did not directly detect the Turnagain Alaskan-type deposit, but the magnetics data proved to be successful in defining the geological framework. Implications for future targeting and exploration for economical Ni mineralization are considered.

Introduction

Nickel is a critical mineral according to the USGS; that is, a mineral that is "essential to the economic or national security of the U.S.…" The majority of Ni is used in stainless steel production but there is a growing demand for Ni in battery applications. Ni is primarily mined from Ni-laterites and from magmatic sulfide deposits, with the latter containing higher average grades and being the dominant source of current mining production, while the former is lower grade but makes up ~70% of the known Ni reserves (Bide et al., 2008). The higher grades of magmatic sulfide Ni deposits make them desirable exploration targets.

Within the magmatic sulfide deposit class, there are two generally recognized groups: sulfide-rich (10-90% sulfide minerals) which are typically associated with rift-related magmatism or komatiite flows, and sulfide-poor (0.5-5% sulfide minerals) which are notable for their PGE component (Schulz et al., 2010). Historically, convergent margins and subduction zone settings have not proven conducive to forming deposits with economical Ni mineralization (Thakurta et al., 2008) and have generally not been viewed as viable for sulfide-bearing mafic and ultramafic intrusions (Jackson-Brown, 2017; Ripley, 2010) which are typically necessary to form Ni-rich magmatic sulfide deposits. However, there are now several known Alaskan-type complexes, which are convergent margin related magmatic intrusions, that are known to contain economic sulfide-related mineralization (Nixon et al., 2017; Thakurta et al., 2008). These occurrences may indicate untapped exploration potential along convergent margins where additional mineralized Alaskan-type complexes may exist.

In this study, two Ni-bearing magmatic sulfide deposits in development (Collins et al., 2014; Thompson et al., 2020) are presented through a geophysical case study lens focussing on their airborne magnetic and EM responses. The first of the deposits is the Mayville M2 deposit in Manitoba, which is a classic geophysical exploration target: a sulfide-rich magmatic Ni deposit likely formed due to extension related magmatism (Collins et al., 2014). The second deposit is the Turnagain deposit in British Columbia, which is an unusual Ni deposit that formed as part of an Alaskan-type intrusive complex (Thompson et al., 2020). In addition to brief geophysical case studies of the two deposits, a comparison of the geophysical character of the two deposits is presented to offer perspective for future Ni exploration in potentially underexplored convergent margin settings and for Alaskan-type complexes.

Deposit Geology – Mayville M2

The Mayville property lies near Lac Du Bonnet in southeast Manitoba. The property hosts the Mayville M2 magmatic sulfide-rich Cu-Ni-PGE deposit consisting of an indicated resource of 26.6Mt with 0.18% Ni (Figure 1). A preliminary economic assessment (PEA) was completed in April 2014 (Collins et al., 2014).

The primary mineralization is typical of a magmatic sulfide assemblage, being composed of pyrrhotite, pentlandite, and chalcopyrite, with textures ranging from finely disseminated, to semi-massive net-textured, to inclusion-bearing massive sulfide (Collins et al., 2014). The intrusion dimensions are approximately 10 km in length and 1.1 km in thickness (Collins et al., 2014). Higher grades have been noted to occur on the basal contact of the intrusion. Chromite mineralization is also found within the property limits.

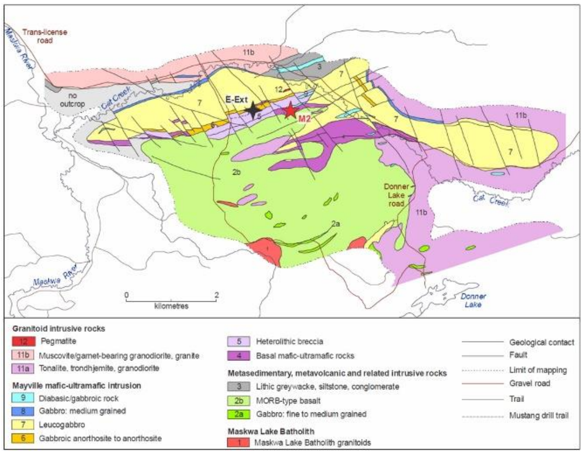

Figure 1. Simplified geologic map of Mayville intrusion (Bécu & Houlé, 2014).

Deposit Geology - Turnagain

The Turnagain property is located in British Columbia and lies about 70 km east of Dease Lake. The property hosts Ni-Co-PGE sulfides in an Alaskan-type intrusive complex (Figure 2).

Alaskan-type intrusive complexes typically consist of a steeply dipping dunite-wehrlite core that transitions to hornblende-rich or magnetite-rich clinopyroxenites at the margins (Nixon et al., 2017; Nixon and Rublee, 1988). The Turnagain intrusion is unique in that most Alaskan-type intrusions are not accompanied by the economic minerals found at Turnagain. The sulfur saturation necessary to precipitate a Ni deposit was most likely reached when the intrusion interacted with the preexisting carbonaceous phyllite wall rocks and scavenged the necessary sulfur content (Nixon, 1998; Scheel, 2007). The property has been developed to a PEA stage (Thompson et al., 2020) and has a measured and indicated resource of 1.042Bt with 0.22% Ni and 0.013% Co. The complex is approximately 8 km by 3 km in size (Figure 2).

Economic mineralization at Turnagain occurs as semi-massive and massive sulfides which are generally hosted by dunite and wehrlite near the southern and eastern margins of the ultramafic body. The principal sulfide minerals associated with mineralization are pyrrhotite, pentlandite, and chalcopyrite, with some trace bornite. PGE minerals have also been identified.

Geophysical Data Collection and Processing

On the Mayville property, heliborne Versatile time-domain EM (VTEM) surveys were flown by Geotech Ltd. (Geotech) in 2005 and 2010 and a heliborne Z-axis tipper EM (ZTEM) audio-frequency magnetic (AFMAG) survey was flown by Geotech in 2010. AeroTEM II heliborne EM and magnetic data were acquired over the Turnagain property in 2004.

Geophysical data processing included calculation of an EM time-constant (tau, or AdTau), conductor picking, 1D layered earth inversions of the EM data, 2D and 3D modeling of the ZTEM data, magnetic grid processing, and 3D magnetic susceptibility modeling.

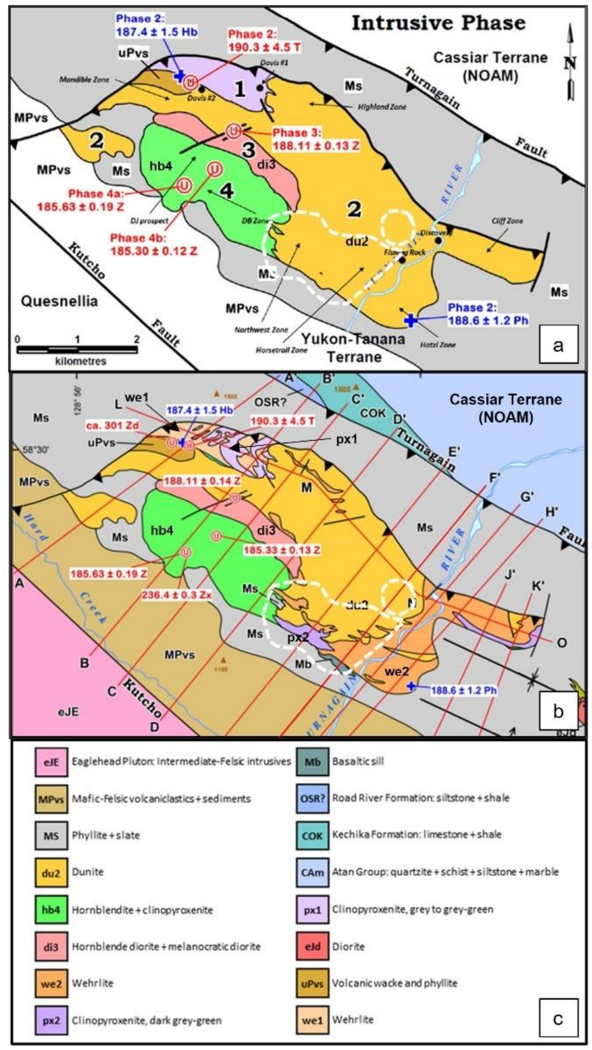

Figure 2. Simplified geology from the Turnagain intrusion (adapted from Nixon et al., 2017) with planned pit outline from Thompson et al. (2020) shown by white dashed line. (a) The Turnagain ultramafic complex was emplaced in four distinct phases. Note the various named prospects and mineralized zones located inside the intrusive complex. (b) Detailed geologic map over the Turnagain ultramafic complex. (c) Geologic legend for the map in (b).

Results

On the Mayville property, the TEM data show generally higher conductivities aligning with the ultramafic intrusions (Figure 3 and 4). Over the M2 deposit a 1.2 km west- southwest-trending tau anomaly appears to reflect mineralization. M2 is also associated with a single, semi-linear west- southwest-trending conductor axis comprised of VTEM picks and closely aligning with the AdTau response. The M2 deposit is well-defined at both high and low frequencies in the ZTEM data and is well mapped at depth by the 3D conductivity inversion of the ZTEM data (Figure 4).

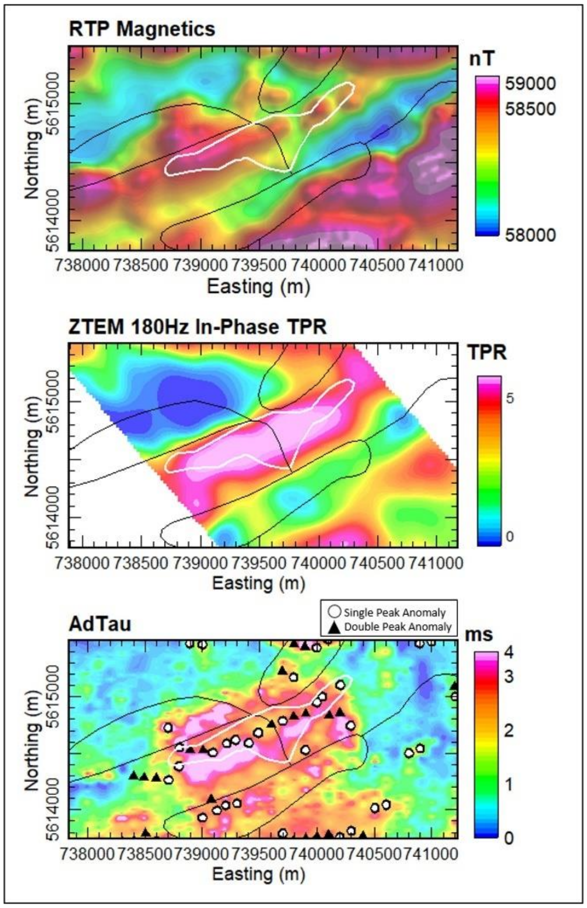

Figure 3. Geophysical responses over the M2 mineralized zone with 1:250,000 scale geologic boundaries from the Manitoba government database outlined in black and the M2 resource outlined in white. (a) Reduced-to-Pole magnetics. (b) ZTEM Total Phase Rotation (TPR) of In-Phase Tipper at 180 Hz (c) AdTau with EM discrete response picks.

The results at Mayville show strong magnetic intensity highs with an east-west trend closely associated with the strike of geologic contacts (Figure 3). A well-defined high magnetic response aligning with the M2 deposit extends past the limits of the interpreted conductor. Generally, the mafic bodies such as gabbros and basalts are correlated with higher magnetic domains while the surrounding felsic granites and granodiorites correspond with lower magnetic intensity.

On the Turnagain property, the EM data distinctly map the boundary between the graphitic phyllite meta-sediments of the Ms unit and the formations within the Cassiar Terrane, which are separated by the Turnagain fault (Figure 5). However, the known resource is only partially aligned with the apparent conductive zone and is not well defined by it. The majority of EM conductor picks occur in the southwest portion of the Turnagain complex in the vicinity of the known resource and trend west-northwest, but these also only exhibit a partial alignment.

The magnetic data from the Turnagain property reveal the ultramafic complex to occur as a well-defined zone of elevated, but variable, magnetic highs. Within the ultramafic complex the varied responses partially appear to map the boundaries of the different intrusive phases. The 3D magnetic susceptibility results indicate that the ultramafic complex has a higher magnetic susceptibility than the surrounding phyllite host rocks (Figure 6). The planned pit outline (Thompson et al., 2020) generally aligns with the highest magnetic susceptibility portions of the magnetic model (Figure 6). The magnetic results are also highly effective at revealing faulted lithologic contacts.

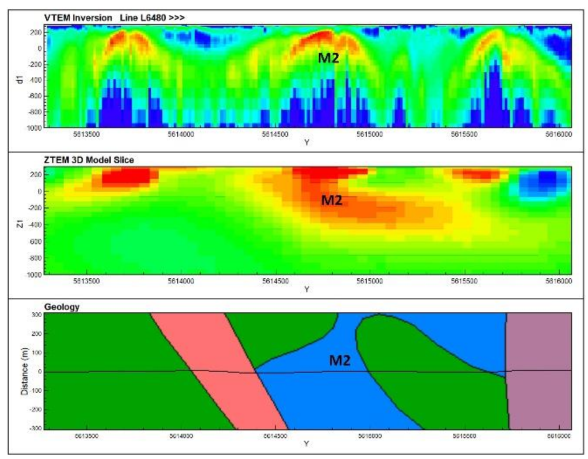

Figure 4. Conductivity-depth sections across the Mayville M2 mineralized zone derived by 1D inversion from VTEM Z-component dB/dt EM response amplitude (top) and 3D inversion from ZTEM data (middle) and local geology in plan-view showing the VTEM flight line in black (bottom). Geologic units: pillow basalt (green), quartz diorite (pink), gabbro (blue) and gneiss (purple).

Discussion and Conclusion

Discrete EM anomalies and their overall trends generally exhibit an association with mineralization for both Mayville and Turnagain. The EM data also help characterize the geologic structure, lithology, and faults on both properties. There is excellent agreement between the Mayville deposit and a series of highly conductive discrete EM responses, although the association is not as clear at Turnagain. However, at the Turnagain property the AeroTEM data are very effective at outlining the intrusive complex and regional geologic contacts. It is possible that the lack of clear conductors associated with the Turnagain deposit is a result of the relatively low sulfide content associated with mineralization; this response may be expected in other mineralized Alaskan-type deposits which, while they have met the necessary sulfide content to emplace Ni mineralization, have not formed sufficient massive sulfide content to produce a distinct EM conductor response.

The magnetic data across both properties serve as a useful tool for mapping lithology, contacts, and faults. The mafic/ultramafic intrusive bodies that host the mineralized zones are reasonably well mapped by areas of high magnetic intensity. However, neither deposit clearly demonstrates an anomalous magnetic response to be associated with economic mineralization within the host intrusive.

Overall, the Alaskan-type Turnagain intrusive complex as a whole is well mapped by both the magnetic and EM data, though follow up would be necessary to precisely map the mineralized zones within. Active-source EM was most effective at direct mapping of mineralization at the classic Ni-bearing magmatic sulfide Mayville M2 deposit, while the Ni mineralization within Turnagain exhibited a weaker association with discrete conductors. These results indicate that airborne magnetic and EM methods remain effective tools for Ni-sulfide mineralization, regardless of the formational environment and deposit style. The genetic association of mafic/ultramafic intrusive bodies with the deposit types considered in this report make them both compelling geophysical targets, even at depth. In areas of detectable physical contrasts, methods such as natural-source EM (AFMAG) may be used to detect ore-hosting intrusives even in deep settings.

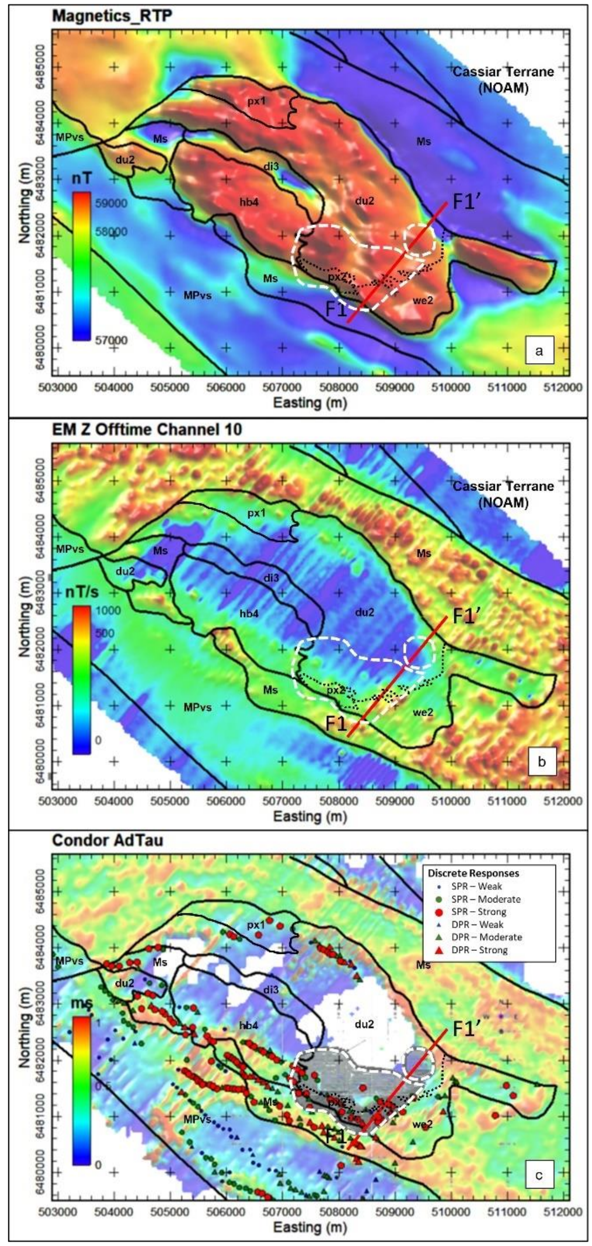

Figure 5. Geophysical responses over the Turnagain intrusive complex with geologic boundaries and intrusive phases from Figure 2(a) outlined in black. Planned pit outlines from Thompson et al. (2020) shown in gray. (a) Reduced-to-Pole Total Magnetic Intensity (TMI) magnetics. (b) Mid-time EM Z off time channel 10 showing EM response amplitude. (c) AdTau representing conductivity with conductor picks ranked by strength. Cross section for Figure 6 indicated by solid red line F1-F1'.

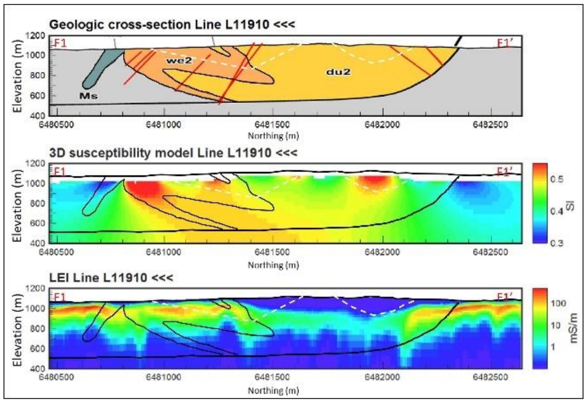

Figure 6. From top to bottom: geologic cross-section from Turnagain (legend in Figure 2), susceptibility-depth and conductivity-depth sections derived from the AeroTEM survey data via 3D and 1D inversions, respectively. The line location is indicated in Figure 5. Interpreted geology outlined with black lines and planned pit outline from Thompson et al. (2020) shown by white dashed line.

Acknowledgements

The authors would like to thank the SEG and The Leading Edge, who have copyright of the material, for allowing us to share the results. This work will be published in The Leading Edge, Vol. 42, No. 4. The authors would like to acknowledge Mustang Minerals and Giga Metals for permitting publication of the results, as well as Geotech and AeroTEM for their contributions in acquiring the geophysical datasets. We would also like to acknowledge Daniel Sattel (EM Solutions, LLC.) for airborne EM processing.

References

Bécu, V, and M.G. Houlé, 2014, Chromite Occurrences of the E-Ext stripped outcrop, Mayville intrusion, Bird River greenstone belt, southeast Manitoba: Manitoba Mining and Minerals Convention, https://doi.org/10.4095/296135.

Bide, T., L. Hetherington, and G. Gunn, 2008, Nickel – Mineral profile: British Geological Survey.

Collins, S., R. Pressacco, D. Ross, H. Miranda, and H. Krutzelmann, 2014, Technical report on the preliminary economic assessment of the combined Mayville-Makwa Project, Manitoba, CA, NI 43-101 Report, Mustang Minerals Corp: Technical Report.

Jackson-Brown, S., 2017, Origin of Cu-PGE-rich sulphide mineralization in the DJ/DB zone of the Turnagain Alaskan-type intrusion, British Columbia (T): University of British Columbia. https://open.library.ubc.ca/collections/ubctheses/24/items/1 0355222.

Nixon, G. T., and V. J. Rublee, 1988, Alaskan-type Ultramafic Rocks in British Columbia – New concepts of the structure of the Tulameen Complex: BC Ministry of Energy, Mines, and Petroleum Resources, Geological Fieldwork, 1988-1, 281–294.

Nixon, G.T., 1998, Ni–Cu 9 mineralization in the Turnagain Alaskan-type complex: a unique magmatic environment. In: Geological Fieldwork 1997, British Columbia Ministry of Energy, Mines and Petroleum Resources, British Columbia Geological Survey, 1998-1, 18-1–18-12.

Nixon, G. T., J. E. Scheel, R. M. Friedman, C. J. Wall, J. Gabites, D. Miller, and J. S. Scoates, 2017, Geology and geochronology of the Turnagain ultramafic-mafic intrusion, BC: BCGS Geoscience Map 2017-1.

Ripley, E.M., 2010, Chapter 24 - A new perspective on exploration for magmatic sulfide-rich Ni-Cu-(PGE) deposits: Society of Economic Geologists Special Publication 15, 437–450, https://doi.org/10.5382/SP.15.2.06.

Scheel, J.E., 2007, Age and origin of the Turnagain Alaskan-type intrusion and associated Ni-sulphide mineralisation, North-Central British Columbia, Canada: M.S. thesis, University of British Columbia.

Schulz, K.J., V.W. Chandler, S.W. Nicholson, N.M. Piatak, R.R. Seal, L.G. Woodruff, and M.L. Zientek, 2010, Magmatic sulfide-rich nickel-copper deposits related to picrite and (or) tholeiitic basalt dike-sill complexes: A preliminary deposit model, https://doi.org/10.3133/ofr20101179.

Thakurta, J., E.M. Ripley, and C. and Li, 2008, Geochemical constraints on the origin of sulfide mineralization in the Duke Island Complex, southeastern Alaska: Geochemistry, Geophysics, Geosystems, 9, 1–34, https://doi:10.1029/2008GC001982.

Thompson, I., P. Rosario, E. Jones, G. Schwab, S. Hloucschko, G. Kirkham, D. Friedman et al., 2020, 43-101 Technical report & preliminary economic assessment for the Turnagain Project - Amended: Technical Report.

AEM modelling and system options in the search for critical mineral systems in a regolith dominated environment – the Musgrave Province, Central Australia.

[1]Tim Munday, [2]Mike McMillan, [3]Rod Paterson, [4]Camilla Soerensen and [5]Noelene Dorn*
[1]Deep Earth Imaging FSP, CSIRO, 26 Dick Perry Av, Kensington, Perth, WA 6151: Australia; tim.munday@csiro.au
[2]Computational Geosciences Inc., 1623 W 2nd Ave, Vancouver, B.C. V6J 1H3 Canada; mike@compgeoinc.com
[3]Intrepid Geophysics, Suite 110 / 3 Male Street, VIC 3186 Brighton, Australia; rod@intrepid-geophysics.com
[4]Aarhus Geosoftware, Inge Lehmanns Gade 10, 05.030 - 8000 Aarhus C, Denmark; camilla.soerensen@seequent.com
[5]ElectroMagnetic Imaging Technology Pty Ltd, 23 Junction Parade, Midland WA 6056, Australia; ndorn@electromag.com.au.

Summary

The Musgrave Province is a Mesoproterozoic crystalline basement terrain that extends across the central part of Australia. The Province is prospective for critical and other important minerals, including Ni (sulphide and lateritic), Cu, PGE, Au, Pb, Zn, C, chromite, V, ilmenite, REE, U, W, and Sn. The region is also characterized by an extensive conductive transported cover overlying an in-situ regolith. Airborne electromagnetics (AEM) is used as a key exploration technology in this setting, with exploration surveys commissioned to assist the direct targeting of mineral systems, but also to aid geological mapping and regolith characterisation. While the choice of survey technologies and interpretation method can, in part, be informed by forward modelling approaches, more direct assessments with data acquired under actual survey conditions can be particularly informative.

Here we discuss the application of 1, 2 and 3D inversion approaches to resolving the geometry and complexity of the geology in an area on the South Australian side of the Musgrave province and consider modelled responses from coincident lines of fixed wing (SPECTREM-Plus and TEMPEST – High Moment), and heliborne (VTEM and SkyTEM) time domain EM systems over a known deep, steeply dipping conductor which typifies some of the exploration targets in the region. The 1D inversion scheme - AarhusInv was used for the processing and inversion of the three AEM data sets. Similarly, all data sets were inverted with the 2D Moksha code developed by Intrepid Geophysics. The algorithm incorporates a 2D inversion solver with adaptive regularisation, allowing the incorporation of a misfit to the reference model and the model smoothness function. Finally, the same data were inverted using Computational Geoscience's 3D inversion applying an induction-only approach with individual survey lines inverted in "2D-mode", with additional regularization applied in the cross-line direction, while still modelling the full 3D physics.

All inversion methods and systems contributed to our understanding of geological variability and structural complexity, although all generate smoothed versions of geological reality. Results from the 1D inversions appear to map geological variability and complexity in the near surface (regolith character?) in greater detail compared to those from the 2 and 3D inversions, even though the geology is recognisably 3D in character. While the 2 and "3D" models have good global data fits, in some instances they failed to replicate the measured data at late time, consequently overlooking known (from ground EM and drilling) small discrete inductive targets.

Introduction

It is well known that the search for critical minerals (e.g. Nickel, graphite, Cu) in Australia using airborne electromagnetics is challenged by a complex regolith cover, with thicknesses often exceeding 100m. This cover, commonly conductive, can mask or distort the geophysical expression of buried mineral systems. In the Musgrave Province of NW South Australia, prospective for magmatic nickel-copper, PGE's, and iron oxide copper gold (IOCG) (Woodhouse and Gum 2003), extensive conductive transported cover overlies an in-situ regolith (Figure 1 and 2A). Combined they create a challenging exploration environment. Airborne electromagnetics (AEM) has been commonly employed as part of an exploration of mafic to ultramafic layered intrusions which are the primary focus for Ni-Cu mineralisation. These intrusions (e.g. of Giles Complex - Figure 2B) which commonly occur as a series of vertically stacked dykes act as potential traps for Ni-Cu sulphides. The motivation for conducting this research was an interest in the application of 1, 2 and 3D inversions with non-dispersive, conventional conductivity or resistivity modelling codes, applied to the targeting of conductive 'critical mineral system' targets at depth in complex weathered settings. Their ability to resolve other relevant geological characteristics, such as regolith thickness and spatial variability (also aspects of the "mineral system") was also of concern. Some may argue that the choice of survey technologies and interpretation method can, in large measure, be informed by forward modelling approaches. We accept this has merit, but also believe that more direct assessments with data acquired under survey conditions can be equally informative. This work builds on earlier studies undertaken in the area by Ley-Cooper et al (2015).

Assessments such as that discussed here have been documented in other instances (e.g. Sattel , Viezzoli and Selfe (2018), Christensen and Lawrie (2012), among others. In this study we examine the definition of a small, conductive dipping target – the Valen Prospect, supported by ground and drillhole geophysical investigations and associated modelling.

Geophysical Systems and Interpretation Methods

AEM systems

Coincident data from four AEM systems (two heli-borne – VTEM and SkyTEM 508; and two fixed-wing -TEMPEST High Moment, and SPECTREM Plus) were examined in this study. It is useful to note that the acquisition of VTEM data was initiated over the study area in 2011, and surveys by other systems continued intermittently up to early 2019. We accept that while developments in all the AEM systems mentioned have continued since that time, we believe the results discussed here remain relevant and informative to explorers for critical mineral systems in the present.

Heli-borne AEM systems

Table 1 details the system parameters for the two helicopter EM systems considered here. There is little difference in the size and heights of the respective Tx loops and Rx coils for the two. The main difference between the systems is in the Tx waveform, ramp time, and receiver gate times: The SkyTEM system is about 15% more powerful in terms of peak dipole moment The SkyTEM system has a much faster current-off ramp (0.2 msec vs 1.38 msec), which will result in different early-time responses. The VTEM system uses a longer on-time with a complex trapezoidal waveform, which is claimed to better energise late-time conductors. However, the late-time gate widths of the SkyTEM system are about twice those of the VTEM system, potentially allowing for better signal-to-noise at later times.

Table 1: Helicopter EM System Parameters

Parameters \ AEM System	VTEM	SKyTEM508
Tx Diameter	26m	28.6-30.6m
No. Turns	4	8
Tx Area	531m^2	508m^2
Tx Elevation	44m	45m
Nominal Current	200A	121A
Peak Moment	425 000 A.m^2	492 000 A.m^2
Base frequency	25Hz	25Hz
Effective Area	113.1m^2	105m^2
Rx Elevation	44m	47m
Waveform	Trapezoid	Square
On-time	6 msec	5msec
Ramp	1.38msec	0.2msec
Duty Cycle	37%	25%
Gate times	0.078-11.458msec	0.0234-1.484msec (LM)
		0.238-19.921 msec (HM)
No. Channels	36	19 (LM); 18 (HM)

Fixed-wing AEM systems

Data from two fixed-wing time domain EM systems were considered here. These included the SPECTREMPLUS and an experimental variant of the TEMPEST system – the TEMPEST High Moment TDEM system. Details of the systems parameters are detailed in Table 2 below. The High Moment TEMPEST was an experimental system developed by CGG (now Xcalibur), flown on a Casa 212 aircraft, while the SPECTREM system is mounted in a Basler-DC3.

Table 2: Fixed-Wing AEM system Parameters

Parameters \ AEM System	SPECTREM PLUS	TEMPEST High Moment
Base frequency	25Hz	25 Hz
Transmitter area	420m^2	244 m^2
Transmitter turns	1	1
Waveform	Square	Square
Duty cycle	100%	50%
Transmitter off-time	N/A	10 ms
Transmitter turnoff	N/A	80µs
Peak current	1,600 A	1,200 A
Peak moment	672 000 A.m2	288 000 A.m^2
Sample rate	76.8kHz	75 kHz on X and Z
System bandwidth		25 Hz to 37.5 kHz
Nominal Flying Height	91m	120 m

(subject to safety considerations)		
EM sensor	Towed bird - 3 component dB/dt coils	Towed bird - 3 component dB/dt coils
Tx-Rx horizontal separation	131m (nominal)	117 m (nominal)
Tx-Rx vertical separation	36m (nominal)	41.5 m (nominal)
Stacked data output interval		200 ms (~12 m)
Number of output windows	10	15
Window centre times	0.0065 to 16.65	13 µs to 16.2 ms

Inversion

Several inversion approaches were examined, including 1, 2 and 3D methods. In all cases, the inversions were undertaken with an induction only AEM inversion code, that is no account was taken of IP/SPM effects that are known to be present in the area. In addition, information from the ground TEM and drillhole DHEM and the presence of an inductive target was known prior to modelling using the different codes.

1D AarhusInv
The 1D inversion scheme AarhusInv (Auken et al., 2015), was employed through the Aarhus Workbench to process and invert all four AEM data set. Lines coincident to the VTEM line 30390 (Figure 2) were processed manually to remove noise. The AarhusInv code inverts soundings for a set of 1D models connected through constraints. In this study the LCI approach was taken with relatively loose horizontal and vertical constraints used. All data from the different systems was inverted using a smoothg model inversion with 30 layers. Only Z component data was inverted for the helicopter systems, whereas the TEMPEST and SPECTREM lines were inverted with X and Z and also for geometry (bird position and pitch). A depth of investigation (DOI) was also defined using the method of Christiansen and Auken (2012) with two different DOI were calculated, one standard and another more conservative.

2D Moksha-EM
A 2D (or 2.5D) inversion of the four airborne data sets was undertaken using the Moksha-EM 2.5D code (Paterson et al., 2016, and Silic et al., 2015). As a re-engineered version of ArjunAir (Wilson et al., 2006), it incorporates a 2D inversion solver with adaptive regularisation which allows the incorporation of a misfit to the reference model and the model smoothness function. The regularisation parameter, chosen automatically, changes adaptively at each iteration, as the model, the sensitivity and the roughness matrices change (Silic et al., 2015). The estimation of regularisation parameter requires calculation of only one forward model and sensitivity matrix at each iteration and is controlled by an easily understood parameter - the Relative Singular Value Truncation (RSVT) parameter.

In this study Z component data were inverted for the helicopter data sets with a 40m (lateral dimension) mesh, and a 5m mesh at surface increasing with depth down to 450 m. For the SPECTREM and TEMPEST data both X and Z component data were jointly inverted.

2D/3D CompGeo/UBC
A 3D inversion of the AEM data sets was also undertaken using an adaptive OcTree mesh refinement, where the mesh spans the full computational domain but uses smaller mesh cells around the selected transmitters and receivers. This mesh refinement methodology results in a forward modelling mesh that has far fewer cells than the full inversion mesh. This procedure results in a highly parallel 3D inversion algorithm that can handle large datasets, building on the approach described by Haber et al., (2012), Oldenburg et al (2013), Schwarzbach et al., 2013, and Yang et al., (2014).

For this study, each line of observed data was inverted separately in 3D using an induction only AEM inversion code employing an OcTree mesh for all inversions where the smallest cell size in the core region is (20m×20m×10m), and uncertainty assignments of 3%, plus a floor of 1×10^{-13} V/Am2 for SkyTEM (high-moment), 3% plus a floor of 5×10^{-10} V/Am2 for SkyTEM (low-moment) and 3% plus a floor of 1×10^{-9} A/Am for SPECTREM and TEMPEST data. The 3D inversions for the individual lines were run in “2D-mode”, meaning there was additional regularization applied in the cross-line direction, while still modelling the full 3D physics.

3D inversions were run with data sets where there were three adjacent lines (in the case of SPECTREM, SkyTEM and VTEM). The lines were inverted as one combined 3D model for each input dataset. With 200m spaced lines it was deemed that the lines were spaced too far apart for the “all-at-once" 3D inversion to be better than the individual line 2D inversions.

Results

Results from a set of coincident survey lines that transgress a complex transported regolith (Cenozoic) cover (Figure 2A) overlying weathered and deformed Mesoproterozoic rocks including layered mafic-ultramafic layered intrusions (Giles Complex), and felsic and minor mafic gneisses (Birksgate Complex) (Figure 2B) are presented here. The geology along the line is summarised in Figure 3. Initial exploration targeting by Musgrave Minerals used VTEM data, and a late time anomaly – the Valen Prospect (Figure 3) was identified in amplitude responses and imagery. This was then followed up by ground TDEM which confirmed the presence of a conductor, modelled as plate in MAXWELL (Figure 4A). The top was modelled as being approximately 100m below the surface, dipping at approximately 60 degrees to the north. The target was then drilled and drilling intersected minor accumulations of sulphide mineralisation but did not encounter any conductive source at the modelled depth of 65m. However, it intersected a 30cm zone of massive graphite at about 89.5m, which is attributed to the source of the TEM anomalism. A second graphitic shear zone was intersected at about 100m with some minor graphitic horizons and zones of matrix pyrrhotite between these depths. Plate modelling for both SkyTEM and VTEM late time data (defined two similar plates (Figure 4A). The ambiguity in the depth estimates and discrepancy between the depths of the MLTEM, DHEM and AEM models may be explained in part by the complex geology. Down hole EM (DHEM) undertaken through the zone of mineralisation indicated that the target exhibited an inductive response.

Modelled responses for each AEM system (along coincident flight lines) derived using the different inversion approaches are presented as conductivity depth sections in Figures 5 and 6. 1D laterally constrained, smooth model LEI, are displayed in Figure 5 (left column). All AEM systems define a conductive regolith varying in thickness, with thicker conductive layers associated with palaeovalley fill sequences. The 1D code pushes the modelled conductor associated with Valen was defined in each of the AEM systems examined but it was placed at much greater depths than suggested by the ground TDEM.

Conductivity depth sections derived from the inversion of each AEM system along the transect of interest using the Intrepid Geophysics 2D (2.5D) Moksha-EM codes are shown in Figure 5 (right hand column of sections). As with the 1D codes, the sections define a conductive regolith of varying thickness over a resistive basement, with all AEM systems showing a similar conductivity structure. Although they all have responses to the Valen late time feature the 2.5D inversion does not fit any of the responses. TEMPEST and SPECTREM both have X component responses in the same location but no response is modelled in joint X and Z inversions.

Finally, the observed data from all systems, inverted separately in 3D using an induction-only inversion code is shown in Figure 6. 3D inversions, modelling the full 3D physics, for coincident lines were initially run in ”2D-mode”, with additional regularization applied in the cross-line direction (Figure 6 – left column). Where data and line density permitted (with VTEM, SkyTEM and SPECTREM data sets), 3D inversions (Figure 6, right column) were run with the three lines together as one combined 3D model for each dataset. With relatively small targets and with 200m spaced lines results suggested that the lines were spaced too far apart for the “all-at-once” 3D inversion to be better than the individual line inversions. The individual inversions consistently had the best data fits and overall models for this project. If the data had been acquired with 100-150m line spacing, where there is a greater overlap of sensitivities between lines, or if more complex 3D geologic features were encountered. then the all-at-once approach may resolve greater detail. Interestingly, the 2D and “all-at-once” 3D inversions of the SkyTEM data model a small conductor close to the indicated position of the Valen “mineralisation”, but this is not reproduced in the results for the other systems. Further work is required to understand why this occurs.

Conclusions

The choice of exploration technologies and their incorporation in an exploration workflow will vary with the experience and preferences of those involved. In the geological setting of the Musgraves, the application of AEM in the search for Ni-massive sulphides or other critical minerals will almost always be a case of “bump-finding”, including some fast modelling (i.e. 1D LEI) and the ground follow-up. In this study, small late-time conductive anomalies were detected by fixed-wing and heli-borne EM systems indicating their relevance to exploration in this environment. Arguably, the choice of system may come down to whether low noise, strong late time responses and target sensitivities are important in prioritising targets. It is apparent that system noise, particularly at late time will have a significant influence of model results. The choice of the noise floor and regularisation can influence the results obtained. That said, it’s likely that in true greenfield settings small targets such as Valen will be followed up by ground EM regardless of system choice, if only to better characterise the mineral systems present and to better determine the prospectivity of the area of interest.

This study suggests that the selection of a particular inversion approach may yield comparable results for different systems at a coarse scale, but significant differences at finer scales, particularly for the regolith cover sequences are apparent. Higher order inversion methods struggle to fit small late-time conductors and the 1D approach, although identifying a deep conductor (Valen), tend to push it to a much greater depth than suggested by ground and borehole EM.

Acknowledgements

We acknowledge the support of CSIRO's Deep Earth Imaging Future Science Platform in facilitating the conduct of this work.

References

Auken, E, Christiansen, A, Kirkegaard, C, Fiandaca, G, Schamper, C, Behroozmand, A, Binley, A, Nielsen, E, Effersø, F, Christensen, N, Sørensen, K, Foged, N, and Vignoli, G, 2015, An overview of a highly versatile forward and stable inverse algorithm for airborne, ground-based and borehole electromagnetic and electric data: Exploration Geophysics,. doi:10.1071/EG13097

Brodie R. (2012) AEM Inversion of VTEM Data from a Resistive Terrain, ASEG Extended Abstracts, 2012:1, 1-4, DOI: 10.1071/ASEG2012ab096

Christiansen, A. V., and E. Auken, (2012), A global measure for depth of investigation: Geophysics, 77, no. 4, WB171–WB177, doi: 10.1190/geo2011-0393.1.

Christensen, N., and Lawrie, K., 2012. Resolution analyses for selecting an appropriate airborne electromagnetic (AEM) system, Exploration Geophysics, 43, 213–227

Haber, E. Holtham, E., Granek, J., Marchant, D., Oldenburg, D., Schwarzbach, C. and Shekhtman, R., 2012. An adaptive mesh method for electromagnetic inverse problems. SEG Technical Program Expanded Abstracts 2012: pp. 1-6. doi: 10.1190/segam2012-0828.1

Lne, R., Green, A., Golding, C., Owers, M., Pik, P., Plunkett, C., Sattel, D., and Thorn, B., (2000), An example of 3D conductivity mapping using the TEMPEST airborne electromagnetic system: Exploration Geophysics, 31, 162-172.

Leggatt, P.B., Klinkert, P.S. and Hage, T.B., 2000, The Spectrem airborne electromagnetic system—further developments: Geophysics, 65(6), 1976-1982.

Ley-Cooper, A. Y., Viezzoli, A., Guillemoteau, J., Vignoli, G. Macnae, J., Cox, L. and Munday, T., (2015). Airborne electromagnetic modelling options and their consequences in target definition: Exploration Geophysics, 46,74–84, doi:10.1071/EG14045

Oldenburg, D. W., E. Haber, and R. Shekhtman, (2013), Three dimensional inversion of multisource time domain electromagnetic data: Geophysics, 78, no. 1, E47–E57, doi: 10.1190/geo2012-0131.1.

Paterson, R., Silic, J., and FitzGerald, D., 2016. Improved Structural Mapping and Conductive Targeting Delivered by a New 2.5D AEM Inversion Solver. ASEG Extended Abstracts (2016), 1-8.

https://doi.org/10.1071/ASEG2016ab232

Sattel, D., 2005, Inverting airborne electromagnetic (AEM) data with Zohdy's method. Geophysics 70 (4), G77-G85.

Schwarzbach, C., Holtham, E. and Haber, E., 2013. 3D inversion of time domain electromagnetic data. ASEG Extended Abstracts 2013, 1-4. https://doi.org/10.1071/ASEG2013ab064

Silic, J., Paterson, R., FitzGerald. D. and Archer, T., (2015). Comparing 1D and 2.5D AEM inversions in 3D geological mapping using a new inversion solver. 14th International, Congress of the Brazilian Geophysical Society, Extended AbstractsSilic

Viezzoli A. and Selfe, G., (2018) Comparing responses from different AEM systems and derived models at the Sunnyside nickel project, Botswana, ASEG Extended Abstracts, 2018:1, 1-8, DOI: 10.1071/ASEG2018abW8_2E

Viezzoli, A., A. V. Christiansen, E. Auken, and K. Sorensen, (2008), Quasi-3D modeling of airborne TEM data by spatially constrained inversion: Geophysics, 73, no. 3, F105–F113, doi: 10.1190/1.2895521

Wilson, G.A., Raiche, A.P. and Sugeng, F., (2006). 2.5D inversion of airborne electromagnetic data. Exploration Geophysics, 37, 363-371.

Witherly, K., R. Irvine, and E.B. Morrison (2004) The Geotech VTEM time domain electromagnetic system. 74TH Annual Meeting and International Exposition, SEG, Expanded Abstracts, p. 1217–1221

Woodhouse AJ and Gum JC (2003) Musgrave Province — geological summary and exploration history, Report

Book 2003/00021. Department of Primary Industries and Resources South Australia, Adelaide.

Yang, D., Oldenburg, D. and Haber, E., 2014, 3-D inversion of airborne electromagnetic data parallelized and accelerated by local mesh and adaptive soundings, Geophys. J. Int., 196 (3), 1492-1507

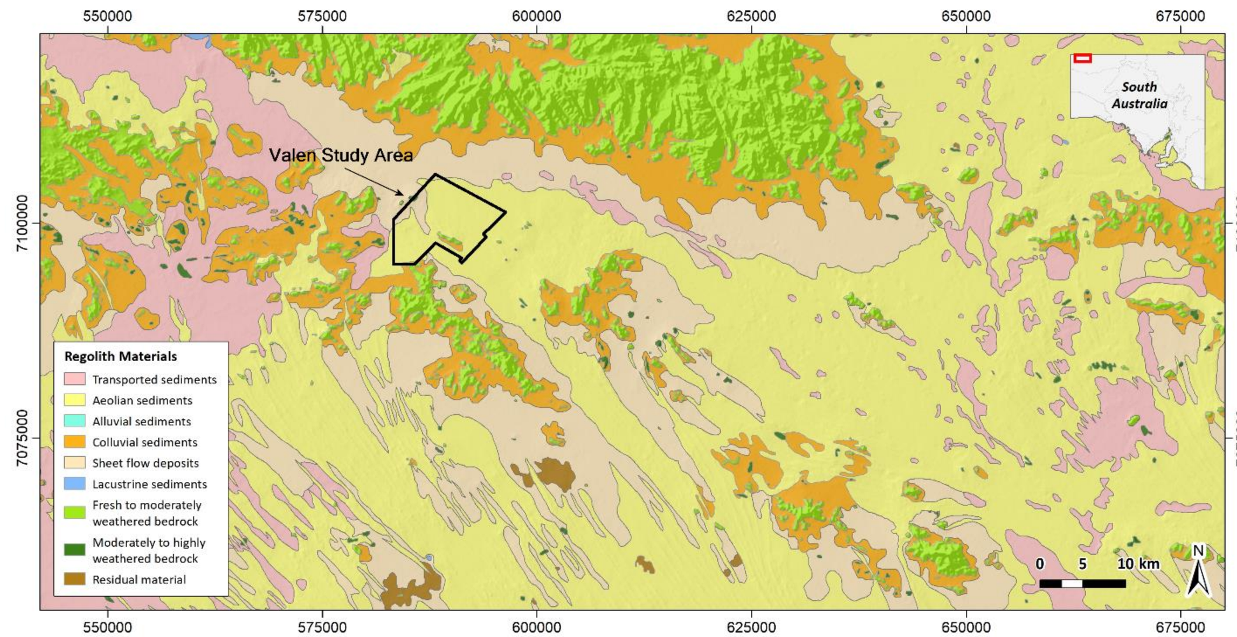

Figure 1: Location of the Valen study area in NW South Australia. The area of interest is delimited by the black polygon overlain on a regolith materials map.

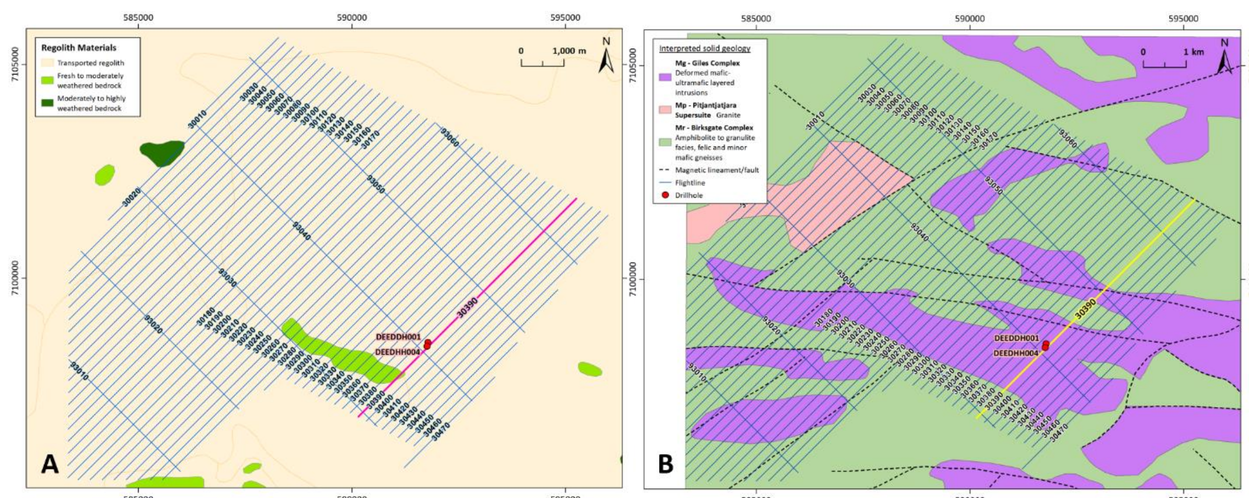

Figure 2: Finer-scale regolith materials (A) and solid geology (B) map for the Valen study area. The maps are overlain with flightlines from a VTEM AEM survey. The section line (Line 30390) of interest in this study is shown in red (over the regolith map) and yellow (over the basement geology map). Drillhole locations that intersected the Valen prospect (red dots) are near-coincident to this line and are plotted on the map. Line spacing of the VTEM survey plotted on the map is 200m.

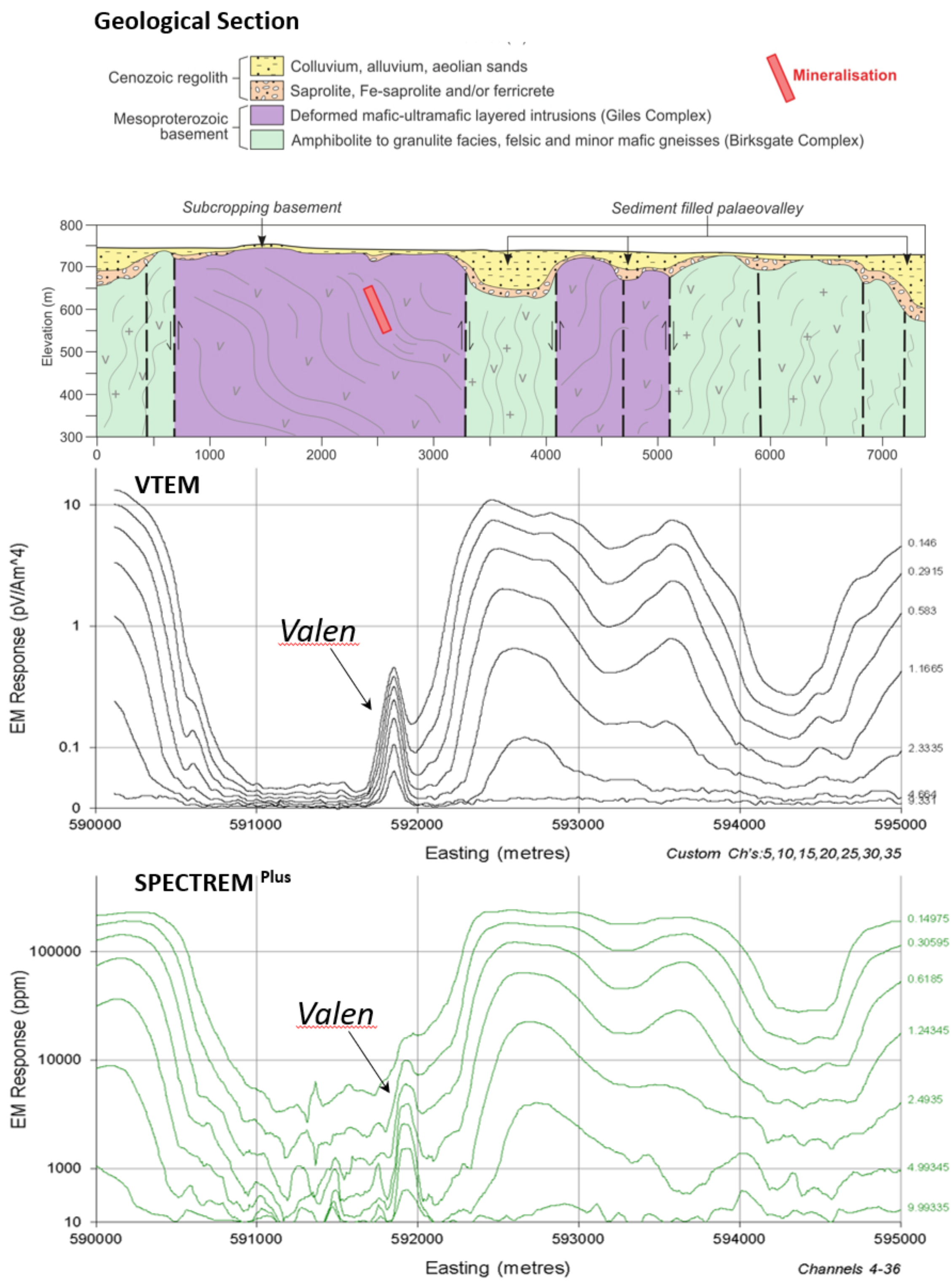

Figure 3: Interpreted geological section (from surface observations, geophysical data interpretation, and drilling) for the line shown in yellow and red in Figure 2. This is coincident with flightlines for the four AEM systems examined in this study. The approximate location of the Valen prospect is shown by a red plate (defined from modelling surface TDEM and borehole DHEM data – see Figure 4). Corresponding amplitude responses for late time gates for two of the four AEM systems (VTEM and SPECTREM PLUS) are shown beneath the geological section. A discrete, late time conductive response (Valen) is noted in both systems. High amplitude responses associated with palaeovalley fill are also apparent.

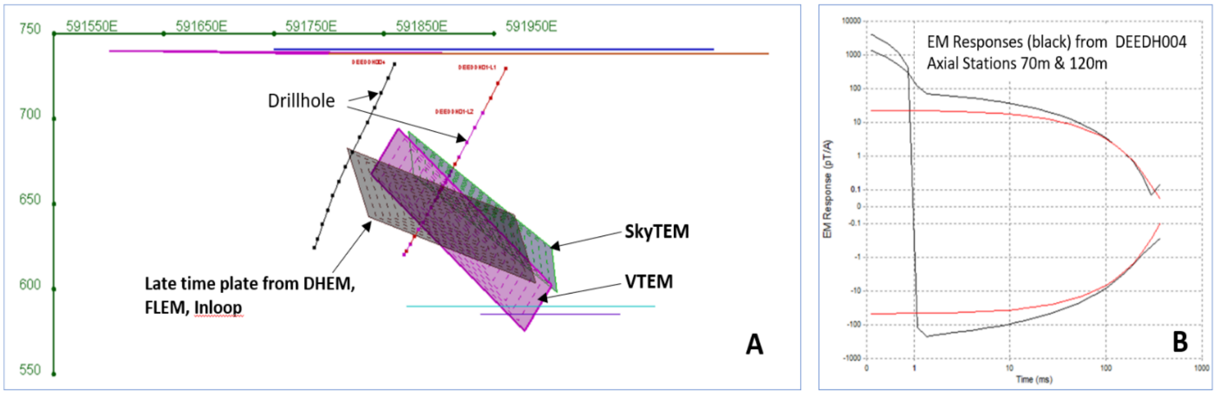

Figure 4: Plate models for the Valen prospect (A) showing VTEM (purple), SkyTEM (grey/green) and combined Surface TDEM and DHEM models (grey). View is from SW to NE. The orientation of the two drill holes (DEEDH001 (pink trace) and DEEDH004 (black trace) is also shown. Plate modelling was undertaken using MAXWELL. Modelling of the ground data places the top of the plate approximately 100m below the ground surface. Measured DHEM responses from axial stations at 70 and 120m below the surface are shown in B. These are coincident with a zone of mineralisation in the drillhole. The responses exhibit well defined exponential decays.

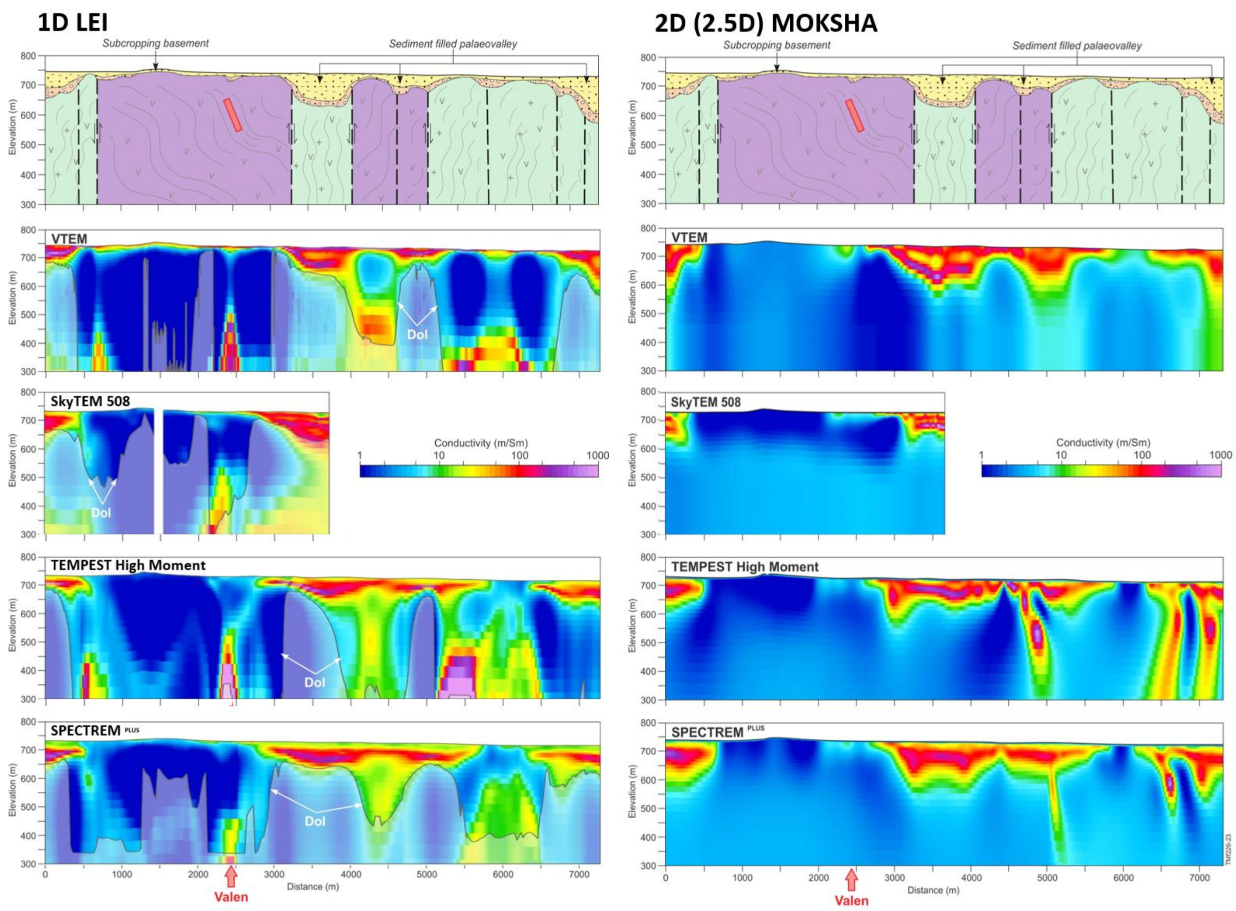

Figure 5: 1D smooth model (AarhusInv) inversion results (Left column)- presented as conductivity-depth sections for data acquired from coincident lines from different systems across the Valen prospect. The right column shows inversion results from inversion using the 2D (2.5D) Moksha code for the systems considered. Line orientation is shown in Figure 2 and the sections are oriented with south on the left and north on the right. The location of the Valen conductor along the section is indicated at the bottom of the stitched sections.

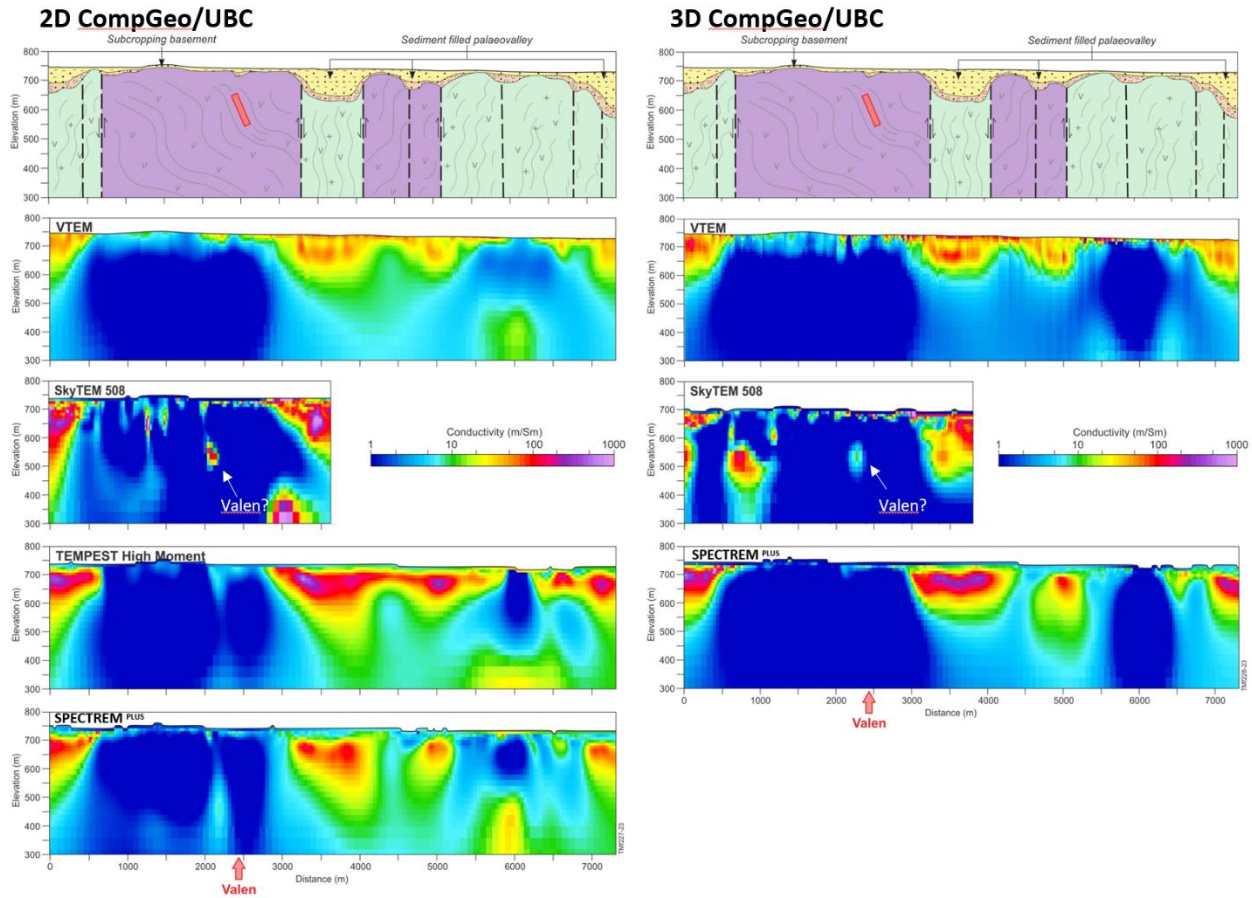

Figure 6: 2D smooth model inversion results for different AEM systems (Left column) generated form the application of the CompGeo/UBC codes, where individual lines were run in “2D-mode" where additional regularization was applied in the cross-line direction, while still modelling the full 3D physics. The right column shows model results from inversion using an “all at once” (where three adjacent lines were modelled with 3D physics. Line orientation is shown in Figure 2 and the sections are oriented with south on the left and north on the right. The location of the Valen conductor along the section is indicated at the bottom of the stitched sections. Suggested location of the Valen conductor is indicated in the SkyTEM data for both inversion approaches.

Geophysical signatures in high enthalpy geothermal exploration using 3D MT surveys

José Antonio Rodríguez, Quantec Geoscience Limited*
Mehran Gharibi, Quantec Geoscience Limited

Summary

The typical geological setting of high enthalpy geothermal systems constitutes a certain pattern of mineral alteration. This alteration pattern, as well as high enthalpy fluids and reservoirs, contributes to large contrasts in electric resistivity of the subsurface that can be identified by electric or electromagnetic geophysical methods. Due to the depths at which high-temperature geothermal reservoirs are situated and the complexity of subsurface structures, the magnetotelluric (MT) method has become the primary technique used for geothermal detection and exploration.

High enthalpy geothermal systems are usually found near active or recently extinct volcanoes. The geology in these settings is complex, and an accurate mapping of the geothermal system and reservoir dictates a 3D survey and treatment. MT data are intrinsically 3D and the method is able to map the complex resistivity distributions in the subsurface when the survey covers the entire geothermal system.

This paper discusses the architecture of high enthalpy geothermal reservoirs and their expected resistivity structures and signatures. A field survey example from a large geothermal system is presented and discussed in conjunction with the expected conceptual model. The results highlight the sensitivity and ability of MT surveys to map and discriminate elements of the geothermal system, including the potential feeding zone. The 3D MT model identifies two zones that may correspond to low-resistivity smectite layers, and so may correspond to two separate geothermal reservoirs. The geometric shapes of the low resistivity anomalies have the appearance of an outflow system, which correlates well with the location and chemistry of fumaroles and hot springs on the surface. The results demonstrate that 3D modeling is an effective way to resolve and position the main features of high enthalpy geothermal systems, and a key factor in the creation of realistic representations of the subsurface.

Introduction

A geothermal resource is usually characterized as composed by a reservoir in fluid phase, geologically situated in altered or structurally deformed host rocks, and heated by some volcanic or magmatic source.

High enthalpy reservoirs (T>~215°C) form a clay cap that traps the hot, buoyant fluid and keeps it from escaping to the surface. The clay cap over the saline reservoir at depths typically > 1 km form a distinct pattern of electrical resistivity that makes magnetotellurics (MT) the preferred method for geophysical exploration.

The geologic settings of commercially viable high enthalpy geothermal projects are usually around volcanic areas with great lateral variations in mineralization and rock types, which require 3D data acquisition and modeling. 1D and 2D models cannot adequately capture the complexities of these geothermal systems.

Schematic of resistivity signature of a high temperature geothermal reservoir

The upflowing hot, buoyant geothermal fluid will form a smectite layer that acts as a cap for the reservoir (Figure 1). The clay layer will extend for some distance as the fluid flows out horizontally away from the heat source.

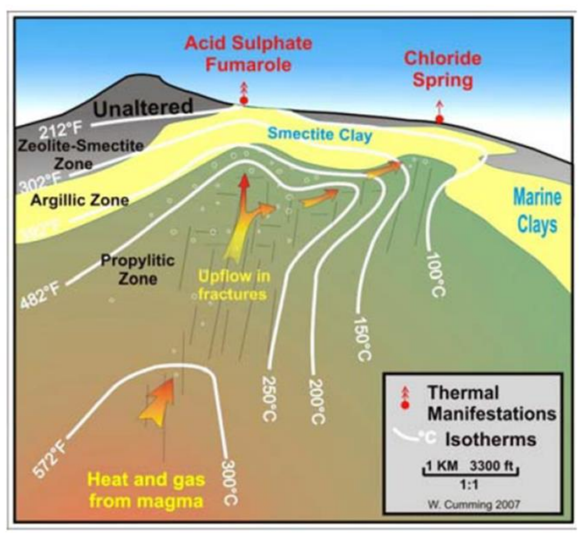

Figure 1. Diagram of a typical high-temperature geothermal reservoir (Cumming, 2009).

At the surface above the clay cap, there will often be acidic fumaroles formed that will contain geothermometer indications of the temperature of the reservoir below the smectite layer. Further out in the outflow, also at the surface, hot water springs will often form after the fluid has degassed.

The smectite layer shows very low resistivity values in the single digits (Figure 2). Below that, the reservoir will show resistivity values in the low double digits, due to the combination of the saline aquifer and a rock matrix rich in silica and epidote. This characteristic resistivity distribution, below a pattern of fumaroles and hot springs, is a clear indicator of the existence of a high-temperature geothermal reservoir.

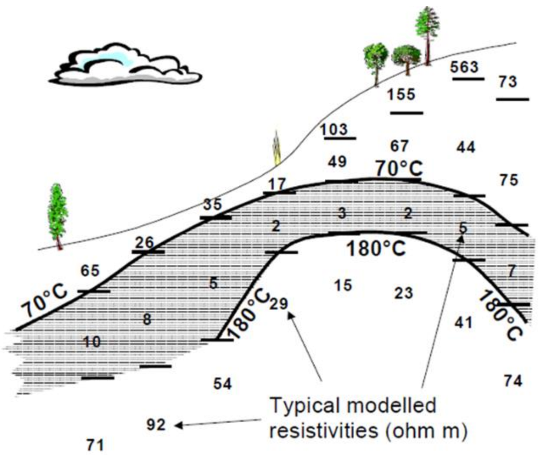

Figure 2. Example of modeled resistivity values, in ohm-m (Anderson et al, 2000).

Fantale geothermal system, Ethiopia

A magnetotelluric study of the Fantale geothermal system was carried out by Quantec Geoscience Ltd. on behalf of Cluff Geothermal Ltd. (Figure 3). A total of 246 full tensor broadband MT sites was collected over an area of approximately 14 x 20 km (Figure 4).

Figure 3. Google Earth image of Fantale volcano.

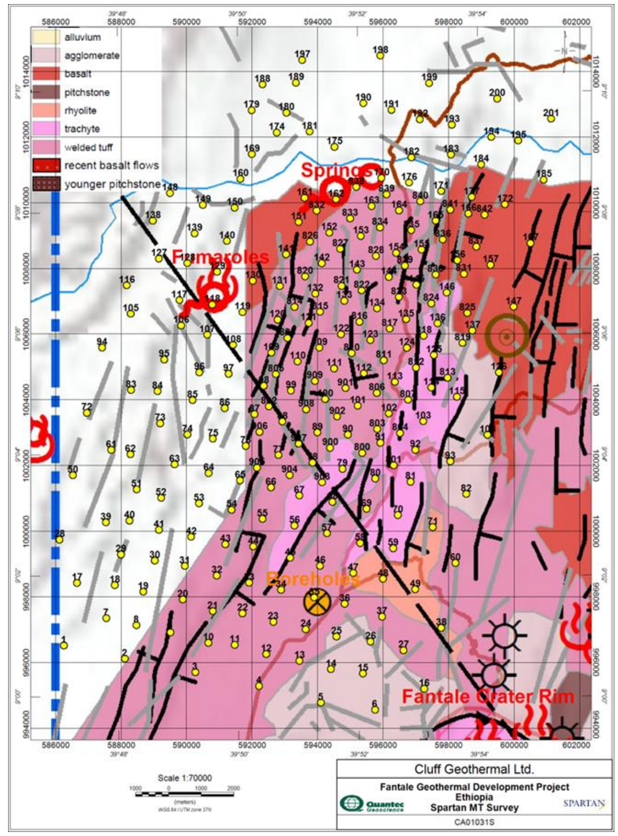

Figure 4. MT site locations shown over a schematic geologic map (Gharibi et al, 2019).

The area shows a graben structure north of the volcanic edifice, with main faulting approximately in a N-S direction. There are high gas content fumaroles inside the crater, acidic fumaroles to the NNW of the volcano, and hot springs to the north, in the typical pattern that is indicative of an underlying high temperature geothermal system.

1D models of selected sites indicate the possible presence of more than one aquifer (Figure 5). The low resistivity layers at ~500m and 1300m depths could correspond to clay caps, and the aquifers would underlie the clay layers, respectively.

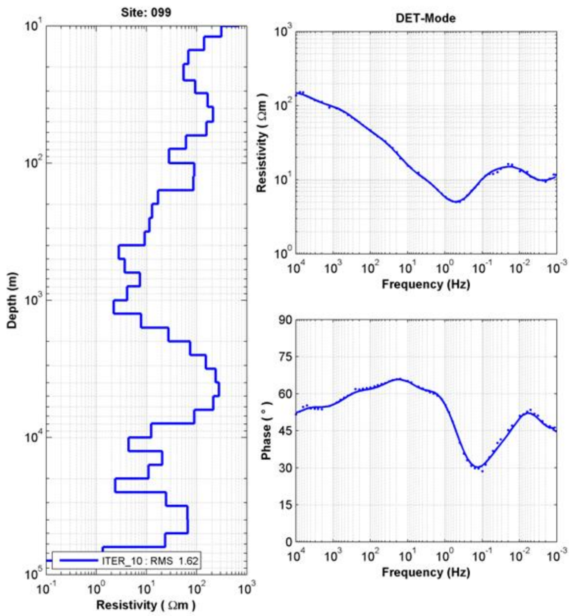

Figure 5. 1D model of sample MT site, showing low resistivity zones at ~500m and ~1300m depths. (Gharibi et al, 2019).

A 3D model was generated from the MT data, and the horizontal plan maps show a low resistivity feature underlain by a moderate resistivity layer that align with the locations of the fumaroles and hot springs.

The plan maps at 1600m and 2000m elevations (Figure 6 and Figure 7) appear to be a true representation of the classic conceptual model of a high temperature geothermal system shown in Figure .

Additionally, in survey acquisitions that include vertical magnetic (i.e. Hz) component, the induction vector can be calculated at each frequency. Each induction vector is calculated independently, and so constitutes independent confirmation of the presence of the conductor. As can be clearly seen in Figure 8, the conductor observed in Figure 6 is confirmed by induction vector from all sites, and is likely to correspond to a conductive clay layer.

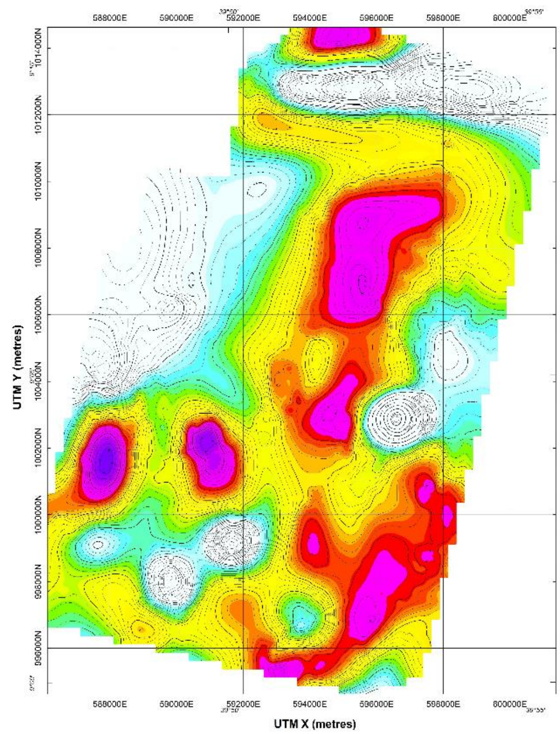

Figure 6. Plan map of 3D MT resistivity at constant 1600m elevation, Fantale geothermal prospect (Gharibi, et al, 2019).

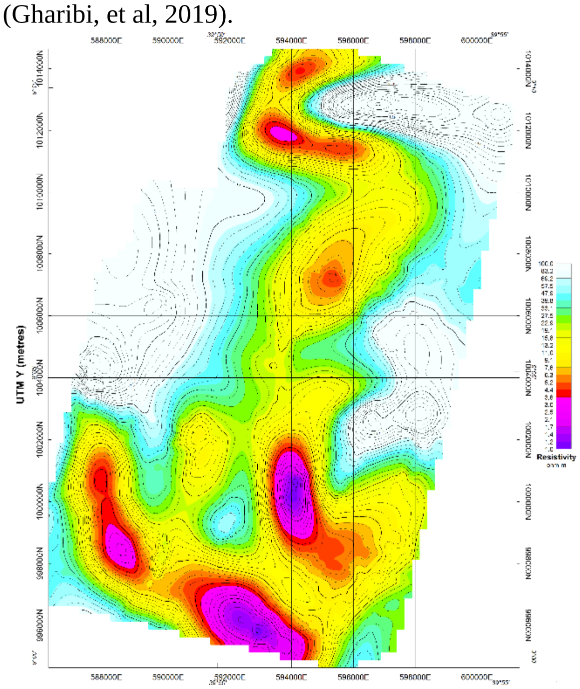

Figure 7. Plan map of 3D MT resistivity at constant 2000m elevation, Fantale geothermal prospect (Gharibi, et al, 2019).

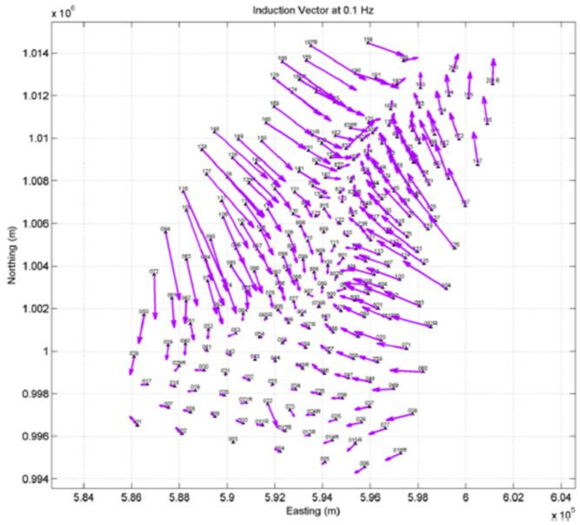

Figure 8. Induction vector plot at 0.1 Hz of Fantale MT survey (Gharibi, et al, 2019).

In order to obtain a model that clearly allows a visualization of a geothermal system, a 3D inversion of the MT data that takes topography into account is essential. Figure 9 shows the 3D model cut at low resistivity value. The model correctly positions the features in space and resembles a visualization of the conceptual model of the volcanic and geothermal system.

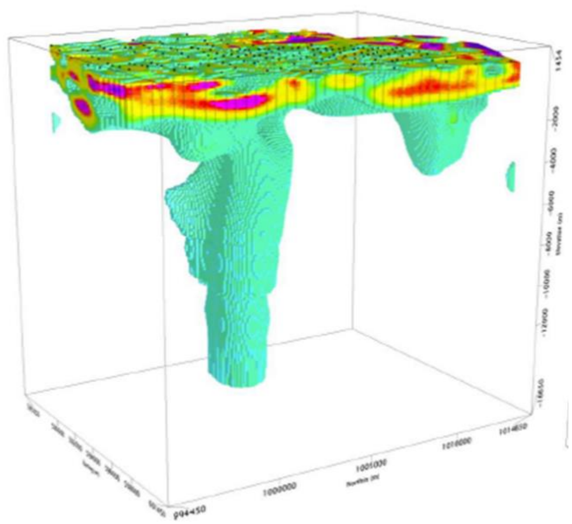

Figure 9. 3D view of 3D models.

Conclusions

The classical conceptual resistivity pattern for a geothermal system is clearly observable in the 3D MT model for the Fantale volcanic high temperature geothermal prospect. 3D modeling is required to accurately resolve the resistivity features of the subsurface.

Acknowledgements

Thanks to Cluff Geothermal Ltd. for allowing publication and discussion of this magnetotelluric study.

References

Anderson, Errol, Crosby, Daryl, and Ussher, Greg, 2000. "Bulls-Eye! – Simple Resistivity Imaging to Reliably Locate the Geothermal Reservoir", Proceedings of the World Geothermal Congress, Japan, p.909-914.

Cumming, William, 2009. "Geothermal Resource Conceptual Models Using Surface Exploration Data", Proceedings of the Thirty-Fourth Workshop on Geothermal Reservoir Engineering, Stanford University, p.322-327.

Gharibi, Mehran, Kuhn, Oliver, and Eliott, Thomas P., 2019. "Deep Resistivity Imaging of Geothermal System Using Magnetotelluric Surveys, A Case Study", GRC Transactions, Vol. 43, p.784-793.

Hersir, Gylfi Páll, Árnason, Knútur, and Vilhjálmsson, Arnar Már, 2013. "3D inversion of magnetotelluric (MT) resistivity data from Krýsuvík high temperature geothermal area in SW Iceland", Proceedings of the Thirty-Eighth Workshop on Geothermal Reservoir Engineering, Stanford University, p.1253-1266.

IGA Service GmbH, 2014. "Best Practices Guide to Geothermal Exploration", prepared for and managed by International Finance Corporation, 194 p.

Recovering exploration models patterns with airborne total field passive electromagnetics

Alexander Prikhodko, Expert Geophysics Limited*

Summary

The latest development in the airborne natural (passive) electromagnetic field method, the MobileMT system, was designed to measure three orthogonal geometrical components forming total field data. The technical feature makes the system sensitive to any direction of geoelectrical boundaries and, ultimately, capable of recovering complex geology of hydrothermal-magmatic systems followed by different types of mineralization. Other advantages inherent to the natural electromagnetic fields are the significant depth of investigation and response capabilities in the expanded resistivity range. These advantages are also crucial for geoelectrical mapping and recovering more comprehensive pictures of exploration models. Case histories from around the world illustrate the airborne natural electromagnetic field technology capabilities in recovering geological models and their specific patterns. The examples include unconformity uranium mineralization, main types of gold-bearing structures (orogenic and epithermal types), porphyry style of mineralization, and ferromanganese and polymetallic ores formed in a continental rift valley.

Introduction

The capability of recovering mineralization systems' morphological patterns is an essential factor of a geophysical method or a geophysical parameters measurement system selection and its efficient application. MobileMT airborne electromagnetic system (Prikhodko et al., 2022) has specific technical solutions that make the system universal for the exploration of different commodities in a wide range of geological terrains. The system is capable of imaging subsurface geology in a wide depth range with high resistivity resolution in different ranges of the physical property allowing detection of mineralization controlling structures and their specific patterns. Field case studies and examples are provided from over the world over known mineral deposits, occurrences and mineralization controlling structures compared with conceptual geological models.

Method

The main advantages of the MobileMT airborne electromagnetic technology include its wide range of depth of investigation (from the near-surface up to the first kilometres); sensitivity to any direction of geoelectrical boundaries, from horizontal to vertical; sensitivity to differentiations in a broad range of resistivities, from superconductors to tens of thousands of ohm-m; high spatial and in-depth resolution. In addition, output MobileMT data is independent of relief in contrast to tipper type of data and much less dependent on terrain clearance than systems with controlled transmitting field sources.
There are technical solutions behind these capabilities and advantages:

- The technology exploits electromagnetic wave, which is naturally transmitted under the earth's surface;
- variations of the magnetic field are measured by three orthogonal coils supported by a sophisticated suspension system in a towed-bird receiver;
- two independent pairs of grounded lines measure variations of the electric field (stationary base station) to get denoised and bias-free data, as described by Labson et al. (1985);
- 3+ orders of the frequency data measurement range (22/26-21,000 Hz) divided by 30 windows;
- 74 kHz sampling rate of data acquisition.

All resistivity sections in the paper are from non-constrained inversions of MobileMT data executed with the adopted MARE2DEM code software (Key, 2016).

Field examples

The following examples present the results of MobileMT surveys operated by Expert Geophysics Limited (EGL), and by EGL in collaboration with MPX Geophysics and Qazaq Geophysics. The cases were taken from surveys integrated into exploration programs in Canada, Central Asia, and Chile.

The MobileMT depth-resistivity images present field data over known deposits or developing highly prospective areas and following by conceptual geological models of corresponded types of mineralization and mineral deposits.

Athabasca basin (uranium)

Two types of unconformity related uranium mineralization are presented (Figure) – the "ingress style" (Jefferson et al., 2007) basement-hosted, fracture controlled or vein mineralization below the unconformity (Shadow project, Figure 2) and the "egress style", in the basement and above the unconformity (from the region of McArthur River Mine and Millennium deposit, Figure 3). The field examples demonstrate that the airborne system resolves the geological targets in a wide depth range, beginning from near surface (Figure 2) and far below the unconformity contact (U/C in Figure 3).

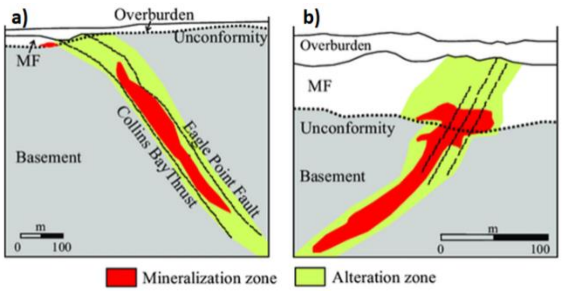

Figure 1. Geological models of basement hosted “ingress style” uranium deposits (a) and at and below the unconformity, “egress style” (b), (From Li et al., 2016)

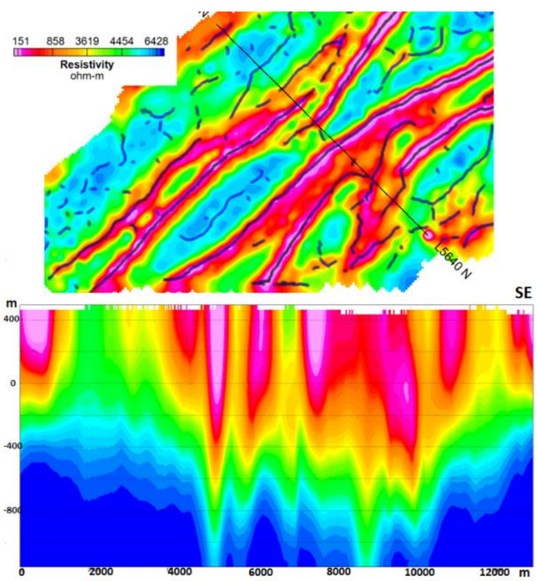

Figure 2. MobileMT resistivity map (top) and section (bottom) over a central part of the Shadow project (basement hosted mineralization, corresponded to Figure a model)

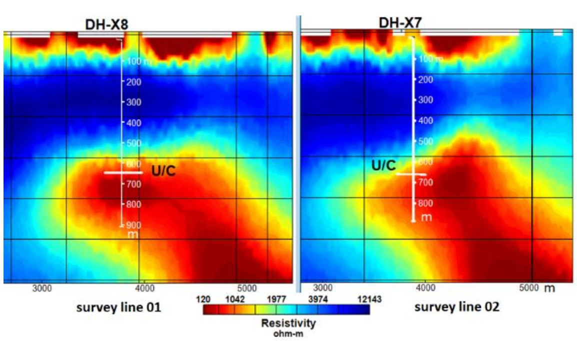

Figure 3. MobileMT resistivity sections along two survey lines with confirmed by drilling unconformity contact (U/C) at 650 m depth and related mineralization in and above the basement (geological model Figure b).

Epithermal and porphyry deposits

Stockwork-style and veins of copper, copper-gold, and copper-molybdenum deposits are widespread along the Kendyktas Ridge (Central Asian Ordovician magmatic arc) in south-central Kazakhstan (Zientek et al., 2014). Chatyrkul (544,200 t copper), Jaisan, Ungurli, Aktasty are examples of typical deposits in the region. The ore bodies are located over subalkaline intrusives of the Paleozoic age (Devonian) which petrophysically are more resistive than the overlaying late Ordovician granites. Position of the mineralization, according to MobileMT survey results, are controlled by vertical pipe-similar electrically resistive “vents” (Figure 4). The petrophysical image recovered from the MobileMT data is amazingly similar to the conceptual geological model of magmatic-hydrothermal systems producing porphyry and related epithermal ore deposits (Figure 5).

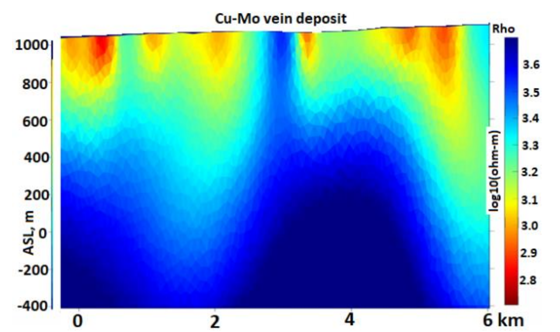

Figure 4. Typical MobileMT resistivity section over a cupper- gold-molybdenum deposit in the Kendyktas Ridge, Kazakhstan

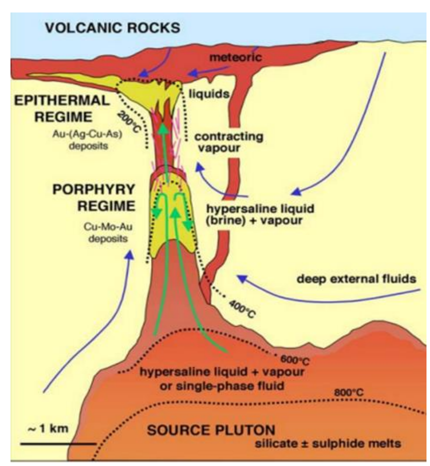

Figure 5. Schematic cross section of a magmatic–hydrothermal system (after Heinrich, 2005)

Another example of MobileMT resistivity mapping results matching the morphology of the schematic geological model is the epithermal silver-gold deposit Dukat (17k t of silver) in northeast Russia (Kordi et al., 2021). In this case, deep seated intrusive dome structures and related to them feeding channels arising to the surface and controlling the mineralization, are more conductive in comparison with host rocks (volcanic rocks in this case) (Figure 6).

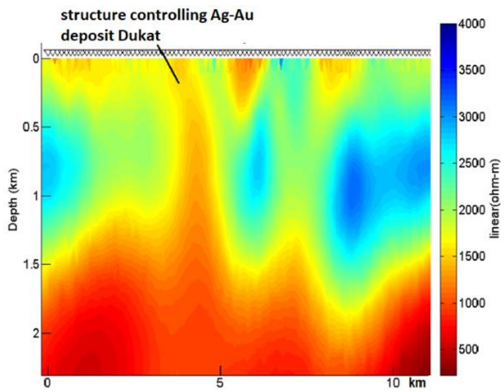

Figure 6. MobileMT resistivity section over the Dukat ore field (northeast Russia)

The schematic model in Figure 7 represents a calc-alkalic porphyry system with following alteration zones what typical for Andean porphyry copper systems.

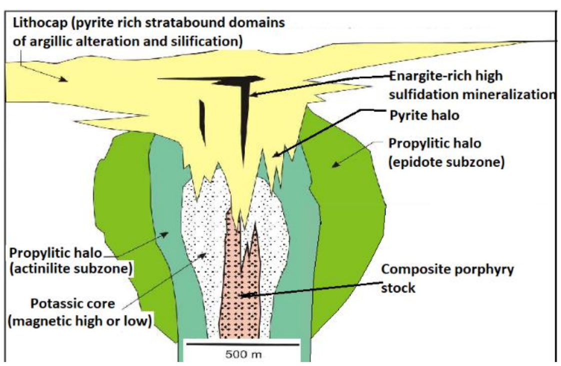

Figure 7. Schematic illustration of alteration zoning and overprinting relationships in a calc-alkalic porphyry system (after Holliday et al., 2007).

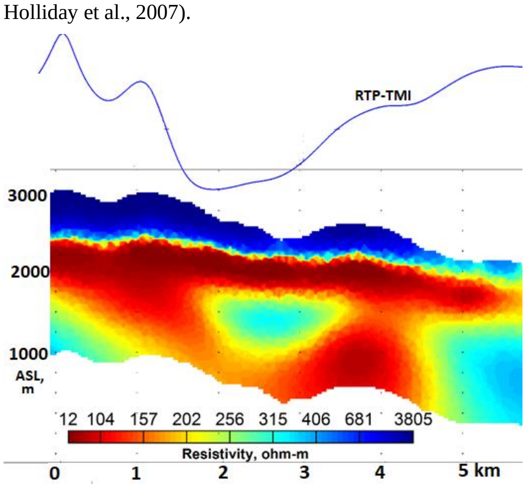

Figure 8. MobileMT resistivity section over a porphyry system in Northern Chile with the magnetic field profile

Figure 8 shows a MobileMT resistivity section along a line crossing an estimated porphyry system in northern Chile. The image reflects the conductive lithocap, propylitic halo and comparatively resistive potassic halo. The resistive layer over the conductive lithocap is a geologically mapped gravel.

Orogenic gold

The Tien Shan structure hosts a number of giant gold deposits including Kumtor, Muruntau, Zharmitan, Kokpetas, Jilau and others (Yakobchuk, 2005). The orogenic gold of the Kumtor deposit is on the mesozonal intrusive-related mineralization level at paleodepths on the order of 5 km (Figure 9) and occurs where the Vendian sediments have been hydrothermally altered and mineralized. The resistivity section (Figure 10) shows a link between the zone containing altered metasediments (top conductive layer) and a dome-like, deep-seated conductive structure which is interpreted as a reduced intrusion, or an alteration zone above it.

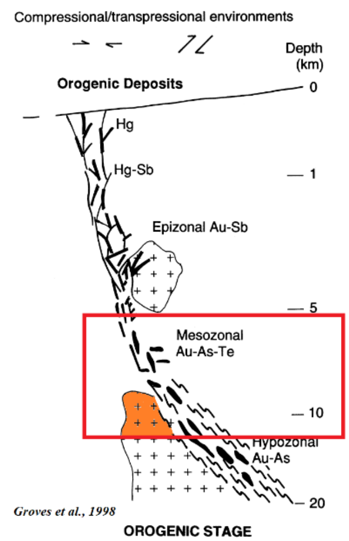

Figure 9. Conceptual diagram of a mineral system model for orogenic-gold deposits (after Groves et al., 1998) with the outlined paleo level of the Kumtor deposit

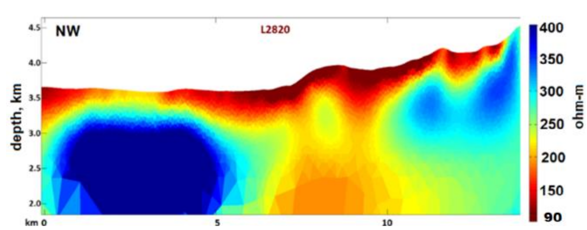

Figure 10 – MobileMT resistivity section crossing a structure controlling the Kumtor deposit mineralization.

Ferromanganese and polymetallic ores in a continental rift valley

Type of mineralization: stratiform/lens Fe-Mg and superimposed Cu-Ba on the comparatively near surface contact between volcano-sediment layers under alluvium (Figure 11). There is a preferable stratigraphic horizon of the ore bedding rocks which is shown in the resistivity section between dush lines 1 and 2 (Figure 12). The MobileMT survey results recover not only the comparatively near surface beds with mineralization but a buried magmatic source of hydrothermal fluids with feeding channels (Figure 12).

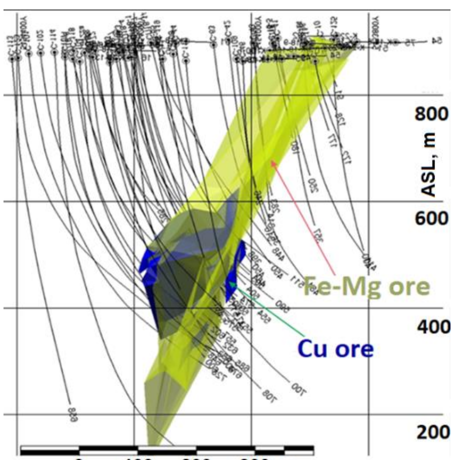

Figure 11. 3D projection of a Fe-Mg-Cu ore body. East Atabay, Central Kazakhstan.

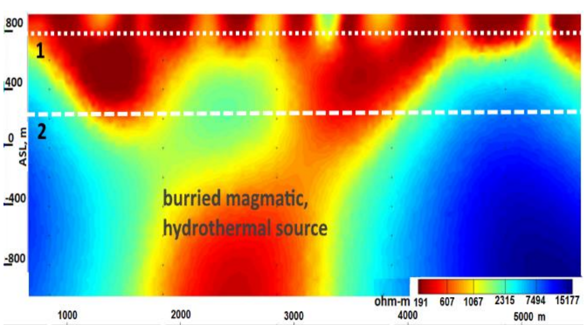

Figure 12. MobileMT resistivity section over a line on the East Atabay area. 1- the line of alluvium sediments with salt licks 2- bottom level of permeable beds with ore

Conclusions

As the field examples of different types of mineralization systems demonstrate, the extensive depth range resistivity imaging and its analysis/ interpretation guided by exploration models is a powerful tool for exploring geologically prospective districts. Sensitivity to any direction of geoelectrical boundaries in the broad resistivity range makes the MobileMT technology efficient in exploration of different types of mineralization in complex geologic settings.

Acknowledgments

The case studies were developed based on Expert Geophysics Limited MobileMT surveys including surveys under support and participation of Qazaq Geophysics and MPX Geophysics.

References

Groves D.I., Goldfarb, R.J., Genre-Mariam, M., Hagemann, S.G., and Robert, F. (1998). Orogenic gold deposits : A proposed classification in the context of their crustal distribution and relationships to other gold deposit types: Ore Geology Reviews, 13, 7-27.

Heinrich, C.A. (2005). The physical and chemical evolution of low-salinity magmatic fluids at the porphyry to epithermal transition: a thermodynamic study. Mineralium Deposita, 39, 864–889.

Holliday, J. R., Cooke, D. R. (2007). Advances in Geological Models and Exploration Methods for Copper ± Gold Porphyry Deposits. In "Proceedings of Exploration 07: Fifth Decennial International Conference on Mineral Exploration" edited by B. Milkereit, 791-809.

Key, K., (2016). MARE2DEM: a 2-D inversion code for controlled-source electromagnetic and magnetotelluric data. Geophysical Journal International, 207(1), 571–588.

Kordi, P., Prikhodko, A., Bagrianski, A., Trushin, S., (2021). Expanding the reserve base of operating mines: Insights from an airborne MobileMT survey in the Omsukchan depression, Russian Far East. 3rd AEGC: Geosciencies for sustainable World – Brisbane, Australia. Expanded Abstracts. 1-4.

Labson, V.F.; Becker, A.; Morrison, H.F.; Conti, U. (1985). Geophysical Exploration with Audiofrequency Natural Magnetic Fields. Geophysics, 50, 656–664.

Li, Z., Chi, G., & Bethune, K. M. (2016). The effects of basement faults on thermal convection and implications for the formation of unconformity-related uranium deposits in the Athabasca Basin, Canada. *Geofluids*, *16*(4), 729-751.

Prikhodko, A., Bagrianski, A., Kuzmin, P., Sirohey, A., (2022). Natural field airborne electromagnetics – history of development and current exploration capabilities. Minerals, 12, 583, 1-16.

Jefferson, C. W., Thomas, D., Quirt, D., Mwenifumbo, C. J., and Brisbin, D. (2007). Empirical Models for Canadian Unconformity-Associated Uranium Deposits. “Ore deposits and exploration technology” in “Proceedings of Exploration 07: Fifth Decennial International Conference on Mineral Exploration”, 741-769.

Yakubchuk A.S., Shatov V.V., Kirwin D. et al. (2005). Gold and base metal metallogeny of the Central Asian Orogenic supercollage. Society of Economic Geologists, Inc. Economic Geology, 100th, Anniversary Volume, 1035-1068.

Zientek, M., Hammarstrom, J., Johnson, K. (2014). Porphyry Copper Assessment of Western Central Asia. USGS scientific investigations report 2010-5090-N.

Airborne GPR Survey for Bathymetry, Muskrat Falls, Labrador (1998)

William J. Scott, GeoScott Exploration Consultants Inc. (Acquired by Abitibi Geophysics in 2006, now Abitibi Atlantic.)

Summary

When design of the Muskrat Falls Power Station was commenced, it was important to determine the bedrock elevation in the pool between upper and lower falls. A heli-borne GPR survey was conducted over the area. 141 lines were flown across the area at 10 m intervals. Water depths of up to 15 m were encountered, and a map of bedrock elevations was produced.

Introduction

Muskrat Falls, on the Churchill River, was one of the two possible areas considered for development of hydro power in Labrador. NALCOR Energy was established by the NL Government as the organization responsible for the project. Final design began in the mid-1990s. The consortium SNC-AGRA was established to provide all the initial geotechnical information on which the design would be based. GeoScott was contracted to provide bathymetric information by means of an airborne GPR survey.

The survey was carried out August of 1998. At the time, GeoScott was unable to obtain release of the data in order to present a paper on the survey. However, recently the survey report was published on the NALCOR website, thus allowing the preparation of this talk.

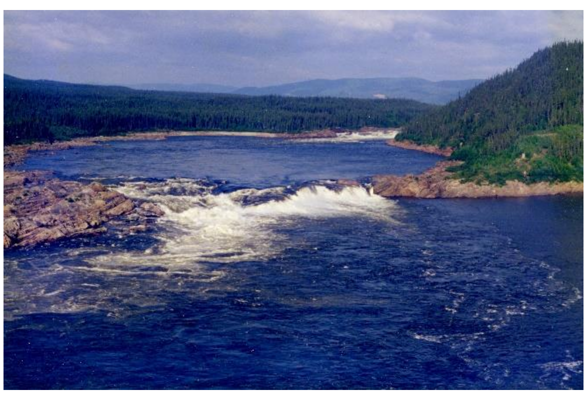

Figure 1: Muskrat Falls viewed from the east in 1998.

Survey Approach

Initial consideration was given (very briefly) to a bathymetric survey performed from a boat, but clearly this approach was far too dangerous. GeoScott was retained to carry out the survey with Ground Penetrating Radar (GPR) mounted under a helicopter.

We used a RAMAC/GPR impulse radar, made by Malå Geoscience in Malå, Sweden, and provided by Terraplus Inc. in Toronto. The centre frequency of the system was 200 MHz. The helicopter was a Robinson R44 supplied by Héli-Transport, Sept Isles, QC.

Navigation was accomplished with a Trimble Series 4000 global positioning system operated in real-time differential mode, with the base station on a control point supplied by SNC-AGRA. The moving antenna was mounted on the tail boom of the helicopter, and the radio link antenna on one of the helicopter landing skids. With one-second updates, horizontal and vertical precisions were about 3 cm.

One hundred and forty-one lines were flown across the river at ten metre intervals. In addition, several tie lines were flown along the river from below the lower falls to above the upper falls.

At first, it was planned to fly with the antennae five meters above the water surface, but initial trials found that multiple reflections from the water surface obscured any deeper reflectors. The survey was flown with a nominal clearance of two metres or less from the water. The flying speed was about 4 knots, to allow adequate stacking of the radar signals.

Two laptops were set up in the helicopter. One was to monitor and record the GPR profiles, and the other to run the navigation program. We found that the pilot was too busy flying to be able to look at the navigation screen, so the radar operator had to provide a running guidance "Left a bit, right a bit, on line now, …..".
Position data were recorded every second. GPR traces were recorded at 0.2 second intervals, so that every fifth trace was at a known point. The tie between navigation and GPR recording was achieved by synchronising the two computer clocks.

The survey was flown with the doors removed from the helicopter. Both the pilot and the operator wore life jackets, but we agreed that this would facilitate finding the bodies, but not necessarily save us if we went into the water. After every ten lines we would set the machine down, walk around until we stopped shaking, and then remove the cowlings and inspect the helicopter minutely before taking off again

Processing

Particularly in areas where the water was very turbulent, we had concerns that the velocity would be higher than in still water, because of the entrained air. We had counted on finding hyperbolic reflections to allow us to determine true velocity values. However, we could not identify such reflections, even in the most critical areas, where the water was most turbulent and presumably most aerated. Fortunately, the water in the critical area between the falls appeared to be relatively less aerated, so that applying water velocity values could provide reasonably accurate depths.

Reflections from water surface and river bottom were digitised at trace intervals from one to four seconds, depending on the bottom complexity revealed in the particular profile. Water surface elevations were established using the air velocity of 30 centimetres per nanosecond (cm/ns). The time differences between water surface and bottom reflections were digitised, and depths determined by using the water velocity of 3.3 cm/ns. Bottom elevations were then determined by reference to the water surface elevations.

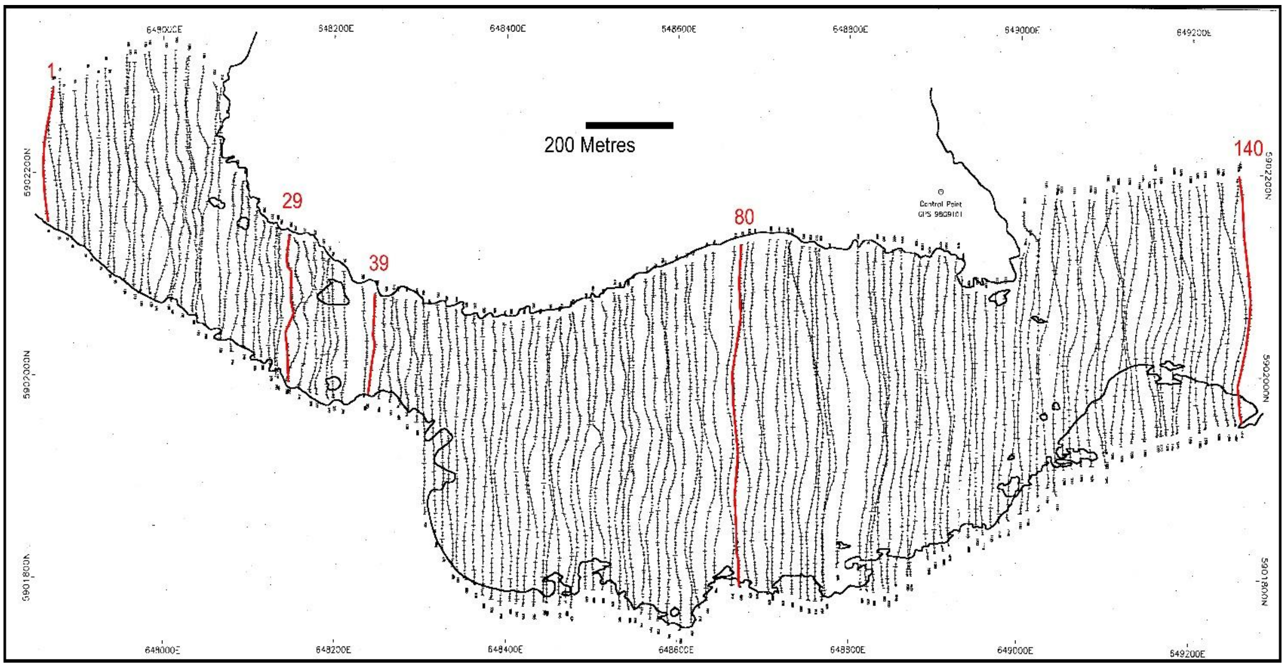

Figure 2: Survey lines. Line 80 is the red line in the centre.

Results

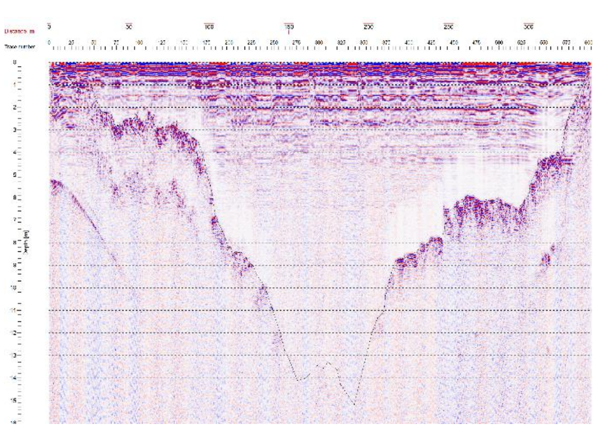

Figure 3: GPR profile on Line 80. Depth at water velocity is 15 m.

Figure 3 shows the GPR profile on Line 80, highlighted in red in the central part of the survey area (Figure 2). The horizontal distance is about 350 metres, and there is significant vertical exaggeration. If the velocity in the water is truly 3.3 cm/ns, then the depth to the bottom in the central part of the profile is about 15 metres. At this depth, the reflections are quite faint, but are picked partly on the basis of line-to-line correlation.

Figure 4 shows the bedrock elevations determined on the assumption that not enough air was entrained in the water to alter the velocity significantly.

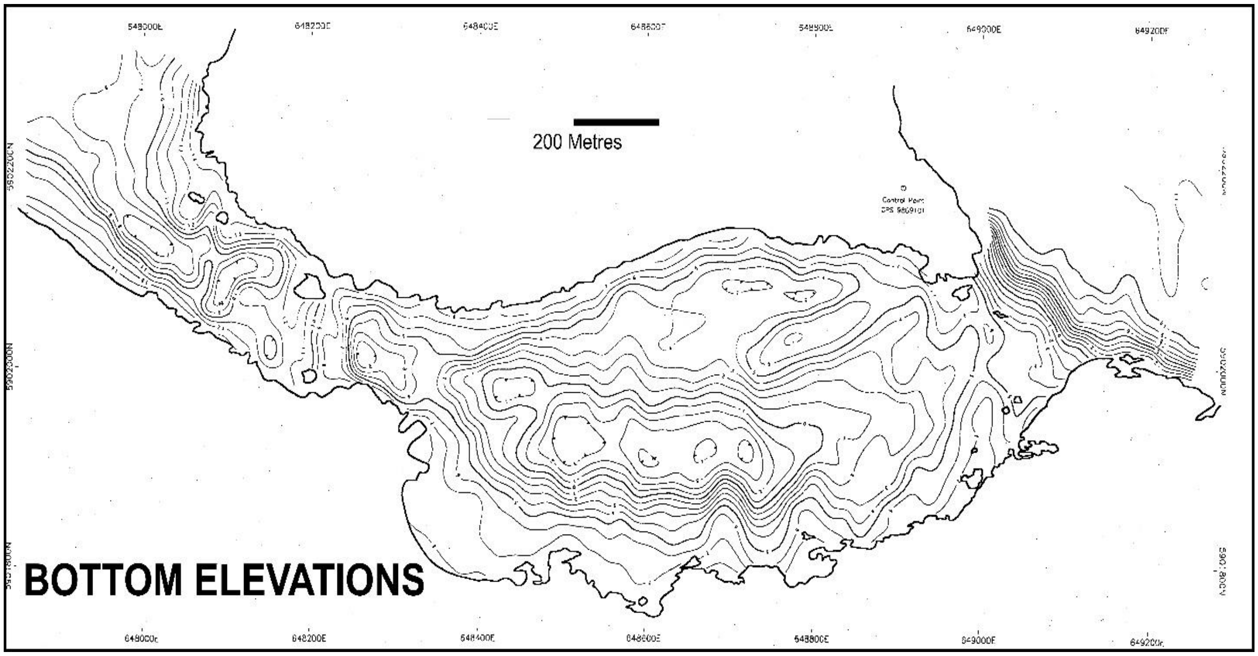

Figure 4: Bedrock elevations determined from the time difference between the GPR reflections from water surface and bottom. Contour interval is 1 metre.

Conclusions

At the time of the survey, we understood that the question of greatest interest was how well the central pool would drain if a coffer dam was placed above the upper falls. The bedrock elevations indicate a depth of over 12 metres which would not drain naturally once the river flow was cut off.

Unfortunately, we never heard how closely our interpreted elevations matched the surface once drained. We have to assume that this is because the elevations were reasonably accurate.

Acknowledgements

The pilot for Héli-Transport, R. Brunet, showed nerves of steel in flying the survey.
Grant Hiscock found for me the data release on the NALCOR website.
Terraplus Inc. provided the RAMAC in 1998, and now lent me the software to re-process the profiles shown in this paper and in the presentation.

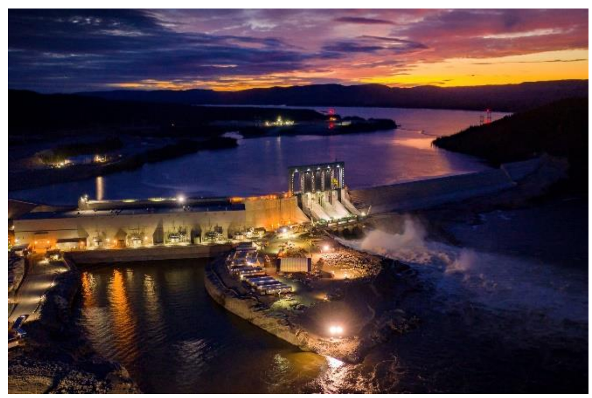

Figure 5: Muskrat Falls viewed from the east in 2021 (NALCOR photo). Compare with Figure 1, taken from roughly the same point..

References

NALCOR GPR Report Release:
https://muskratfalls.nalcorenergy.com/wp-content/uploads/2016/03/Ref-21-Muskrat-Falls-Hydroelectricy-Development-Final-Feasibility-Study-Vol-2-1998-Appendix-A-C.pdf

NALCOR Photo:
https://muskratfalls.nalcorenergy.com/construction-activities/muskrat-falls-hydroelectric-generating-facility/

Establishment of a hardrock seismic test site in central Sweden

Alireza Malehmir (Uppsala University, Sweden), Magdalena Markovic (Uppsala University, Sweden), Myrto Papadopoulou (Uppsala University, Sweden) and Paul Marsden (Nordic Iron Ore, Sweden)*

Summary

Through over 10 years of research and innovative studies, Ludvika Mines (operated by Nordic Iron Ore) in central Sweden has witnessed over 4 campaigns of 2D seismic surveys, a sparse 3D survey, a dedicated surface and downhole fiber-optic sensing survey acquired with a collocated 3C and broadband geophone array as well as numerous UAV, helicopter, fix-wing magnetic and electromagnetic surveys. The site also provides a wealth of borehole data (geochemistry and assay data) and downhole physical properties including magnetic susceptibility, density, P- and S-wave velocities, remnant magnetization, AMS, IP and electrical conductivity. Seismically, the main target, a series of sheet-like iron-oxide mineralization, magnetite and hematite, is reflective, however, it shows a complex nature including multiple reflections, suddenly truncated with enigmatic diffraction signals. These horizons and a number of crosscutting reflections have been the challenge of several recent studies including the use of deep-learning solutions for diffraction mapping and enhancement.
The mineralization and structures controlling the geometry of the deposits are of significant relevance since the mining operation is expected to commence in a couple of years. Historical mine tailings cover part of the area and severely complicate imaging the deposits underneath them because of their slow velocity, varying thickness and attenuative nature. Active and passive seismic recordings have partly resolved this problem, however, more needs to be done to characterize the tailings and the potential resources underneath them including possible repurposing of the tailing materials. In this presentation, we primarily focus on the technical works, showcase possibilities for future works from data integration, interpretation and even new data. Arguably, the Ludvika Mines has led to more research publications and testing new prototypes and solutions than many other similar type sites, hence worthwhile emphasising it here.

Introduction

Demand for minerals has peaked up again due to the rapid transition towards green technologies and clean sources of energy. This has pushed the mineral exploration industry to innovate more to the degree that it would not be questioned similar to the hydrocarbon industry today. The innovations must be cost-effective, environmentally-friendly and sustainable. Taking advantage of the wealth of information available from the historical mineral endowed Bergslagen district of central Sweden, since 2014, we have been developing solutions and methods for deep targeting and better mapping of iron-oxide deposits (Figure 1) that are sometime the host for critical minerals such as apatite and REEs.
In 2015, for the first time, we acquired a landstreamer seismic profile that allowed imaging of the deposits down to 800 m depth (Malehmir et al., 2017a). Followed by downhole logging data (Maries et al., 2017), we complemented the landstreamer survey with two industry standard orthogonal seismic profiles to provide a semi-3D image of the deposits (Markovic et al., 2020; Maries et al., 2021). Petrophysical studies including anisotropy of magnetic susceptibility (AMS), remnant magnetization and constrained potential field modelling workflows were also followed.

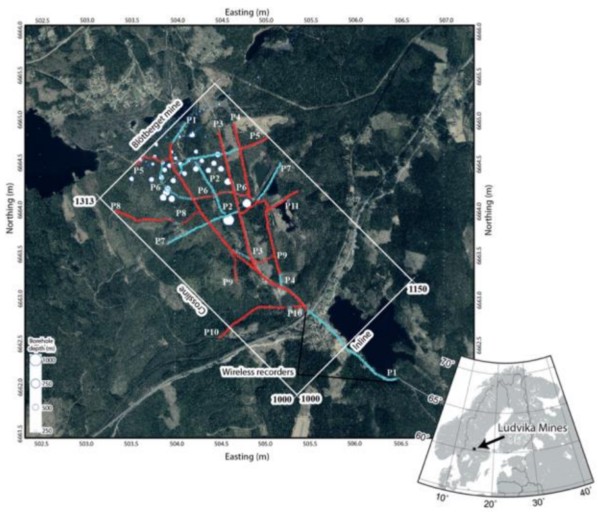

Figure 1. Map showing the exploration site, Blötberget iron-oxide deposits, where extensive innovative solutions have been, and will be, experimented during 2014-2024. P1 is the focus of this paper.

In 2016, we tested rotary-wing drones for magnetic surveying at the site with promising results, justifying why innovations in UAV-based magnetic and electromagnetic surveys are needed and challenges required to be addressed over highly magnetic bodies (Malehmir et al., 2017b). This led to a new UAV-based system and birds developed for both magnetic and extended VLF and was showcased at the site (Bastani et al., 2020). Three sets of fixed-wing and helicopter-based magnetic surveys from 1972, 2016 and 2019 were used to assess the potential of the new sensors and acquisition system developed for this purpose.

In 2019, we also acquired the first 3D seismic dataset to be reported for mineral exploration purpose in Sweden (Malehmir et al., 2020) and how this led to argue for additional potential resources (laterally and down-dip) of up to 30 Mt of iron-oxide deposits. Carefully planned, the sparse 3D survey only used existing tracks and forest roads but was optimized in such a way that it could provide this valuable information on possible extension of the deposits and faults crosscutting the deposits. A modular, for slimholes (less than 48 mm in diameter), seismic system was then developed and tested at the site to allow using the extensive drillholes used in the mining industry for resource assessments and for improved exploration and optimum imaging (Sivard et al., 2020). Inspired by broadband and green-tech developers, we also took part in experimenting a broadband electrically-driven electromagnetic-based seismic vibrator at the site along the same profile (P1) where the landstreamer and conventional surveys were conducted (Pertuz et al., 2022). Thanks to these realizations, it was possible through an academic-industry-SME (small to medium-sized enterprises) partnership to make the site without a doubt the most documented study area for innovative mineral exploration solutions in Sweden. The study area is an excellent hardrock site for technology and software solution testing and often also offers new outcomes and challenges for research development works.

Figure 2. Photos showing several different recorders and seismic sources experimented at the Blötberget site. (a) Seismic landstreamer survey in 2015, (b) drophammer source used in the 2015 and 2016 surveys, (c) the 32t vibrator used in the sparse 3D survey (2019) and (d) e-vib broadband seismic source (in 2019) used along the same profile (P1) as the 2015 and 2016 surveys for comparative works.

To further exemplify this, in 2022, we also acquired new sets of seismic data using collocated 1C-3C nodal arrays, broadband source-receivers and fiber-optic sensing technologies on surface and in boreholes (Figure 3). The new technology testing was made to allow both active- and passive seismic recoding for improved imaging of the mineralization as well as structures controlling its shape and geometry.

Example seismic data

A MEMs-based seismic landstreamer was for the first time experimented for deep exploration at the site using 100 sensors 2-4 m spaced (240 m long in total) and moved 9 times to cover a section of approximately 3-km long. For the seismic source, a 500-kg drophammer easily rentable from local places was used (Figure 2). The experiment meant to check possibility of existing solutions for deep targeting without extensive cost expenditure. We noted clear reflections in the streamer data and were able to image the main deposits down to 800 m depth, which was already known from existing boreholes (Malehmir et al., 2017b). While the experiment was useful, it did not add new geological knowledge although helped to suggest the streamer could be used for this purpose too.

The drophammer seismic source (Figure 2b) came as a surprise since it allowed a reasonably well imaging of the deposits, therefore, in a new survey in 2016, we used the same source but employed plant-type recorders instead using two orthogonal profiles simultaneously recorded to provide psudo-3D information (Maries et al., 2021). The new 2016 and 2015 datasets were merged and processed together (Figure 4a), and this helped to improve depth imaging of the deposits down to 1200 m depth, 400 m deeper than was possible with the streamer and known from boreholes (Markovic et al., 2020).

Given the 3D complexity of most hardrock settings, we were aware that seismic interpretations based on 2D data are highly risky for deep targeting hence a 3D survey, though sparse, using approximately 1200

Figure 3. Field photos showing a recent seismic survey (2022) conducted in Ludvika Mines (Blötberget) employing a broad range of collocated receivers such as 1C and 3C nodal arrays as well as fiber-optic cables laid out as seismic sensor. A broadband seismic source was used operating sweeps in the range of 2-200 Hz

recorders in a fixed geometry taking advantage of 11 existing forest roads/tracks, was conducted in 2019. A 32t seismic vibrator was employed as the seismic source and helped to provide unprecedented 3D image of the deposits (Figure 4c-e) beyond their known depth and lateral extents (Malehmir et al., 2020). Faults and fracture systems were mapped providing information on the tectonic framework in which the deposits are emplaced.

We performed several seismic recordings that were possible at the site including zero-offset and walkaway VSP, however, there was a need to conduct a broadband seismic recording to showcase higher resolution imaging can be possible if low and high frequencies are generated and recorded.

An e-vib seismic survey was conducted in 2019 (Pertuz et al., 2022) using sweeps generated by an electromagnetic-based shaker from 2-200 Hz. The imaging results provided so far, the best definition of one of the fault systems crosscutting the mineralization (Figure 4b), showing this survey was well worth it and broadband data acquisition and processing workflow should be more attempted for mineral exploration purposes.

All these seismic surveys have led to an improved understanding of 3D geometry of the deposits and faults systems in the study area (Figure 5). We employed the 3D seismic volume and estimated the 3D extent of the deposits through amplitude thresholding and matching with drill holes and assay data. The model was then used for 3D gravity and magnetic modeling employing physical properties measured in down holes and suggesting it is a plausible solution verified by potential field data.

In order to test the emerging fiber-optic sensing technologies for mineral exploration, a series of new seismic surveys was planned and conducted at the site. Fiber-optic cables of various types were set up on the surface and in a borehole and collocated broadband

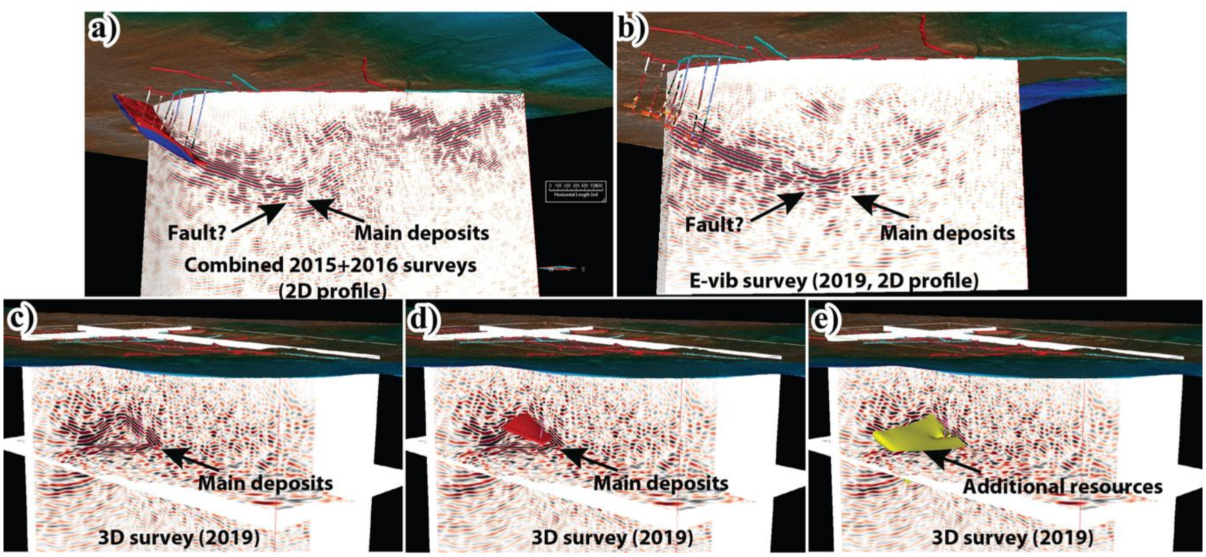

Figure 4. Example seismic sections generated from various surveys at the Blötberget site. (a) Combined 2015+2016, (b) 2019 e-vib, and (c-e) the 2019 3D sparse survey. The surveys all suggest a deeper continuation of the deposits with the 3D one even suggesting additional resources (yellow surface laterally beyond the known ones (red and blue surfaces).

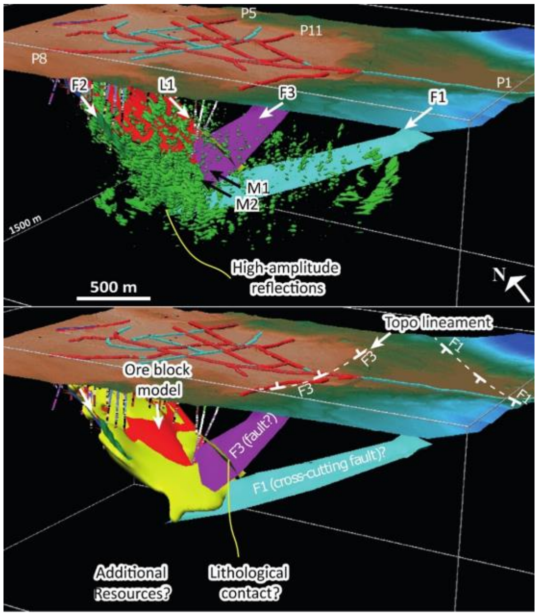

Figure 5. 3D model of the mineralization (red from boreholes and yellow from the 3D seismic survey) and fault system crosscutting it. Amplitude thresholding was used to propose downdip and lateral extension of the deposits.

and geophone-based nodal arrays were used to scrutinize the fiber-optic data. Preliminary results are promising and show improved quality imaging of the deposits and also help to design similar surveys at the site in the near future.

Conclusions

Given the wealth of seismic data, their novelty and geological knowledge produced at the Ludvika Mines site, we propose the site to be used for technology testing and in particular to develop hardrock seismic solutions. Mining operation is planned to commence at the site in a couple of years and this would help to verify interpretations and if any adjustments and revaluation of the survey setups would be required.

Acknowledgments

Several initiatives led to the development works presented and introducing the site as a hardrock test site including ERA-Min1 StartGeoDelineation, EU-funded Smart Exploration and ERA-Min3 Future projects. Nordic Iron Ore has played a key role in embracing, partnering, and supporting these works. All these datasets have been shared with the geoscientific community in a purposeful manner to further scrutinize the potential of the developed hardware solutions and methods to maximize their values.

References

Bastani, M., Johansson, H., Paulusson, A., Paulusson, K., and Dynesius, L., 2020. Unmanned Aerial Vehicles (UAV) and ground-based electromagnetic (EM) systems. First Break, 38, 87–89.

Malehmir, A., Markovic, M., Marsden, P., Gil, A., Buske, S., Sito, L., Bäckström, E., Sadeghi, M., and Luth, S., 2021. Sparse 3D reflection seismic survey for deep-targeting iron oxide deposits and their host rocks, Ludvika Mines, Sweden. Solid Earth, 12, 483–502.

Malehmir, A., Dynesius, L., Paulusson, K., Paulusson, A., Johansson, H., Bastani, M., Wedmark, M., and Marsden, P., 2017b. The potential of rotary-wing UAV-based magnetic surveys for mineral exploration: A case study from central Sweden. The Leading Edge, 36, 552–557.

Malehmir, A., Maries, G., Bäckström, E., Schön, M., and Marsden, P., 2017a. Developing cost-effective seismic mineral exploration methods using a landstreamer and a drophammer. Nature Scientific Reports, 7, 10325.

Maries, G., Malehmir, A., and Marsden, P., 2020. Cross-profile seismic data acquisition, imaging and modeling of iron-oxide deposits: a case study from Blötberget, south central Sweden. Geophysics, 85, B219–B233.

Maries, G., Malehmir, A., Bäckström, E., Schön, M., and Marsden, P., 2017. Downhole physical property logging for iron-oxide exploration, rock quality, and mining: An example from central Sweden. Ore Geology Reviews, 90, 1–13.

Markovic, M., Maries, G., Malehmir, A., von Ketelholdt, J., Bäckström, E., Schön, M., and Marsden, P., 2020. Deep reflection seismic imaging of iron-oxide deposits in the Ludvika mining area of central Sweden. Geophysical Prospecting, 68, 7–23.

Sivard, A., Jansson, N., Juhlin, C., and Malehmir, A., 2020. Slimhole system. First Break, 38, 78–79.

Pertuz, T., Malehmir, A., Bos, J., Brodic, B., Ding, Y., de Kunder, R., and Marsden, P., 2022. Broadband seismic source data acquisition and processing to delineate iron oxide deposits in the Blötberget mine-central Sweden. Geophysical Prospecting, 70, 79–94.